Photovoltaic Modeling and Grain Boundary Recombination in Poly-Silicon

by

Zhizhang Chen

Dissertation submitted to the Faculty of the

Virginia Polytechnic Institute and State University

in partial fulfillment of the requirements for the degree of

Doctor of Philosophy

in

Materials Engineering Science

APPROVED:

Larry C. Burton, Chairman

F.W.Stephenson

A.Elshabini Riad

D.Y.Chen

S.B.Desu

Photovoltaic Modeling and Grain Boundary Recombination in Poly-Silicon

By

Zhizhang Chen

L.C.Burton, Chairman

Materials Engineering Science

ABSTRACT

In the first part of this dissertation, an analytical approach to n^+/p solar cells is developed. Based on this model, the short circuit current, open circuit voltage and energy conversion efficiency of the cells as a function of doping concentration, junction depth, minority carrier surface recombination velocity and diffusion length are discussed. This model simplifies the analysis of the solar cell, and the calculated results agree closely with both experimental results and numerical analysis.

The second part of the dissertation deals with grain boundary (GB) recombination, passivation, and characterization. A simple GB model is developed, and an expression for the GB barrier height under illumination is derived by introducing a quasi Fermi-function. By using this model, the dependencies of the minority carrier transport parameters on the illumination level, grain size, depth from the surface and trap state density are derived. The model is compared to the experimental results for GB capacitance and electron lifetime measurements.

Hydrogen passivation of poly-Si solar cells was accomplished experimentally by hydrogen implantation. A systematic study of implantation parameters was conducted

and an optimum condition was found for the samples under examination. Under this condition, 18 % improvement in cell efficiency was achieved for the cells, with initial efficiencies of about 7%. A transmission electron microscope (TEM) study of the hydrogen-dislocation interaction and hydrogen ion bombardment effects on the surface were also conducted. The GB recombination velocity and the hydrogen passivation effect were characterized by the electron beam induced current (EBIC) technique. A nonuniform passivation depth was observed. The nature of the passivation mechanism was addressed. It was found that hydrogen saturation of dangling bonds in Si grain boundaries is not the only mechanism for hydrogen passivation.

Acknowledgements

The author wishes to express the deepest appreciation to Dr. L.C.Burton for his guidance, encouragement and advice throughout this research. Special thanks are due to Dr. F.W.Stephenson for his suggestions and contributions to this project. The author also thanks Dr. A.Elshabini Riad, Dr. D.Y.Chen and Dr. S.B.Desu for their help and for serving on his committee.

The author acknowledges financial support from Electron-Science Lab. Inc., the Virginia Center for Innovative Technology and The Bradley Department of Electrical Engineering at Virginia Tech.

Thanks are extended to Dr. Y.S.Tsuo, Dr. R.J.Matson and Dr. B.L.Spori of Solar Energy Research Institute (SERI) for their contributions and help with access to the facilities at SERI. Appreciation is extended to Gang Chen, C.K.Kwok, (Mat.Eng.Dept.) and T.D.Lin (Chemistry Dept.) for the help in TEM and FTIR measurements; to R.R.Walters (Hybrid Lab.) for help in cutting samples. Appreciation is also extended to the author's colleagues for stimulating discussions and help in many different ways: Eric Ellis, Dr. S.Sidhartha, Dr. A.Vaseashta, Dr. I.K.Yoo, S.Massie, P.Johnson and C. Turman. I would like to express my special thanks to Dr. J.F.Phelan and Garry Kunselman for their grammatical corrections.

The sincerest gratitude is due to my wife, Qin Liu, for her constant support and encouragement throughout my graduate school career.

Table of Contents

Chapter 1

Introduction

1.1 Background

Developments in solar cell technology have experienced an accelerated pace in recent years. In particular, silicon solar cells in terrestrial applications have become the focus of intensive research because of their reasonably high efficiency and reliability. As a result of this research, the efficiency of crystalline silicon cells in the laboratory has been improved from 15% in 1978 to above 22% in 1989 [1]. Most of the improvement has originated from reducing the cell surface recombination velocity, and improved material qualities. To understand the physical principles of the solar cell and the recent developments, a model which can account for the operation of both the conventional cell (with high surface recombination velocity) and high efficiency cell (with low surface recombination velocity) is desired. Numerical approaches traditionally used in solar cell modeling are rather complicated [2-4]. To simplify the analysis, analytical approaches in solar cell modeling have received increasing attention [5-7]. In Chapter 2 of this dissertation, an analytical modeling approach is proposed in which new expressions for the photo-generation rate and photo-current are developed. Based on this analytical approach, calculations have been made for the short circuit current J_{sc}, open circuit voltage V_{oc} and efficiency EFF as functions of the base region doping concentration N_a, junction

Comparisons are also discussed between the calculated results and experimental results.

From a theoretical point of view, highly purified Si material with longer minority lifetime and diffusion length is desired in order to achieve high efficiency. However, a major concern in terrestrial applications is the cell cost. The dominant contribution to the cost of the total package is the cost of the cell substrate. Accordingly, several approaches have been developed to reduce the substrate cost. Slow solidification in an appropriate mold results in poly-Si ingots with large columnar grains, and solidifying molten silicon directly in large area sheet (called edge-defined film-fed growth) results in silicon ribbon material. Both poly-Si ingots and ribbons are manufactured commercially. Low cost approaches inevitably produce materials of poorer crystallographic quality than does the normal silicon Czochralski process used for integrated circuit applications. Additionally, there are more impurities incorporated and more dislocation defects in the intragrain regions. The most important difference between crystalline and polycrystalline materials arises from the presence of grain boundaries which can act as very efficient recombination sites for the minority carriers. Thus, the transport of the minority carriers is controlled by the grain boundary recombination [8]. As a result, efficiencies of cells fabricated on poly-Si substrates are generally lower than that of crystalline silicon substrate cells. A study of grain boundary effects on the minority carrier transport parameters is essential to understand the electrical properties of poly-Si material and

to find those key factors that control the quality of the materials. A simplified grain boundary model is proposed in Chapter 3. Based on this model, new expressions for the grain boundary barrier height in the dark and under optical illumination are developed. The dependencies of the transport parameters such as lifetime τ, mobility μ and diffusion length L on the grain boundary barrier height V_g, grain size d, illumination level G, depth x from the surface, and grain boundary trap state density N_{ts} are discussed quantitatively. Experimental results on the trap state density N_{ts}, electron capture cross section σ_n, and lifetime τ are interpreted in terms of the grain boundary model.

Quantitative analysis [9] has shown that N_{ts} is one of the major material parameters which controls the grain boundary recombination and the minority carrier transportation in poly-Si materials. To improve the minority carrier transport parameters and the efficiency of a finished poly-Si solar cell, several passivation methods have been proposed to decrease N_{ts}, such as the incorporation of aluminum and hydrogen [10,11]. Hydrogen passivation is a generally accepted process to improve the quality of low cost silicon substrates. Conventionally, hydrogen was incorporated from the frontside (junction side) of the cells [10,11]. However, front side hydrogenation increases the surface recombination velocity and places some restrictions on cell fabrication processes [13,14]. Accordingly, backside hydrogen implantation was recently proposed [15,16], but a systematic investigation on the implantation parameters has not been reported. Additionally, a basic question has

not been answered concerning how deep hydrogen can diffuse from the back surface. Efforts are reported in Chapter 4 to find optimum implantation parameters such as the hydrogen ion beam energy E, beam current I_b, sample holder temperature T and implantation duration t. The improvements for cells with different initial conditions are discussed. Transmission electron microscopy (TEM) results of hydrogen-dislocation interaction and surface damage caused by ion beam bombardment are also presented.

The scanning electron microscope (SEM) in the electron beam induced current (EBIC) mode provides a measurement with far greater resolution and more sensitivity to electronic defects than other measurements [17]. Therefore, as discussed in Chapter 5, the EBIC technique was applied to quantitatively characterize the grain boundary recombination velocity, diffusion length, and hydrogen passivation effects on the grain boundaries. The passivation depth for backside hydrogenation was also monitored by the EBIC technique. A combination technique of EBIC and an Electron Channeling Pattern (ECP) is discussed. It makes the correlation possible between the grain boundary recombination and the grain's crystal orientations. The cell surface recombination velocity was also determined by measuring the beam energy dependence of EBIC current.

1.2 Basic parameters in solar cells

Solar cell performance can be characterized by three major parameters: the open circuit voltage V_{oc} (which is the voltage output when the output current is zero);

the short circuit current density J_{sc} (which is the output current density when the output voltage is zero); and the fill factor FF (which is the ratio of maximum power output to the product of V_{oc} and J_{sc}). These three parameters determine the energy conversion efficiency (EFF) of a solar cell as follows:

$$EFF = \frac{V_{oc} J_{sc} FF}{P_i} \qquad (1.1)$$

where P_i is the incident light power density.

V_{oc} is directly related to the energy bandgap of the semiconductor through the energy barrier height at the junction. The upper limit of V_{oc} is the bandgap. V_{oc} is often expressed as a function of J_{sc} and J_o, the leakage current of the junction without illumination [18], and can be written as

$$V_{oc} = A\left(\frac{kT}{q}\right) \ln\left(\frac{J_{sc}}{J_o} + 1\right) \qquad (1.2)$$

where A is the junction quality factor.

For a good junction, A is equal to unity and V_{oc} attains its highest value, while for larger values of A, J_o increases in such a way that V_{oc} is reduced. A closed analytical expression for J_o has been derived [18]. It is determined mainly by the bandgap, doping concentration, and the minority carrier diffusion length. In general, longer diffusion length, higher bandgap, and doping density result in a lower J_o, and thus higher V_{oc}. But if the doping density is so high that the diffusion length and bandgap become less, J_o will increase and V_{oc} will decrease.

J_{sc} is determined by the spectrum of the light source and the spectral response of the cell. The spectral response in turn depends on the optical absorption coefficient, the junction depth, the width of depletion region, the minority carrier lifetime, the diffusion length on both sides of the junction, and the surface recombination velocity. The bandgap dependence of J_{sc} is manifest through the absorption coefficient. Generally speaking, larger bandgap materials absorb less sunlight and have a smaller J_{sc} than smaller bandgap materials. A longer diffusion length and lower surface recombination velocity are always desired to get a higher J_{sc}. A higher doping concentration, however, will decrease the diffusion length and result in lower J_{sc}.

FF measures the squareness of the J-V curve. It is determined by V_{oc}, A, shunt resistance R_{sh}, and series resistance R_{se}. The higher V_{oc} and R_{sh}, and lower A and R_{se}, the larger FF will be. For the ideal case in which $A = 1$, $R_{sh} = \infty$ and $R_{se} = 0$, the FF can be determined by V_{oc} [18].

For both crystalline and polycrystalline solar cells, lower surface recombination and higher diffusion length will improve the EFF of the cells. For polycrystalline cells, the diffusion length strongly depends on grain boundary trap density states N_{ts} [9]. Therefore, the necessity for grain boundary passivation is obvious. That is one of the major topics of this thesis.

References

[1]. U.S. Department of Energy, Photovoltaic Energy Program Summary, p3, (1989).

[2] J.G. Fossum, Solid-State Electron. Vol.19, p269, (1976).

[3] P.M.Dunbar and J.R.Hauser, Solid-State Electron. Vol.19, p96, (1976).

[4] M.Wolf, IEEE Trans. Electron Dev. ED-27, 751, (1980).

[5] H.C.Hsieh, C.Hu and C.I.Drowley, IEEE Trans. Electron Dev.ED-27, p883, (1980)

[6] J.Furlan and S.Amon, Solid-State Electron. Vol.28, P1241, (1985).

[7] S.Noor Mohammad,J.Appl.Phys.61(2),p767,15 January (1987).

[8] Z.Chen and L.C.Burton, 21st IEEE Photovoltaic Spec.Conf., p731, (1990).

[9] Z.Chen and L.C.Burton, Phys.Stat.Sol.(a), 122, p361, (1990)

[10] S.Martinuzzi, H.Poitevin, M.Zehaf and C.Zurletto, Reve.Phys.Appl.22, p645, (1987)

[11] Y.S.Tsuo and J.B. Milstein, Appl. Phys. Lett. 45, p971, (1984).

[12] J.I.Hanoka, Appl. Phys. Lett. 42, p618, (1983).

[13] R.O.Bell and C.E.Dube, 18th IEEE Photovoltaic Spec.Conf., p795, (1987).

[14] B.L.Sopori, J. Appl. Phys. 64, p5264, (1988).

[15] H.Yagi, H., et. al., 19th IEEE Photovoltaic Spec.Conf., p1600 (1988).

[16] S.Martinuzz, et. al., 18th IEEE Photovoltaic Spec.Conf., P1069, (1987)

[17] D.B.Holt and D.C.Joy, SEM Microcharacterization of Semiconductors, p241, (1989)

[18] H.J.Hovel,Semicondutors and Semimetals.Vol.11,Solar Cell, (1975).

CHAPTER 2

Solar Cell Modeling

2.1 Introduction

A major task in solar cell modeling involves solving a transport equation for minority carriers. The equation can be expressed as:

$$D_p \frac{d^2 p'}{dx^2} + g(x) - \frac{p'}{\tau_p} = 0 \qquad (2.1)$$

where p′ is the excess minority carrier density, D_p and τ_p are the diffusion coefficient and lifetime, respectively, and g(x) is the photo-generation rate. It is evident that a solution to the equation depends on the form of g(x). g(x), in general, can be expressed as:

$$g(x) = \int N_{ph}(E)\,\alpha(E)\,e^{-[\alpha(E)\,x]}\,dE \qquad (2.2)$$

where $N_{ph}(E)$ is the incident photon density entering a semiconductor surface, $\alpha(E)$ is the absorption coefficient, E is the photon energy and x is the depth from the surface. It is customary to approximate g(x) as a series expansion, with each term corresponding to a spectral segment of incident light. For accurate analysis, the transport equations for each component are solved numerically, which can be quite cumbersome [1-3]. For simpler analysis, the following approximation has been proposed by Hsieh et.al [4]:

$$g(x) = \sum_i \frac{g_i}{a_i + x} \qquad (2.3)$$

where g_i and a_i are numerical parameters obtained by trial and error. It has been shown that Eq.(2.3) had excellent agreement with the numerical integration of g(x). However, the disadvantages of Eq.(2.3) are, as the authors stated, that each term in g(x) does not have direct physical meaning and that a less familiar exponential integral function is involved in its solution:

$$J_{sc} = \sum_i \frac{qg_i}{2}\left\{H\left(\frac{W_p - a_i}{L_n}\right) - \frac{H\left(\frac{a_i}{L_n}\right) + \left[\frac{S_o L_n}{D_n}\left(1 - \cosh\left(\frac{W_p}{L_n}\right) - \sinh\left(\frac{W_p}{L_n}\right)\right)\right] K\left(\frac{W_p + a_i}{L_n}\right)}{\cosh\left(\frac{W_p}{L_n}\right) + \frac{L_n S_o}{D_n}\sinh\left(\frac{W_p}{L_n}\right)}\right\} \qquad (2.4)$$

where

$$K(y) = Ei(y)\, e^{-y} - Ei(-y)\, e^{y}$$
$$H(y) = \frac{dK(y)}{dy} \qquad (2.5)$$

and in which Ei(y) is an exponential integral function available only in tabulated form in mathematics handbooks. Thus, J_{sc} still could not be calculated analytically.

To overcome this problem, another approximation for g(x) was proposed by Furlar et al [5]:

$$g(x) = \sum_i^n a_i e^{-b_i x} \qquad (2.6)$$

where a_i and b_i are determined by curve-fitting. Relation (2.6) was used to calculate photocurrent from the base region for two diffusion lengths, 10 and 100 microns [5], but the solution was not presented in their paper. An approximation similar to Eq.(2.6) has been used to solve the transport equation for an n^+-p silicon cell, and an analytical form of short circuit current was presented [6]. In the previous approaches, however, the depletion region width of the p-n junction was ignored. The approaches not only oversimplified the problem but also the final expression for short circuit current in ref.6 was still rather complicated.

The main object of this chapter is to use analytical methods to simplify the analysis of conventional solar cells and to study the effects of substrate doping concentration N_a, junction depth X_j, surface recombination velocity S_p and minority carrier diffusion length L on short circuit current J_{sc}, open circuit voltage V_{oc} and efficiency EFF. In this chapter, a new simpler analytical expression for the photocurrent of n^+-p silicon cell is developed, which includes three contributions: from the top layer, base region and depletion region. It will be seen that the depletion region contribution cannt be neglected, especially when the doping concentration of the substrate is less than 10^{17} cm^{-3}.

A new method to calculate g(x) is presented in section 2.2. A simpler expression for photocurrent is developed in section 2.3. The calculated results of J_{sc}, V_{oc} and EFF as a function of N_a and X_j, and the comparisons with numerical analysis and experimental results are presented in section 2.4. In section 2.5, high efficiency

silicon solar cells are discussed, where the low surface recombination velocity and high diffusion length strongly influences spectral response SR, saturation current J_o, J_{sc}, V_{oc}, and EFF.

2.2 Gauss-Quadrature (G-Q) Approximation for g(x)

Mathematically, g(x) has been expressed in a summation form by a G-Q method [7]:

$$g(x) = \frac{b-a}{2} \sum_{i}^{n} W_i N_{ph}(k_i)\, \alpha(k_i)\, e^{-[\alpha(k_i)x]} \qquad (2.7)$$

where a, b are the integral limits of Eq.(2.2) (for silicon, a of 1.1 eV and b of 4 eV were chosen). k_i is the key point of G-Q which can be expressed by

$$k_i = \frac{Z_i(b-a)+b+a}{2} \qquad (2.8)$$

Z_i and W_i being the roots and weight factors respectively, which can be found in a standard mathematics handbook.

The major advantage of the G-Q method is that the parameters in Eq.(2.6) can be calculated analytically. If a comparison is made between Eqs.(2.6) and (2.7), a_i and b_i in Eq.2(2.6) can be expressed by:

$$a_i = \frac{b-a}{2} W_i N_{ph}(k_i)\, \alpha(k_i)$$
$$b_i = \alpha(k_i) \qquad (2.9)$$

It can be seen that b_i is the absorption coefficient at the key point, and a_i is proportional to the product of photon density and absorption coefficient at the key point. The proportional factor is related to the upper and lower limits, and weight factor in the G-Q method.

In order to calculate g(x), the silicon absorption coefficient and the photon spectral for a given air mass number are needed. Silicon absorption coefficient as a function of photon energy can be found from ref.[8]. The photon density distribution for AM0 (air mass zero) condition was from Wysocki [9]. The photon density for AM1 (air mass one) condition was obtained by converting energy density of AM1 [10]. We have computed g(x) for silicon under AM0 and AM1 illumination conditions by using Eqs (2.7-2.9). a_i and b_i are listed in Table 2.1.

Figs.2.1 and 2.2 compare the g(x) calculated by six-point G-Q approximation and obtained numerically [1,4], for AM0 and AM1, respectively. It can be seen that the results of the G-Q approximation are close to the results of numerical integration within a depth of 500 microns for both the AM1 and AM0 cases. This depth is deep enough for silicon solar cell applications.

Table 2.1 The coefficients $a_i(cm^{-3}s^{-1})$ and $b_i(cm^{-1})$ in g(x) for silicon at AM1 and AM0 conditions calculated by the G-Q method

a_i and b_i	AM1	AM0
a_1	$1.334x10^{21}$	$2.207x10^{21}$
a_2	$5.686x10^{20}$	$5.948x10^{20}$
a_3	$3.386x10^{21}$	$4.534x10^{21}$
a_4	$9.348x10^{19}$	$16.06x10^{19}$
a_5	$1.411x10^{21}$	$16.42x10^{21}$
a_6	$2.002x10^{18}$	$1.253x10^{21}$
b_1	$4.7x10^{4}$	$4.7x10^{4}$
b_2	$6.2x10^{3}$	$6.2x10^{3}$
b_3	$1.0x10^{6}$	$1.0x10^{6}$
b_4	$1.2x10^{3}$	$1.2x10^{3}$
b_5	$1.5x10^{6}$	$1.5x10^{6}$
b_6	5.0x10	5.0x10

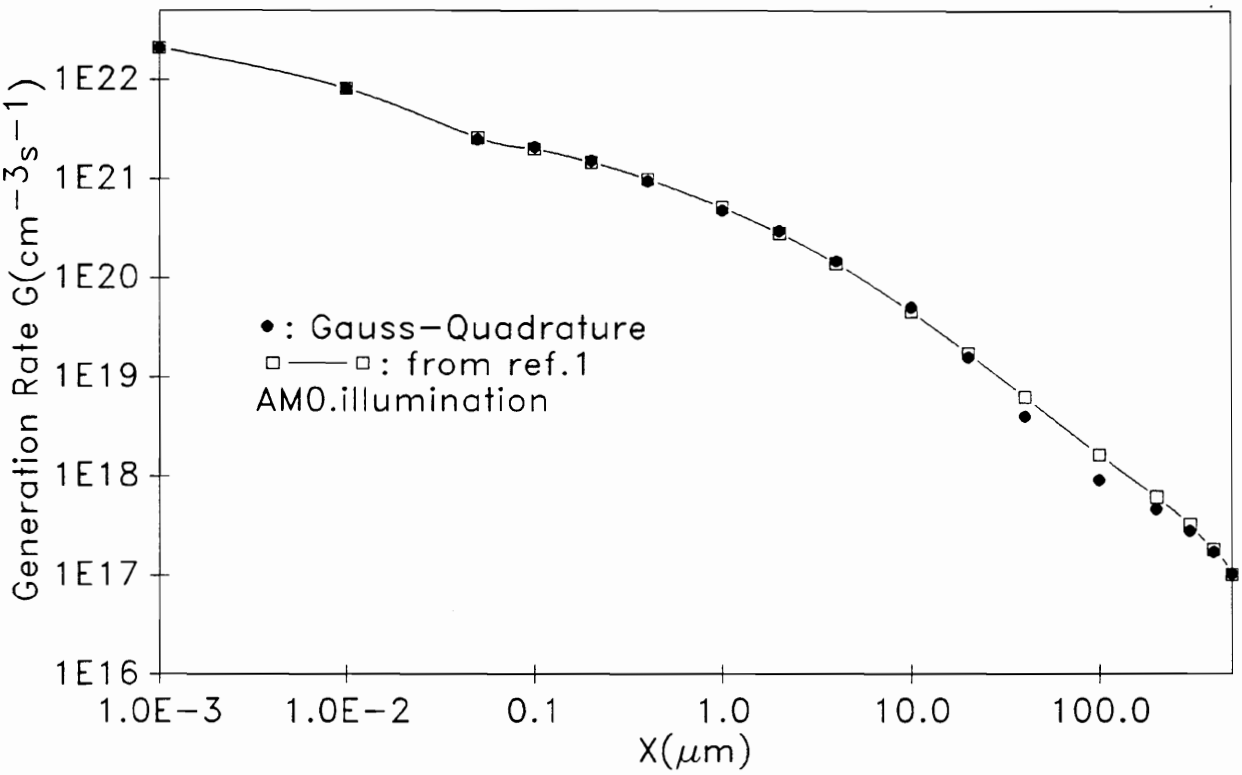

Fig.2.1 The AM0 generation rate calculated by G−Q method and obtained by numerical integration from ref.1

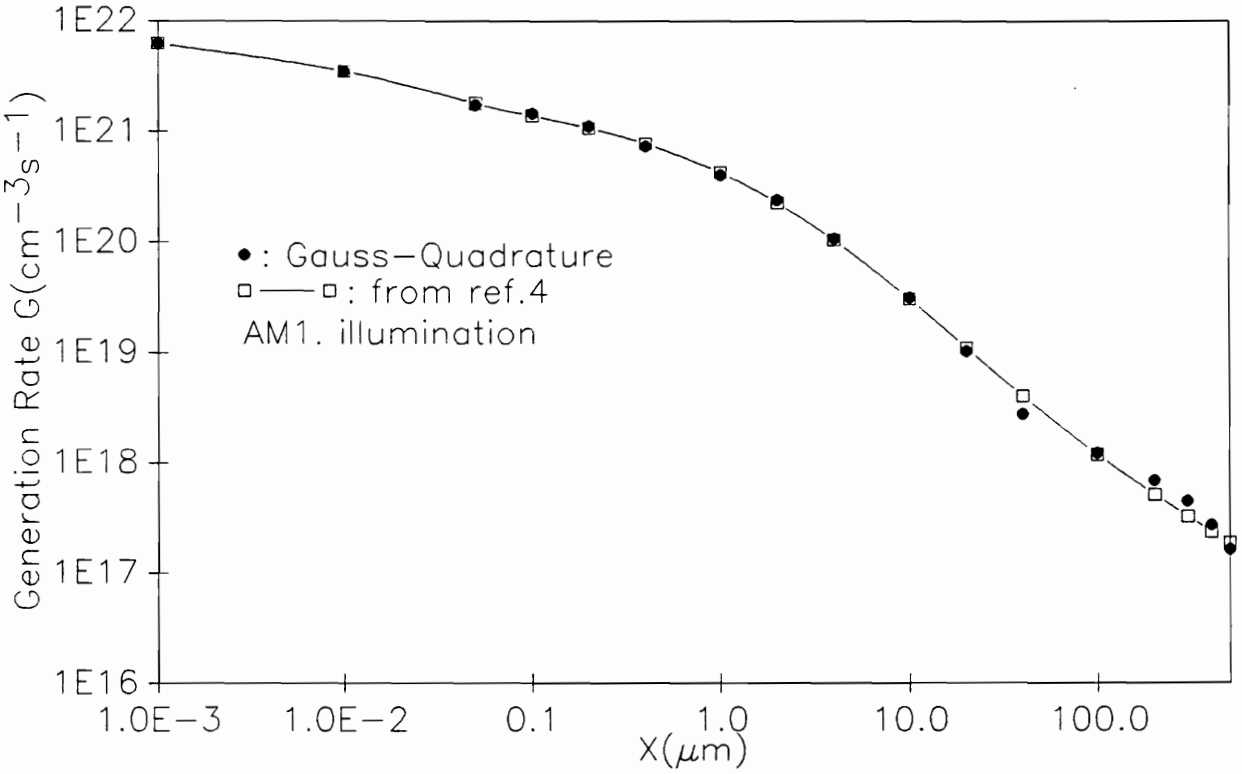

Fig.2.2 The generation rate calculated by G−Q method and the numerical result from ref.4

2.3 Theoretical Model

Since there are so many factors that affect solar cell performance, it is impossible to include all of them at the same time. For this reason, uniformly doped top and base regions were assumed in the modeling. The short circuit current, open circuit voltage, and efficiency as functions of doping concentration (or material resistivity), junction depth, surface recombination velocity and diffusion length were investigated under this assumption.

A schematic structure of a typical n^+-p solar cell is shown in Fig.2.3, where H is the cell thickness, w is the depletion region width and x_j is the junction depth. For the top n^+ layer the minority carrier transport equation can be written as:

$$D_p \frac{d^2 p'}{dx^2} + g(x) - \frac{p'}{\tau_p} = 0 \qquad (2.10)$$

where p'is the excess minority carrier density, D_p and τ_p are the diffusion coefficient and lifetime, respectively. G-Q approximation for g(x) was used and the parameters in g(x) were listed in table 2.1.

Substituting Eq.(2.6) into Eq.(2.10) one obtains:

$$\frac{d^2 p'}{dx^2} + \sum_{i=1}^{6} \frac{a_i}{D_p} e^{-b_{ix}} - \frac{p'}{L_p^2} = 0 \qquad (2.11)$$

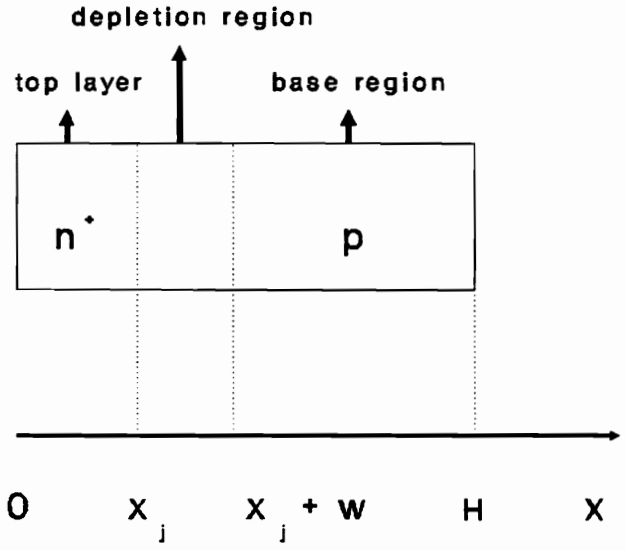

Fig.2.3 Schematic of n/p junction solar cell and the coordinates used in calculations

where $L_p = (D_p \tau_p)^{1/2}$ is the diffusion length.

The general solution to Eq.(2.11) can be expressed as follows,

$$p'(x) = A \cosh\frac{x}{L_p} + B \sinh\frac{x}{L_p} - \sum_{i=1}^{6} \frac{a_i \tau_p}{L_p^2 b_i^2 - 1} e^{-b_i x} \quad (2.12)$$

where A and B were determined by the indicated boundary conditions:

$$D_p \frac{dp'}{dx} = s_p p'(0) \qquad at \quad x=0 \qquad (2.13)$$

$$p'(x) = 0 \qquad at \quad x=x_j \qquad (2.14)$$

in which s_p is the surface recombination velocity.

By using

$$J_p(x_j) = qD_p \frac{dp'(x)}{dx} \qquad at \quad x=x_j \qquad (2.15)$$

we obtained an expression for the top layer contribution to the photocurrent:

$$J_p(x_j) = q \sum_{i=1}^{6} \frac{a_i L_p}{b_i^2 L_p^2 - 1} \left\{ \frac{2(S+b_i L_p) - e^{-b_i x_j}\left[e^{\frac{x_j}{L_p}}(S+1)(1+b_i L_p) + e^{-\frac{x_j}{L_p}}(S-1)(1-b_i L_p)\right]}{e^{\frac{x_j}{L_p}}(1+S) + e^{-\frac{x_j}{L_p}}(1-S)} \right\} \quad (2.16)$$

where $S = s_p L_p / D_p$.

In the above derivation, we have assumed a uniform doping concentration in the top layer. Research has shown that varying the diffused layer impurity profile does not significantly affect device performance, and that uniform doping is a good

approximation [1,11,12].

For the base region, the transport equation and boundary conditions can be written as:

$$\frac{d^2n'}{dx^2} + \sum_{i=1}^{6} \frac{a_i}{D_n} e^{-b_i x} - \frac{n'}{L_n^2} = 0 \qquad (2.17)$$

$$-D_n \frac{dn'}{dx} = s_n n' \qquad at \quad x=H \qquad (2.18)$$

$$n' = 0 \qquad at \quad x=x_j+W \qquad (2.19)$$

where n′ is the excess electrons in the base, and s_n is the surface recombination velocity for the base.

In a like manner, base region contribution to J_{sc} is shown to be:

$$J_n(x_j+W) = q\sum_{i=1}^{6} \frac{a_i L_n}{b_i^2 L_n^2 - 1} e^{-b_i(x_j+W)} \left\{ \frac{e^{\frac{H'}{L_n}}(S'+1)(b_i L_n - 1) - e^{-\frac{H'}{L_n}}(S'-1)(b_i L_n + 1) - 2e^{-b_i H'}(b_i L_n - S')}{e^{\frac{H'}{L_n}}(1+S') + e^{-\frac{H'}{L_n}}(1-S')} \right\} \qquad (2.20)$$

where H'= H - (x_j+w), S'= s_n L_n/D_n and W can be expressed as:

$$W = \left[\frac{2\epsilon V_{bi}}{q} \left(\frac{N_d}{N_a(N_a+N_d)} \right) \right]^{1/2} \qquad (2.21)$$

ϵ being the dielectric constant for silicon, V_{bi} is the built in potential, and N_d and N_a are the doping concentration for the n^+ and p layer, respectively.

Some photocurrent collection takes place within the depletion region as well. The electric field in this region can be considered high enough that photogenerated carriers are accelerated out of the depletion region before they can recombine [13,14]. Therefore the contribution from this region can be expressed as:

$$J_d = q \int_{X_j}^{X_j+W} g(x)\, dx = q \sum_{i=1}^{6} \frac{a_i}{b_i} e^{-b_i x}(1-e^{-b_i W}) \qquad (2.22)$$

By considering the following:

$$J_{sc} = J_p(X_j) + J_n(X_j) \qquad (2.23)$$

$$J_n(X_j) = J_d + J_n(X_j+W) \qquad (2.24)$$

and combining Eqs.(2.16),(2.20) and (2.22), we have for the total short circuit photocurrent:

$$J_{sc} = J_p(X_j) + J_n(X_j+W) + J_d \qquad (2.25)$$

It should be noted that in the above derivations the electric field is assumed to be zero. While this would be true in the homogeneously doped, quasi-neutral base region, it is clearly invalid in a heterogeneously doped base region. One could extend the analysis to include a constant field or a piecewise-constant field model, but it would become rather complicated. This is a limitation of the analytical approaches to solving the transport equation.

In order to predict solar cell efficiency and to make the relationships analytically manageable, approximations are often made so that the series and shunt resistance effects are negligible and the dark current can be written as [14]:

$$J_{dark} = J_o[e^{(\frac{qV}{A_o kT})} - 1] \qquad (2.26)$$

where J_o is the dark saturation current, A_o is the junction perfection factor (which would be close to unity for a good crystal silicon solar cell), V is the voltage, k is the Boltzmann constant and T is the temperature.

Under these conditions, and using the equivalent circuit of a solar cell, the output current density can be expressed as

$$J_{out} = J_{ph} - J_o[e^{(\frac{qV_{out}}{A_o kT})} - 1] \qquad (2.27)$$

The short circuit current is simply given by

$$J_{sc} = J_{ph} \tag{2.28}$$

and the open circuit voltage is obtained by setting the current to zero, then

$$V_{oc} = A_o \frac{KT}{q} \ln\left(\frac{J_{sc}}{J_o} + 1\right) \tag{2.29}$$

where J_o is expressed as

$$J_o = J_{on} + J_{op} \tag{2.30}$$

and J_{on}, J_{op} can be calculated from the following Eqs [14]:

$$J_{op} = q\frac{D_p n_{ib}^2}{L_p N_d}\left[\frac{\frac{S_p L_p}{D_p}\cosh\left(\frac{X_j}{L_p}\right) + \sinh\left(\frac{X_j}{L_p}\right)}{\frac{S_p L_p}{D_p}\sinh\left(\frac{X_j}{L_p}\right) + \cosh\left(\frac{X_j}{L_p}\right)}\right] \tag{2.31}$$

$$J_{on} = q\frac{D_n n_{ie}^2}{L_n N_a}\left[\frac{\frac{S_n L_n}{D_n}\cosh\left(\frac{H'}{L_n}\right) + \sinh\left(\frac{H'}{L_n}\right)}{\frac{S_n L_n}{D_n}\sinh\left(\frac{H'}{L_n}\right) + \cosh\left(\frac{H'}{L_n}\right)}\right] \tag{2.32}$$

where n_{ie} and n_{ib} are the effective intrinsic carrier concentration in the top emitter and base, respectively.

Several authors [12,15,16] have shown that in order to obtain a good agreement between theoretical calculations and experimental results, incorporation of bandgap narrowing due to heavy doping is necessary. Slotboom's model [17] for bandgap

narrowing was used. The effective intrinsic carrier concentration is then expressed as:

$$n_i^2 = n_o^2 e^{\frac{q\Delta V}{KT}} \qquad (2.33)$$

where n_o is the intrinsic carrier density in the absence of bandgap narrowing. An empirical expression [17] for bandgap narrowing ΔV was used:

$$\Delta V = 9\left[\ln\frac{N}{10^{17}} + \left(\ln^2\frac{N}{10^{17}} + 0.5\right)^{1/2}\right] \qquad (2.34)$$

where $N = N_a$ for p-type and $N = N_d$ for n-type silicon material. Substituting Eqs. (2.25,2.30-2.34) into Eq.(2.29), V_{oc} can be calculated theoretically.

The fill factor, FF, defined as $V_m J_m / J_{sc} V_{oc}$ (where V_m and J_m are the current and voltage at maximum output power point), is a measure of the squareness of the J-V curve. For an ideal cell, FF can be expressed as [14]:

$$FF = \frac{V_m}{V_{oc}}\left[1 - \frac{e^{\frac{qV_m}{KT}} - 1}{e^{\frac{qV_{oc}}{KT}} - 1}\right] \qquad (2.35)$$

where V_m can be solved from the following equation:

$$V_{oc} = V_m + \frac{KT}{q}\ln\left(1 + \frac{qV_m}{KT}\right) \qquad (2.36)$$

Finally, the efficiency of the solar cell is obtained by:

$$EFF = \frac{FF\ V_{oc}\ J_{sc}}{P_i} \qquad (2.37)$$

where P_i is the incident light power density whose value is close to 100 mW for AM1 illumination condition.

To calculate photogenerated current and saturated recombination current, the following empirical expressions for minority carrier lifetime and diffusivity as functions of impurity concentration were used [11,12,18]:

$$\frac{1}{\tau} = \left[\frac{3.95x10^{-4}}{1 + \frac{N}{7.1x10^{15}}}\right]^{-1} + C\,N^2 \qquad (2.38)$$

where C is the Auger recombination coefficient, for electron: $N = N_a$ and $C = 9.9x10^{-32}cm^{-6}$; for hole: $N = N_d$ and $C = 2.8x10^{-31}cm^{-6}$. The diffusivities are calculated according to the following relations:

$$D_p = \frac{KT}{q}\frac{\mu_{po}}{\left[1 + \frac{350N_d}{(N_d+1.05x10^{19})}\right]^{1/2}} \qquad (2.39)$$

$$D_n = \frac{KT}{q} \frac{\mu_{no}}{[1 + \frac{81N_a}{(N_a+3.2x10^{18})}]^{1/2}} \qquad (2.40)$$

where D_p and D_n are the diffusivity for holes and electrons, and μ_{po} and μ_{no} are the intrinsic hole and electron mobilities, respectively.

2.4 Results and Discussions on Conventional n^+/p Cells

The effects of doping concentration and junction depth on J_{sc}, V_{oc}, and EFF for conventional cells are discussed in this section. To investigate the effects of the base doping concentration N_a, the emitter doping concentration N_d is held constant. Several authors have shown that the optimum N_d is about $10^{20}cm^{-3}$ [6,11]. This value was used in studying the effects of substrate doping concentration. We will check its the validity of this value at the end of this section.

In our calculations, s_n of 10^{15} and s_p of 10^6 cm/s were chosen. Fig.2.4 shows our calculated results for the total J_{sc}, base contribution J_n and contribution from depletion region J_d as a function of N_a (based on Eqs.(2.16,2.20,and 2.22)). It can be noted that although the contribution to J_{sc} from the base is the major factor, the contribution from depletion region is also important, and should not be neglected, especially when N_a is less than $10^{17}cm^{-3}$.

In practice, the intrinsic J_{sc} suffers a loss due to factors such as reflection from the front surface of the cell and the top metal coverage. A 10 % reduction is usually taken for the loss, which we also assume.

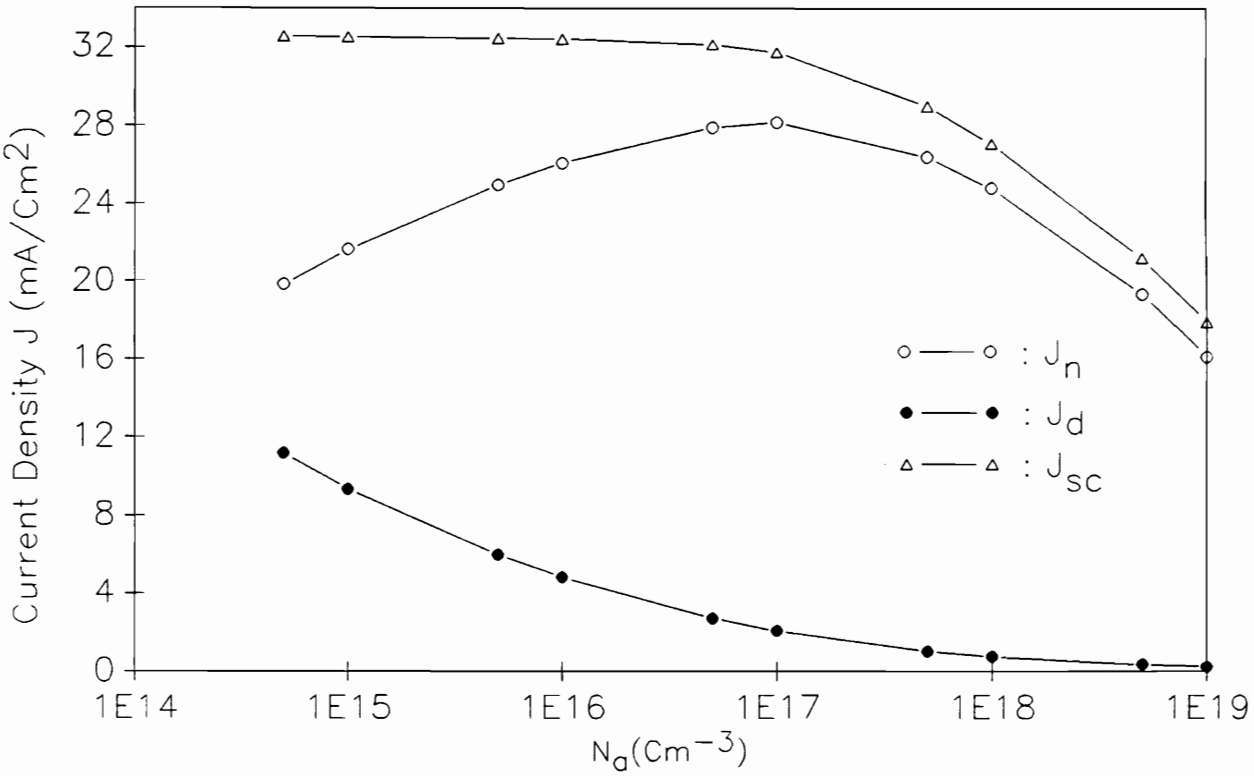

Fig.2.4 The total photocurrent (J_{sc}), the contribution from the base (J_n), and from the depletion region (J_d).

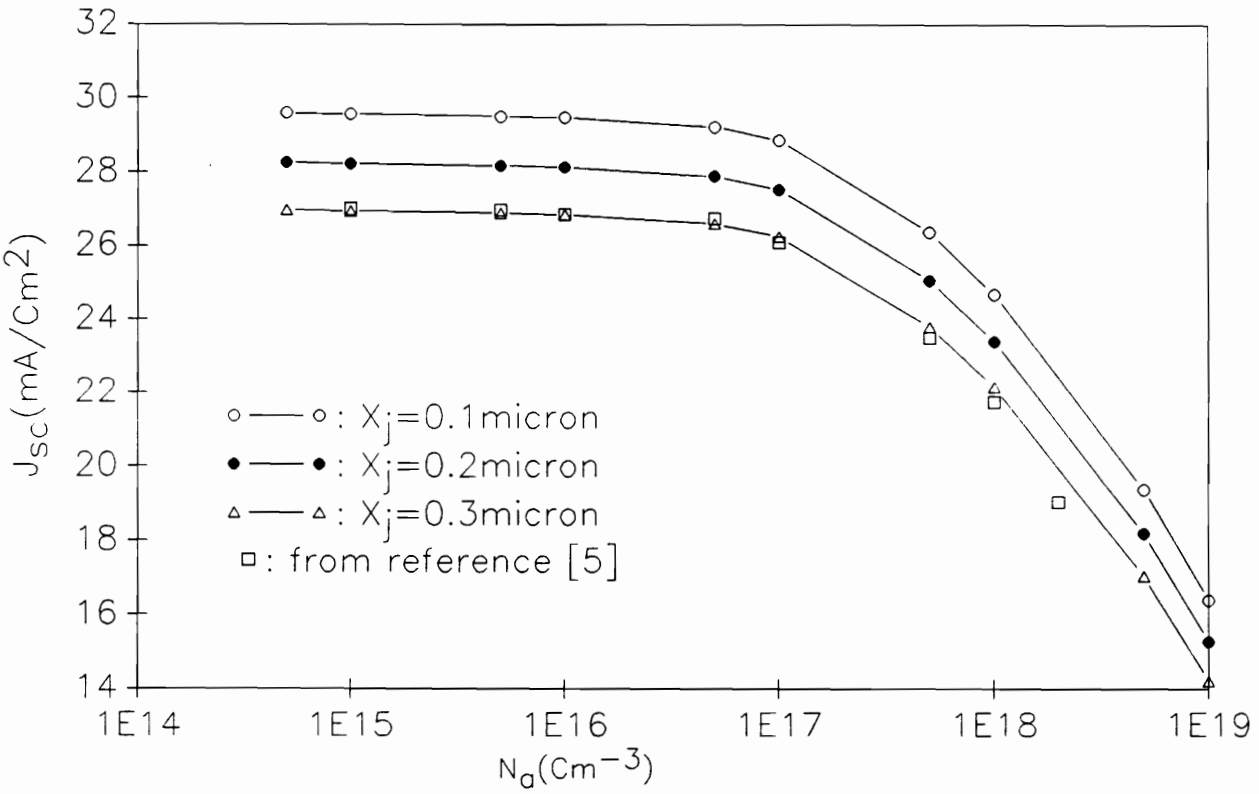

Fig.2.5 The short circuit current J_{SC} as a function of N_a for different junction depths X_j.

Fig.2.5 displays calculated J_{sc} as a function of N_a for three different junction depths x_j. It can be seen that J_{sc} decreases as N_a increases. This is because increased impurity concentration causes higher recombination in the base region due to impurity defects. It is also seen that lowering x_j from 0.5 to 0.1 μm results in successive improvements in J_{sc}. This indicates that surface recombination loss due to the high surface recombination velocity can be partly overcome by making the junction depth small. Our results show that a 20% increase in J_{sc} results from 0.5 to 0.1 micron reduction of x_j. The same conclusion was obtained by Fossum from numerical analysis [1]. Fig.2.5 also compares our calculations with numerical calculations from Lauwers et.al.[15], in which x_j of 0.3 μm was chosen. The results are very close.

V_{oc} as a function of N_a is shown in Fig.2.6. It can been seen that maximum V_{oc} is about 600mV when N_a is approximately $10^{17}cm^{-3}$. At low doping concentration (N_a is less than $10^{17}cm^{-3}$), V_{oc} increases with N_a due to the decrease of the saturation current. In the range of 10^{17} - $10^{18}cm^{-3}$, V_{oc} tends to saturate, and finally decreases with further increase of N_a because of the heavy doping effect on the minority diffusion length and the energy bandgap narrowing effect on n_i. The same results were obtained numerically by Lauwer, Overstraeten et.al.[15] and by Burgess and Fossum [19]. They found a maximum V_{oc} of 598 mV at N_a of $10^{17}cm^{-3}$. The result also agreed closely with measured values: 600 mV reported by Iles and Soclof[20], and 605 mV by Godewski et.al.[21]. Our calculations also indicated that junction

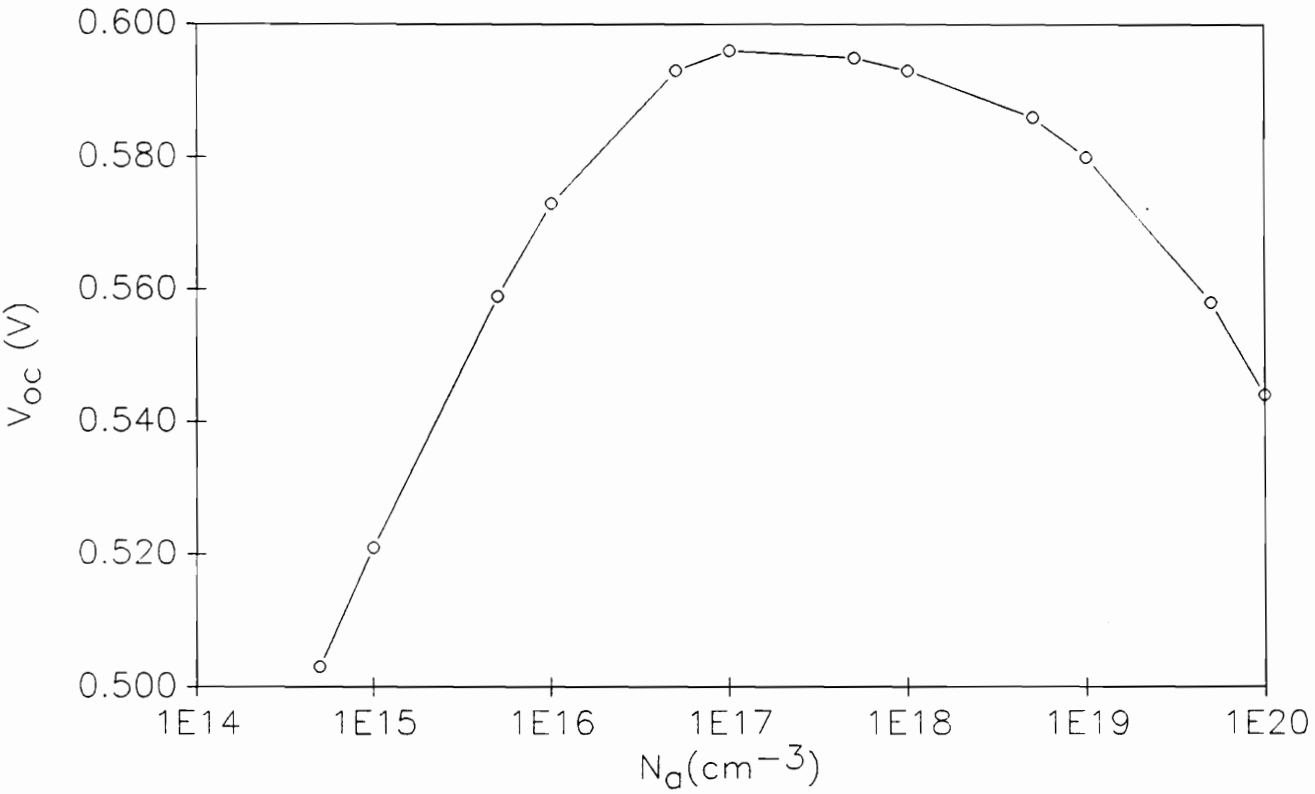

Fig.2.6 Open circuit voltage V_{oc} as a function of the base doping concentration N_a.

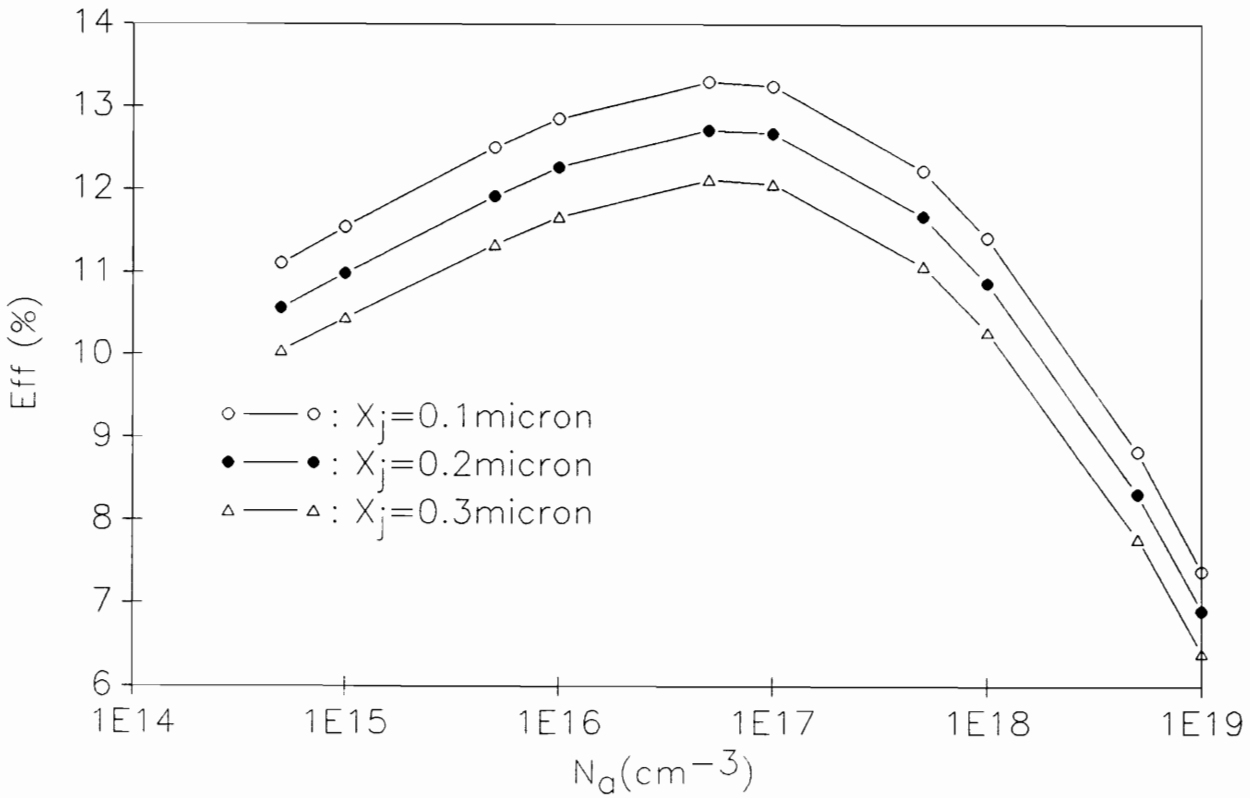

Fig.2.7 Efficiency EFF as a function of N_a for different junction depths X_j

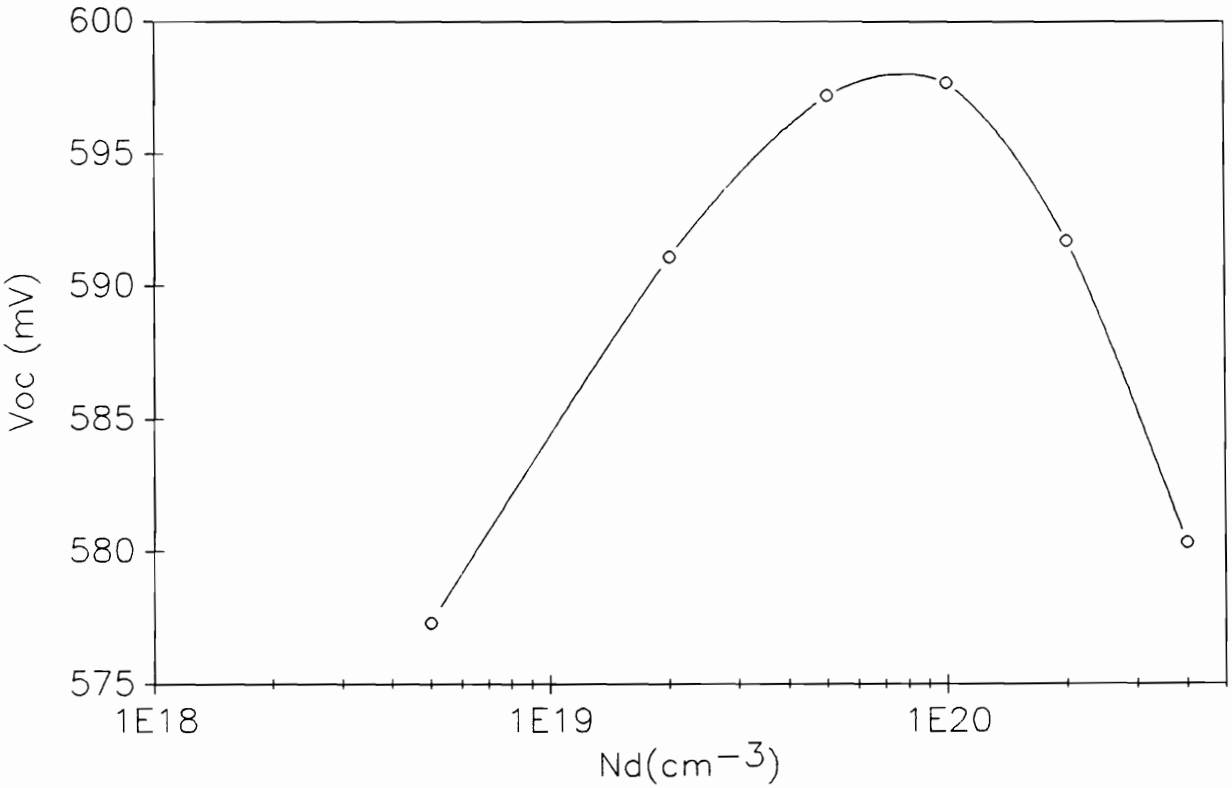

Fig.2.8 Open circuit voltage Voc as a function of diffused layer doping concentration Nd

depth has little effect on V_{oc}. V_{oc} changed about 0.3% as X_j varied from 0.5 to 0.1 μm.

Fig.2.7 shows the efficiency as a function of N_a for different x_j. The maximum values of EFF occur at N_a in the range $5x10^{16}$ to $1x10^{17}$ cm^{-3} for all x_j. The same conclusion has been reached with both numerical calculations and experimental results [15,19,20]. It can also be seen that x_j has a strong effect on efficiency. This is mainly because J_{sc} varies with x_j.

As stated at the beginning, an N_d of $10^{20}cm^{-3}$ is assumed to be an optimum n^+ layer doping concentration. We are now looking into the validity of this assumption. Fig.2.8 presents our calculation of V_{oc} as a function of N_d at N_a of $5x10^{16}$ cm^{-3}. The maximum V_{oc} does occur around N_d of $1x10^{20}cm^{-3}$. Our calculations also show that N_d has little effect on J_{sc}, (changing N_d from $1x10^{20}$ to $1x10^{19}$ cm^{-3}, the change in J_{sc} is less than 1%), so we may assume that the optimum N_d is mainly determined by V_{oc}. The results agree with the reports of other authors [6,11].

2.5 Surface Recombination Velocity Effects and High Efficiency Si Cells

In addition to recombination in the bulk Si, a loss of photogenerated minority carriers also takes place at the surface of the cells due to the presence of surface states arising from dangling bonds, and chemical contamination. The rate at which the minority carriers are lost at the surface is described by the surface recombination velocity S. The recombination velocity at the surface is of critical importance since

the number of carriers generated for a given wavelength of light is highest at the surface and decreases exponentially with the depth. The high value of S at the cell's front surface, together with the low diffusion length that usually occurs there, makes a shallow junction depth (0.3 micron or less) necessary to prevent a serious loss of photogenerated carriers. The surface recombination velocity at the back of the cell is not as critical as the front surface, but its importance increases as cells are made thinner. While shallow junction depth can partly prevent a serious loss of photogenerated current, it will result in some difficulties. It is hard to make a good junction which is very close to the surface, especially for a textured surface. Reducing the surface recombination velocity is another way to prevent the lose. Hovel has shown [14] that for lower value of surface recombination velocity (less than 10^3 cm/sec.), the efficiency of cells stays constant as the junction depth increases up to one micron. In recently developed high efficiency Si solar cells, a thin oxide layer is used to reduce the surface recombination velocity. A velocity of less than 10^2 cm/sec has been reported [22-25].

a. High Efficiency Silicon Cells

Over the last five years, there have been substantial improvements in silicon solar cell performance. Efficiency of the cells has increased from 14 percent to above 22 percent [22,24]. Most of this improvement results from using thermal oxide passivation to reduce surface recombination velocity. The contact area is generally the region of high recombination velocity. Maximum cell performance is obtained

when such contacts are passivated. Two major structures are widely used in high efficiency silicon solar cell technology.

The first structure is the Metal Insulator NP junction cell (MIPN) which employs top contact passivation by use of a thin oxide layer underneath the metal contact, as well as top surface passivation by a slightly thicker oxide layer. The difference in the thickness complicates the cell processing, but it is necessary to achieve maximum device performance [23]. The cell structure is shown in Fig.2.9 (a). In this structure, the use of a low work function metal such as Ti (for the contact layer) is essential in order to make an accumulation layer in the underlying silicon, which minimizes the contact recombination.

The second structure is the Passivated Emitter Solar Cell structure (PESC). The structure is shown in Fig.2.9 (b) [23]. It is similar to the MINP cell structure, except that electrical contact is made directly through narrow slots in the thin oxide. As a result, the contact passivation is obtained by minimizing the contact area.

Processing in both cases involves the diffusion of phosphorous junctions, the growth of the passivation oxide, and the etching of contact regions. A high quality thin oxide layer above the n^+ layer is desired in order to effectively reduce recombination velocity.

In addition to front surface passivation, rear surface passivation has recently been developed. Its advantage includes a better light trapping effect. The rear passivation becomes more important for thin cell applications. The structure of the Passivated

Emitter and Rear Cell, (PERC), is shown in Fig.2.9(c) [24,25]. This structure has been reported with an efficiency above 22 percent, the highest silicon cell efficiency so far. Three major features are included in this structure. The first is the use of inverted pyramids and a textured front surface to reduce reflection loss. The second is the use of a large number of holes through a passivation oxide layer to contact the cell rear surface. The third is the use of chlorine-based processing to obtain a high minority carrier diffusion length and to improve the quality of the passivating oxide [25]. In all of the above structures, surface passivated by a thin oxide layer is the key to reduce surface recombination velocity.

b. Surface Recombination Effects on Spectra Response

The internal spectral response is defined as the number of electron-hole pairs collected under short circuit condition relative to the number of photons entering the material, i.e.

$$SR(\lambda) = \frac{J_p(\lambda)+J_n(\lambda)+J_d(\lambda)}{qF(\lambda)(1-R(\lambda))} \qquad (2.41)$$

where λ is the wavelength of incident light, $F(\lambda)$ is the number of incident photons per cm^2 per sec. per unit bandwidth, and $R(\lambda)$ is the number of photons reflected from the surface. The reflection of light from the surface as a function of wavelength does affect spectral response, but in general the technology of anti-reflective coatings on the solar cell surface has been developed to such a degree that the reflection and its variation with wavelength can be ignored to a first degree approximation.

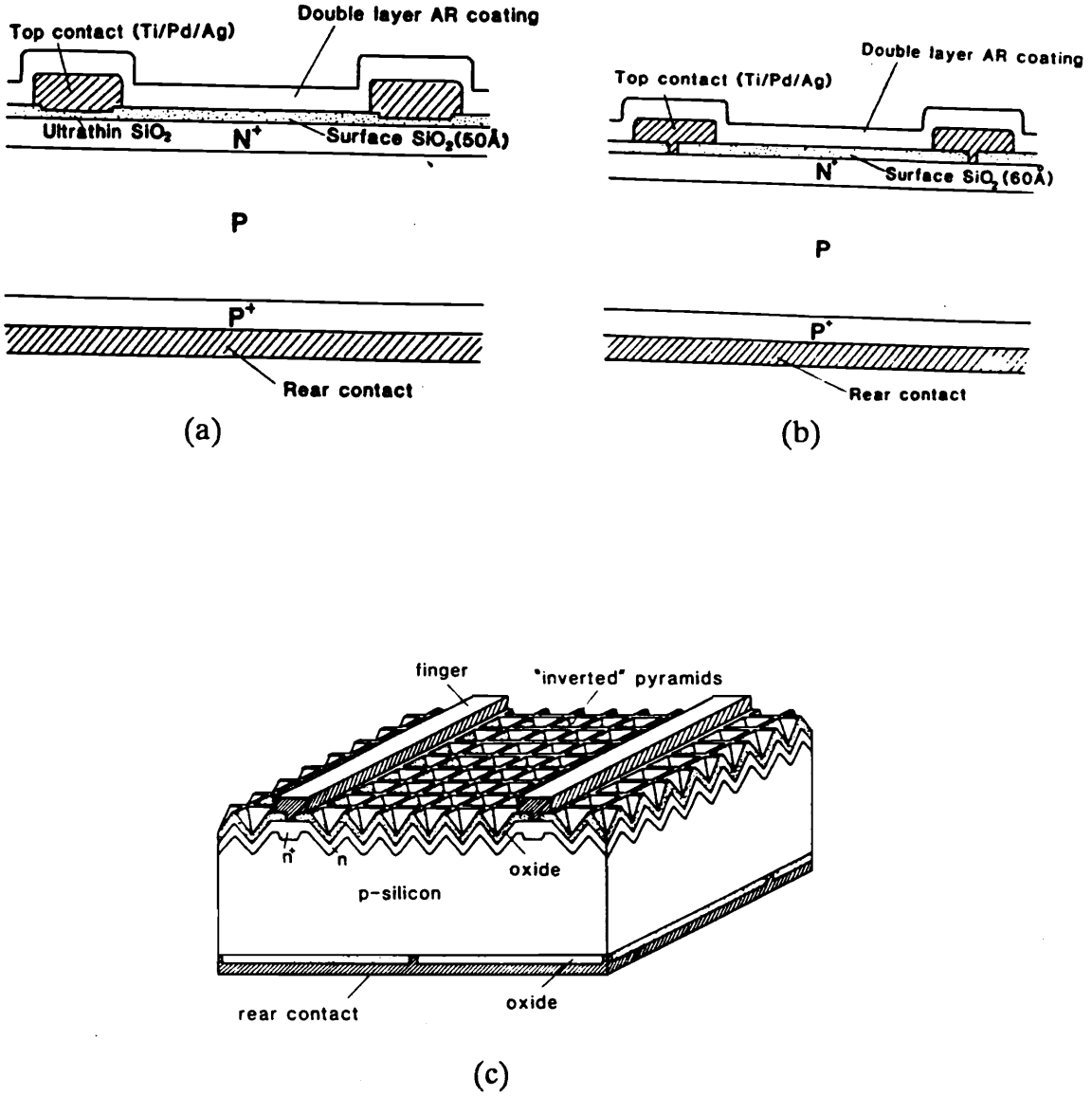

Fig.2.9 (a) The schematic of the Metal-Insulator-NP junction (MINP) solar cell. The major feature is the thin oxide layer over the surface and under the top metal contact (after [18]).
(b) The passivated emitter solar cell (PESC). The electrical contact is made directly through narrow slots in thin oxide. The passivation is obtained by minimizing the contact area (after [18]).
(c) The passivated emitter and rear cell (PERC). In this structure both front and rear surfaces are passivated by thin oxide layer (after [20]).

The analytical expressions of $J_p(\lambda)$, $J_n(\lambda)$ and $J_d(\lambda)$ for a uniformly doped n/p junction have been derived in ref.14. The total short circuit photocurrent at a given wavelength is then the sum of these three components, and the spectral response is obtained by Eq.(2.41). Calculated results are shown in Fig.2.10 for a silicon n/p cell with varying surface recombination velocity. It is seen from Fig.2.10 that the spectral response at high photon energy is very sensitive to the surface recombination velocity. This is because at high photon energy, all of the carriers are generated near the surface due to the high absorption coefficient. Thus the losses due to high recombination velocity at the front of the cell are critical. Fig.2.10 also shows that for S_p less than 10^3cm/sec., the spectral response is very close to unity.

c. Effects of Surface Recombination Velocity and Diffusion Length on J_{sc}, V_{oc}, and EFF

For a high efficiency solar cell, low the surface recombination velocity and long diffusion length are desired. J_{sc}, V_{oc}, and EFF varying with the diffusion length and surface recombination velocity were studied based on the analytical approach developed in section 2.3.

The short circuit current as a function of the diffusion length for different surface recombination velocities has been computed using Eqs.(2.16,2.20,2.22,and 2.29). The results are shown in Fig.2.11. It can be seen that J_{sc} increases with L in the region of L less than 60 μm, after which J_{sc} tends to saturate with a further increase of L.

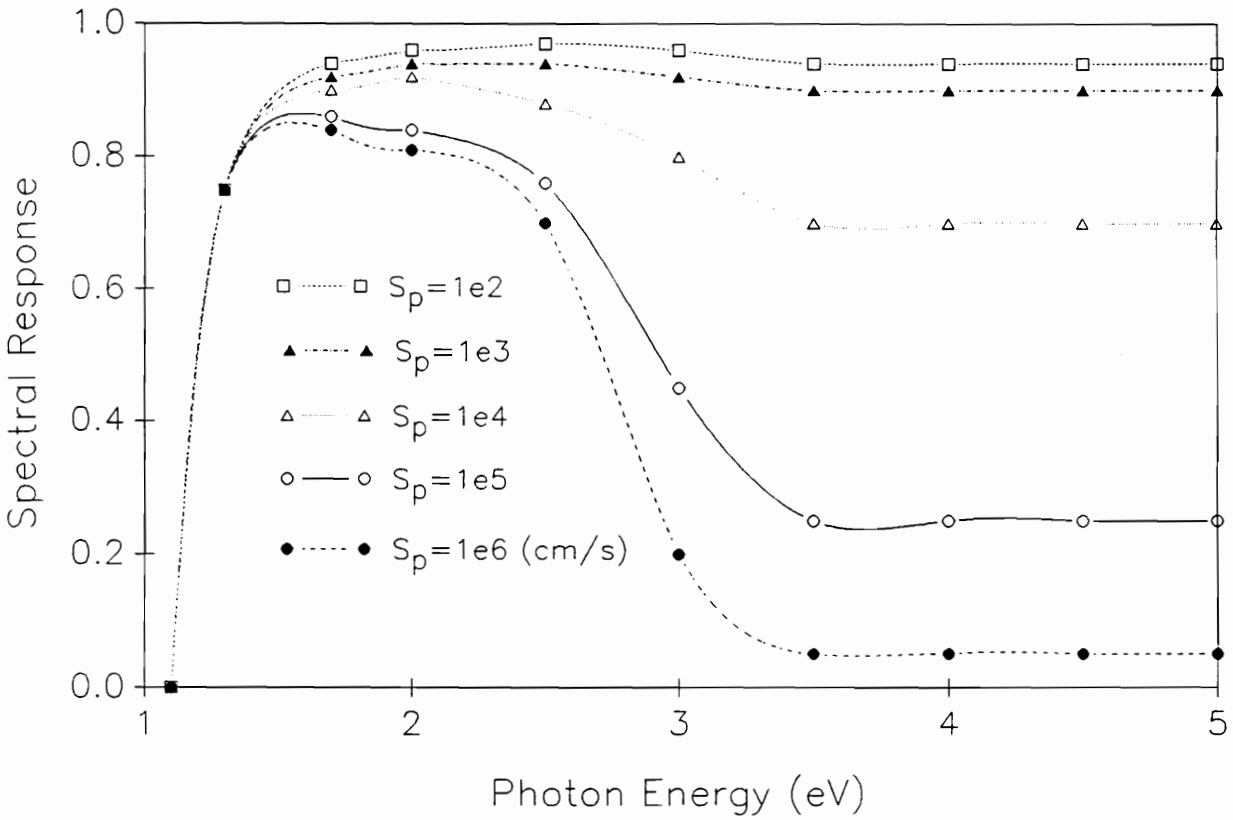

Fig.2.10 Spectral response vs. photon energy for different surface recombination velocities S_p

It is also seen that J_{sc} increases with a decrease of S_p. It should be noted that J_{sc} is very sensitive to S_p in the range of 10^4 to 10^6 cm/sec. and becomes less sensitive in the regions of S_p below 10^4, or above 10^6 cm/s.

The saturation current J_o as a function of L has been calculated by using Eqs.(2.30-2.32). The result is shown in Fig.2.12 in which J_o decreases rapidly with increasing L in the low L region and changes slowly for large L. It should be noted that J_o is not a function of the front surface recombination velocity S_p, even though S_p appears in the expression for J_{op}. This is because in an n^+/p cell, the doping concentration in the top layer is much higher than that in base region. In general, J_{on} is larger than J_{op} by two orders of magnitude. Thus J_{on} is the dominate term in J_o. Since J_{on} is independent of S_p, J_o is not sensitive to S_p.

V_{oc} as a function of L for different S_p is presented in Fig.2.13 It is seen that V_{oc} increases fast with L in low L region (L less than 40 μm) and then the increase becomes slower for larger L (L greater than 80 μm). It is also seen that V_{oc} increases with decrease S_p, but is not as sensitive as J_{sc} to S_p. V_{oc} increases by about 10 mV when S_p is reduced from 10^6 to 10^2 cm/sec.. The calculated results of cell efficiency EFF as a function of L for different S_p are presented in Fig.2.14. We see that EFF is very sensitive to S_p, and increases approximately 40 percent as S_p decreases from 10^6 to 10^2 cm/sec.. Fig.2.14 also shows that for a cell with long diffusion length and low front surface recombination velocity, the efficiency will be greater than 22%. This agrees with the experimental results of high efficiency silicon

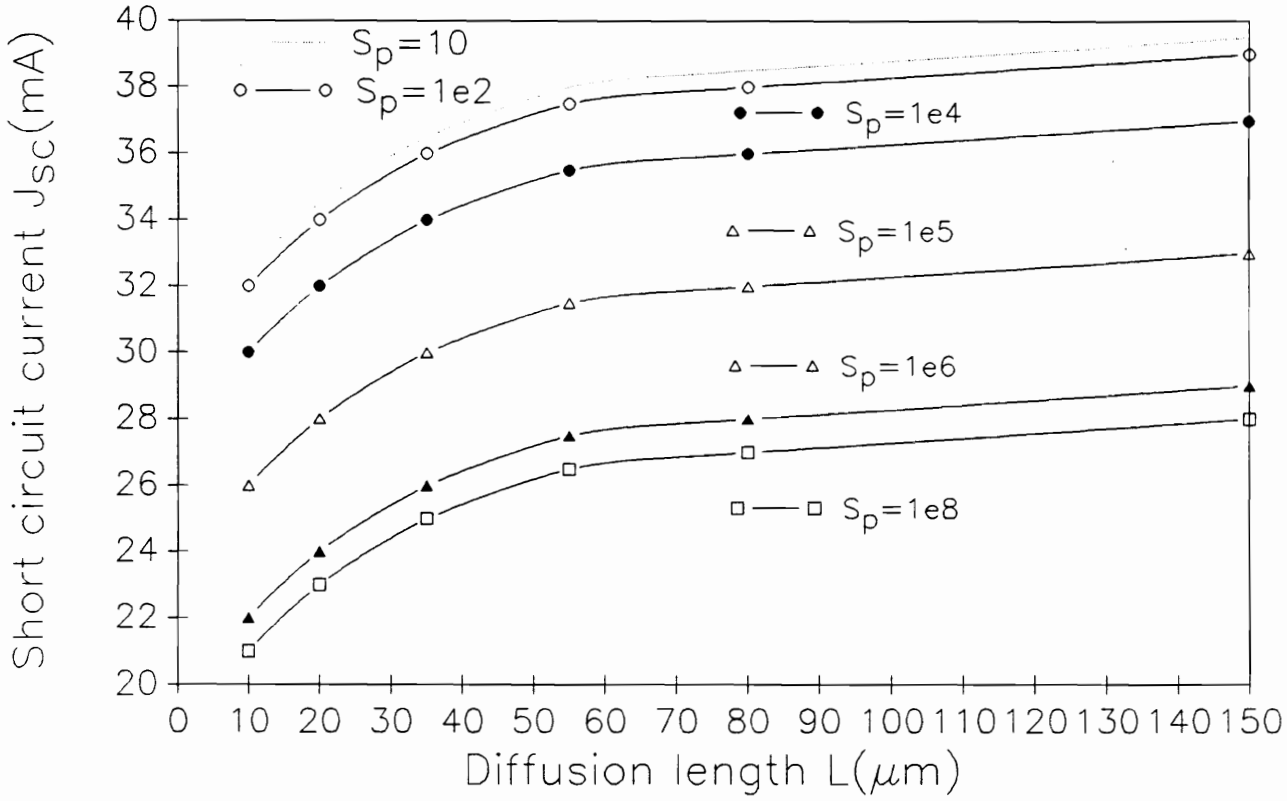

Fig.2.11 J_{SC} Vs. L for different surface recombination velocities S_p(cm/sec)

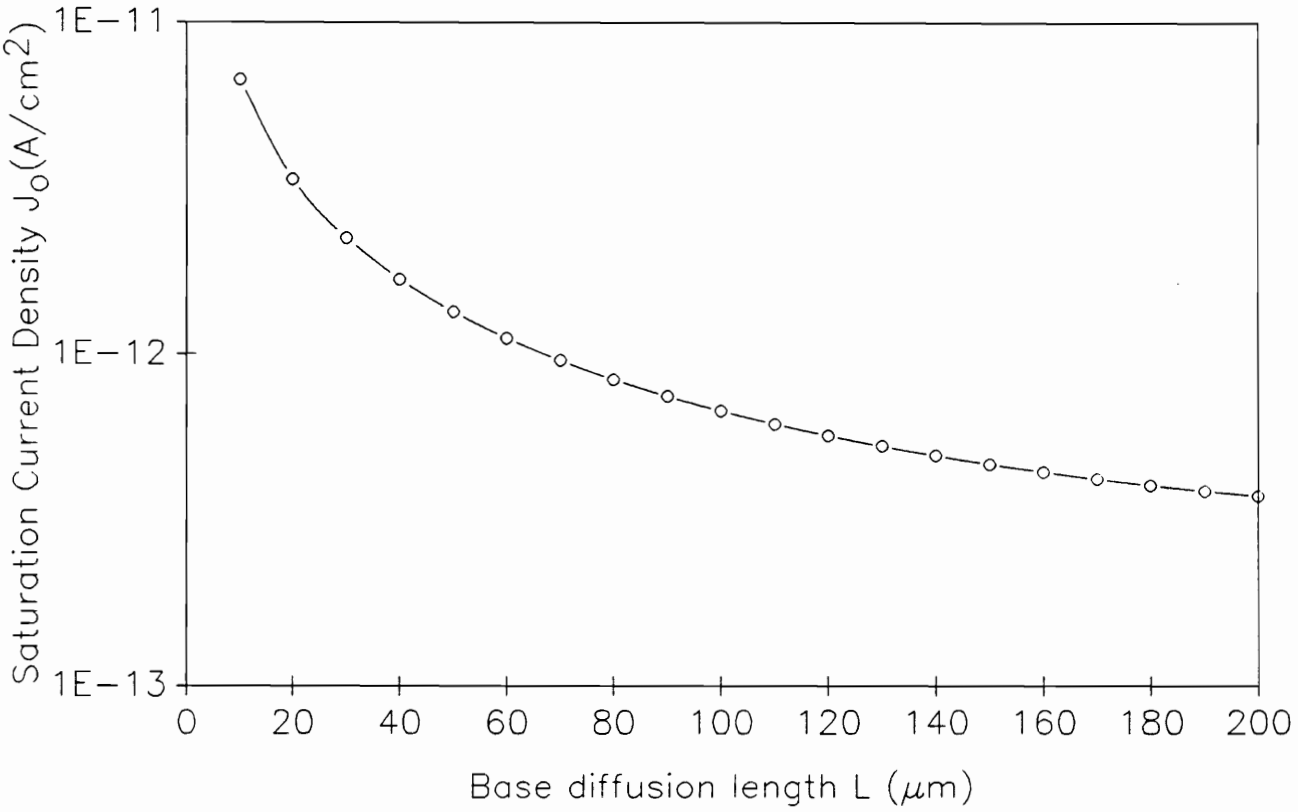

Fig.2.12 J_O as a function of the diffudion length L.

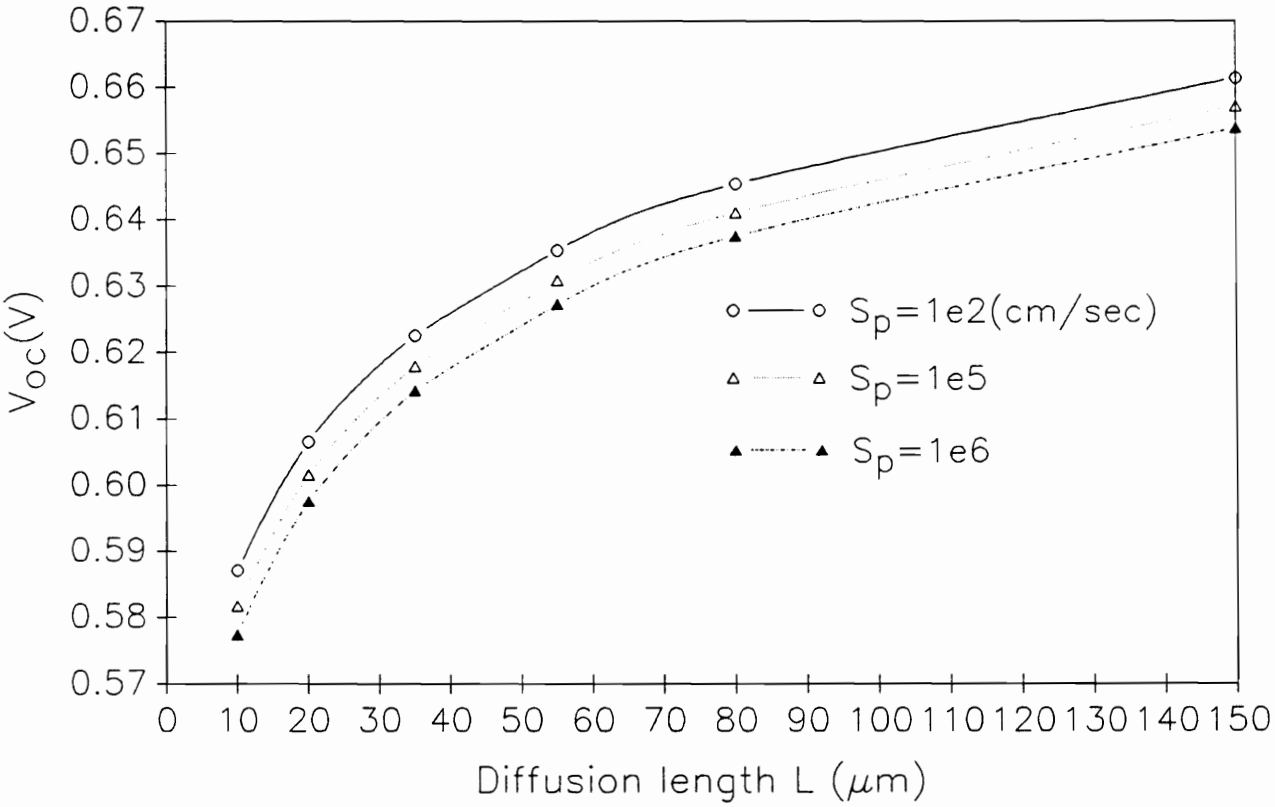

Fig.2.13 V_{OC} Vs. L for different surface recombination velocities S_p

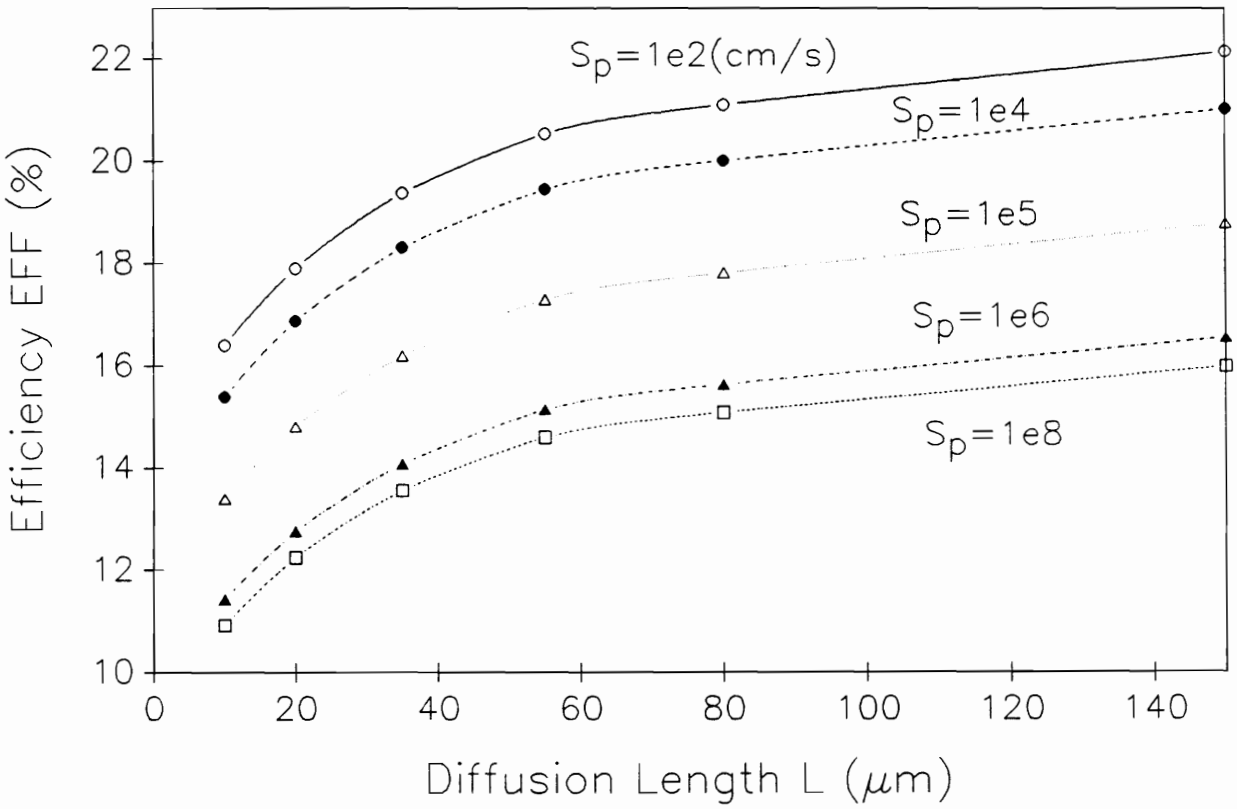

Fig.2.14 Efficiency as a function of diffusion length L for different values of S_p

cells [22-25].

2.6 Conclusions

A new expression for the short-circuit photogeneration current of the n^+-p silicon solar cell has been developed. The analytical approach simplifies the solar cell analysis and enables one to do the calculations with a personal computer. Calculations have been made for J_{sc}, V_{oc}, and EFF as a function of the base region doping concentration N_a, junction depth x_j, surface recombination velocity S_p and diffusion length L. The results show that x_j has a significant influence on J_{sc}, and EFF, whereas, V_{oc} is insensitive to x_j. And all these three parameters strongly depend on doping concentration in the base region. The optimum doping concentration is found to be in the range of $5x10^{16}$ to $1x10^{17}$ cm^{-3}. The calculated results of J_{sc}, V_{oc}, and EFF were in close agreement with previous experimental results and numerical analysis. The studies of surface recombination velocity effects show that the efficiency is very sensitive to the recombination velocity, and that for a high efficiency cell (EFF > 22 %), an S_p of lower than 10^3 cm/sec. is desired.

References

[1] J.G. Fossum, Solid-State Electron. Vol.19, p269,1976.

[2] P.M.Dunbar and J.R.Hauser, Solid-State Electron. Vol.19, p96,1976.

[3] M.Wolf, IEEE Trans. Electron Dev. ED-27, 751, 1980.

[4] H.C.Hsieh, C.Hu and C.I.Drowley, IEEE Trans. Electron Dev.ED-27, p883, 1980

[5] J.Furlan and S.Amon, Solid-State Electron. Vol.28, P1241, 1985.

[6] S.Noor Mohammad,J.Appl.Phys.61(2),p767,15 January 1987.

[7] F.L.Bauer, H.Rutishauser and E.Stiefel, Proceedings of Symposia in Applied Mathematics, xv, 99199-218, American Mathematical Society, Providence.R.I.1963. 2.7, H.R.Philipp, J.Appl.Phys., Vol.43, No.6, P2835, June 1972.

[8] H.R.Philipp, J.Appl.Phys., Vol.43, No.6, P2835, June 1972.

[9] J.J.Wysocki, Solar Energy, Vol.6, No.3, P104, 1962.

[10] M.Wolf, Proc. IEEE 48, p1248, 1960.

[11] Ming-Jer Chen and Ching-Yuan Wu,Solid-State Electron. Vol.28,p751,1985.

[12] Wen-zen Shen and Ching-yuan Wu,J.Appl.Phys.51(1),p466,1980.

[13] S.M.Sze,Physics of Semiconductor Devices,1981 by John Wiley & Sons Inc.

[14] H.J.Hovel,Semiconductors and Semimetals.Vol.11,Solar Cell,1975.

[15] P.Lauwers,R.Van Overstraeten et al.Solid-State Electron.Vol 21,p747,1977.

[16] H.P.D.Lanyon, Solar Cells, Vol 3,p289,1981.

[17] J.W.Slotboom, Solid-State Electron.Vol.20,p279,1977.

[18] J.G.Fossum, Solid-State Electron,Vol.19,p504,1976. C.Wyn et al. IEEE Trans. Nucl.Sci. Ns-14,p153,1967.

[19] E.L.Burgess and F.G.Fossum,IEEE Trans.on Electron Devices,Vol.ED-24,p433,1977.

[20] P.A.Iles and S.I.Soclof,11th IEEE Photo.Spec.Conf.p19,1975.

[21] M.P.Godlewski,H.W.Brandhorst,Jr.,and C.R.Baraona,11th IEEE Photo.Spec.Conf.,p32,1975.

[22] R.A. Sinton, Yong Kwark, J.Y. Gan and R.M. Swanson, IEEE Electron Device Letter, Vol. EDL-7, No.10, October 1986

[23] Martin A. Green, High Efficiency Silicon Solar cell, Trans. Tech. Publication, 1987.

[24] A.W. Blakers, A. Wang, A.M. Milne, J. Zhao and M.A. Green, Appl. Phys. Lett. 55 (13) Sept.1989, p1363.

[25] M.A. Green, A.W. Blakers, A. Wang, A.M. Milne, J. Zhao and X. Dai, IEEE. Transactions on Electron Device Vol.37, No.2, 1990, p331.

Chapter 3

Electrical Properties of Poly-Si

3.1 Introduction

Polysilicon is a promising material for terrestrial photovoltaic applications. The efficiency of polycrystalline solar cells is limited by the minority carrier recombination loss at grain boundaries. Optimum designs of polysilicon solar cells and other bipolar devices can be achieved only if the effects of grain boundary (GB) on the minority carrier transport are well understood.

In the past, several valuable investigations have been made on the properties of polysilicon under optical illumination [1-7]. Card and Yang first studied the effects of optical illumination on the GB barrier height (V_g) and pointed out that V_g could be reduced from its dark value by the presence of illumination [1]. The analysis of Seager [2] and Fossum et.al.[3] provided valuable insight into recombination mechanism in grain boundaries.

In previous models, however, the nonuniform solar illumination effects, and the depth variation of minority carrier transport parameters, have not been addressed. The nonuniform photogeneration in a solar cell is a practical situation, and the depth dependence of minority carrier transport parameters is important for poly-Si. A practical relation between photogeneration rate and the GB V_g is needed to

understand the properties of poly-Si under illumination. Recently, the grain size effect on the GB V_g under illumination has been studied by Joshi et.al.[4-6], and several relations of the GB V_g were proposed. In their calculation of V_g, however, the minority carrier diffusion length L was assumed as a constant parameter. It may not be a good approximation because L should be a function of the GB V_g, as is described in next section. Another expression for V_g was proposed by Dimitriadis et.al.[7]. In their analysis, the GB potential V_g under illumination was expressed as a function of V_{go} (the GB potential in dark). But in their treatments the Fermi-function in dark f_o was assumed to be $<< 1$, and $(1 - f) \approx 1$ was used (f is the Fermi-function under illumination). This approximation, in fact, is good only for very low doping concentration, e.g. for $N < 10^{15}cm^{-3}$. Additionally in their model, the value of V_{go} and the trap density N_{ts} were treated as two independent parameters. These approximations may oversimplify the problem.

We tried to limit the number of assumptions and parameters used in our model to keep the model applicable to a reasonably broad range of physical situation. In this chapter, starting with an initial equilibrium (dark) V_{go} which can be expressed as a function of N, N_{ts} and the Fermi-function f_o at the GB region, a new expression for V_g under illumination is developed by introducing a quasi Fermi-function (f). The f was solved by considering the dynamic balance between capture and emission of carriers at the GB trap states. By using this new relation, the minority transport properties and their depth variations are developed.

3.2 General Considerations

Polysilicon material consists of crystallites joined together by grain boundaries. Each crystallite can be considered as a single crystal. The grain boundary consists of a layer of disordered atoms which is a transitional region between different orientations of neighboring crystallites. In this region, there are a large number of defects due to incomplete atomic bonding. This results in the formation of high density trapping states. These trap states are capable of trapping carriers and immobilizing them [8-10]. The chemical potential for majority carriers in grain boundary is also shifted down from the grain value due to the lack of perfect periodicity [11]. The lower chemical potential and the high trap density will make influx of majority carriers into grain boundary region to fill the trap states. Once filled, the traps become electrically charged and a space charge region is generated nearby, which is a barrier for further flow of the majority carriers. These filled trap states act as recombination or scattering centers for the minority carriers. Therefore minority carrier transport is controlled by the amount of filled trap states, which are in turn controlled by the grain boundary potential barrier height. To calculate the grain boundary potential, a knowledge of the trap density of states and its distribution in grain boundary is needed, those depending on the sample preparation processes. It is generally agreed that the trap states are located near the middle of the energy gap, and a monoenergetic trap level model is a suitable model. This can explain the

difference in grain boundary potential for n- and p-type polysilicon, and the resistivity data [10-16]. The single trap energy level model was also assumed in this work. In real polysilicon material, the grain size and geometry are irregular. There is no distribution function available to describe real materials, especially for large grain samples. To simplify the analysis, the following assumptions were made in our calculations:

1) The material is composed of identical cubic grain of dimension d.

2) A single trap energy level exists at energy E_t.

3) The depletion approximation is used in GB space charge region.

4) Impurity atoms are completely ionized and uniformly distributed.

5) Carriers trapped in the GB come from the GB space charge region.

3.3. The GB potential in dark V_{go}

Applying the neutralization condition to the GB and its space charge regions, V_{go} can be determined. This is done by equating charge in the GB (Q_t) to that in GB space charge regions (Q_s). The Q_t is given by

$$Q_t(cm^{-2}) = qN_{ts}f_o(E_t, E_f) \qquad (3.1)$$

where N_{ts} is the grain boundary trap density of states per cm^2, and $f_o(E_t,E_f)$ is the Fermi probability function in the GB region. By considering two space charge regions for each boundary Q_s can be expressed by

$$Q_s = 2\ q\ W\ N \qquad (3.2)$$

where N is the doping concentration, W is the depletion region width which is determined by solving Poisson's equation in the space charge region, viz.

$$W = \left(\frac{2\epsilon V_{go}}{qN}\right)^{1/2} \qquad (3.3)$$

where ϵ is the dielectric constant.

From the electrical neutrality condition ($Q_t = Q_s$), and using Eqs.(3.1, 3.2 and 3.3) we have an expression for the GB potential

$$V_{go} = \frac{qN_{ts}^2}{8\epsilon N} f_o^2 \qquad (3.4)$$

in which f_o is defined as

$$f_o = \frac{1}{1 + e^{(E_t - E_f)/kT}} \qquad (3.5)$$

where E_t is the trap energy level and E_f is the Fermi energy level in GB region. For holes the Fermi-function is $(1 - f_o)$.

Eq.(3.5) for f_o describes the probability of an electron filling a trap state in terms of $(E_t-E_f)/kT$, but the quantity of (E_t-E_f) is generally unknown in the GB region. In order to calculate V_{go} by Eq.(3.4), we need a more useable form for f_o. By using Boltzmann statistics, the carrier density in GB is given by

$$n = Ne^{-qV_{go}/kT} \tag{3.6}$$

and n can also be expressed as

$$n = n_i e^{(E_f - E_i)/kT} \tag{3.7}$$

Therefore, one obtains

$$e^{(E_t - E_f)/kT} = \frac{n_i}{N} e^{(qV_{go} + E_t - E_i)/kT}$$

Thus, f_o can be expressed as

$$f_o = \frac{1}{1 + \frac{n_i}{N} e^{(qV_{go} + E_t - E_i)/kT}} \tag{3.8}$$

where n_i and E_i are the intrinsic carrier density and Fermi level in the GB. Substituting Eq.(3.8) into Eq.(3.4), V_{go} can be represented as follows:

$$V_{go} = \left(\frac{qN_{ts}^2}{8\epsilon N}\right) \left[\frac{1}{1 + \frac{n_i}{N} e^{(qV_{go} + E_t - E_i)/kT}}\right]^2 \tag{3.9}$$

Eq.(3.9) pertains to n-type material. For p-type, considering that the probability of a hole filling a trap state equals (1 - f_o), and following similar derivation as in n-type, it turns out that Eq.(3.9) is also true for p-type if (E_t-E_i) is replaced by (E_i-E_t). By fitting experimental data of resistivity, (E_i-E_t)≈0.17eV was determined for p-type polysilicon [10,14], and (E_t-E_i)≈0.066eV was chosen for the n-type [11]. These two values were used in our calculations. Therefore, Eqs.(3.8) and (3.9) allow one to

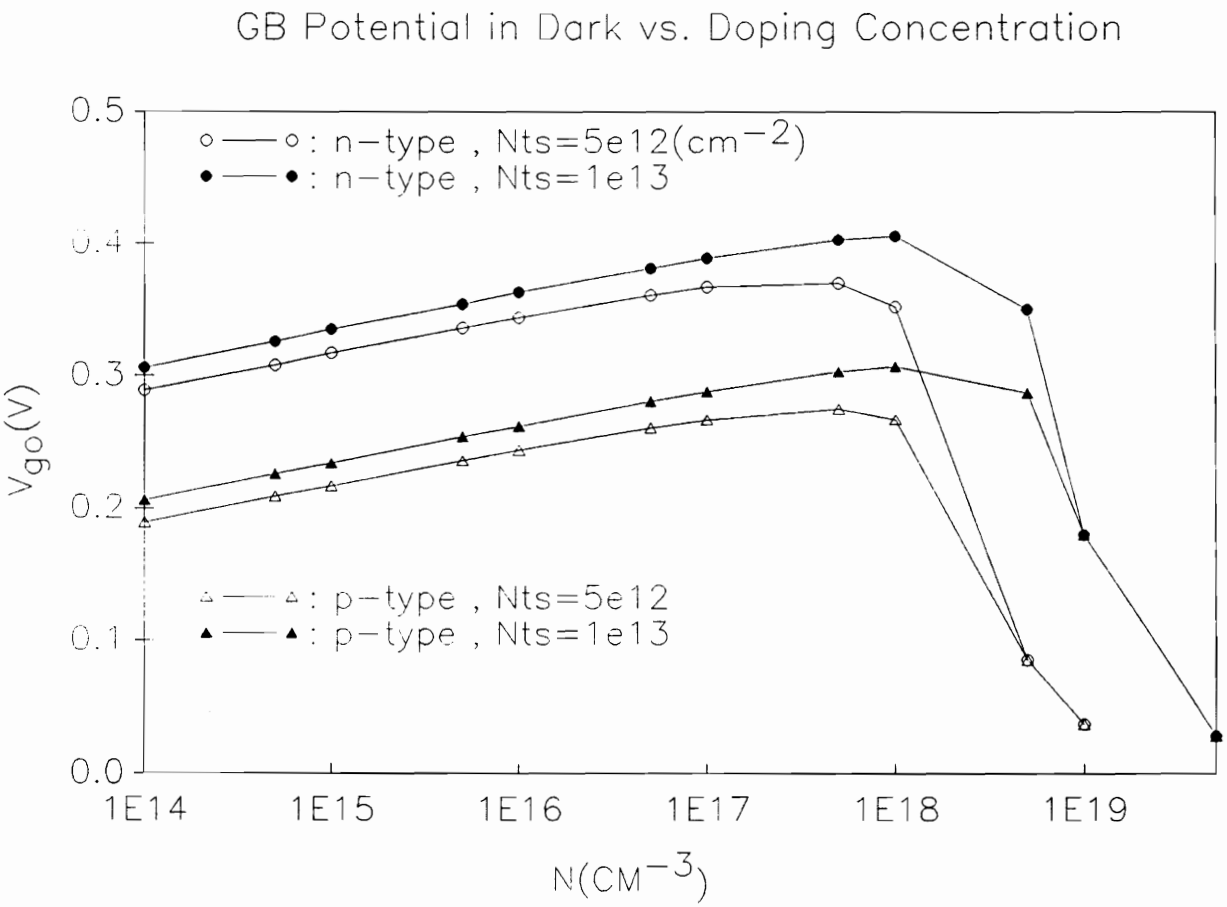

Fig.3.1 V_{go} as a function of doping concentration for both n and p type poly-Si at different Nts

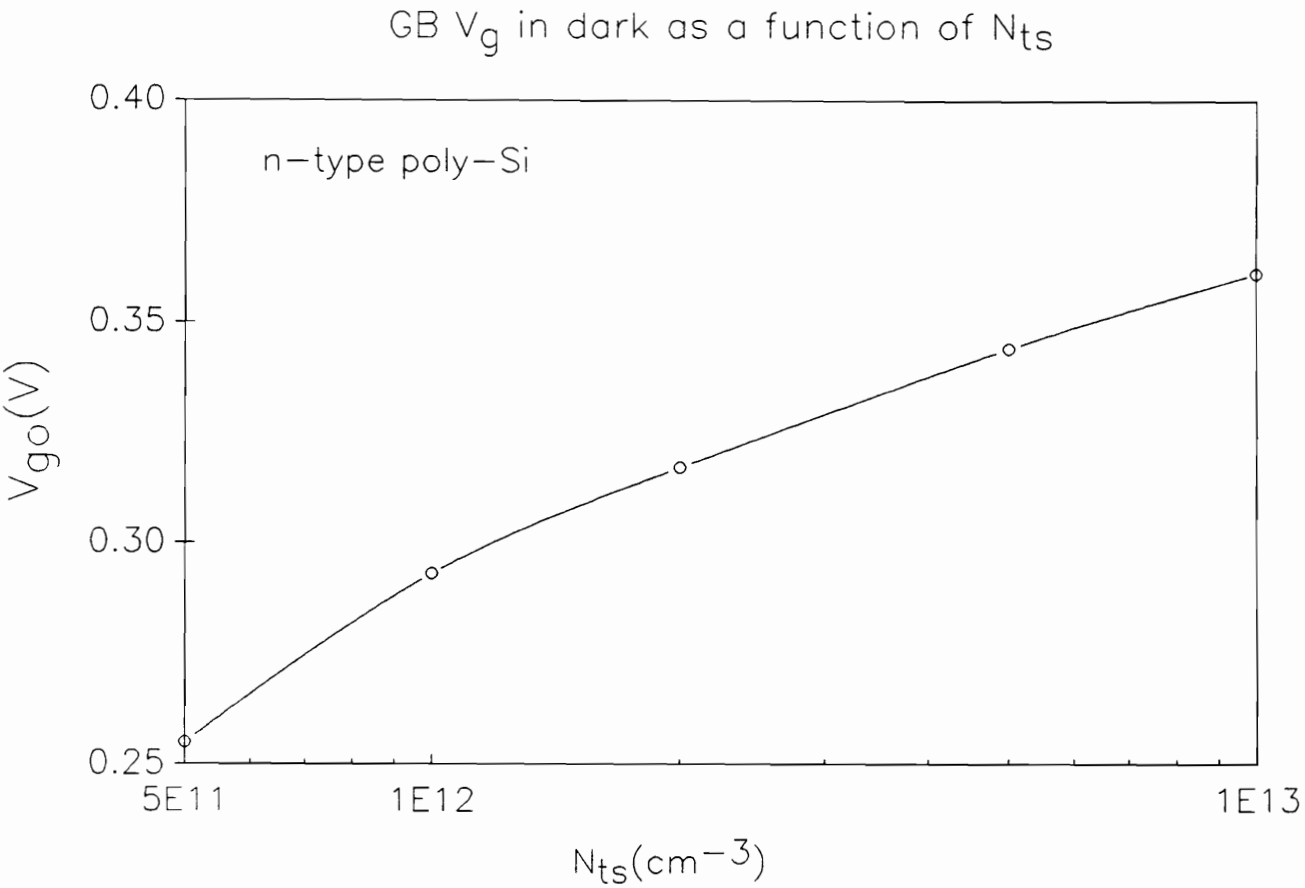

Fig.3.2 The variation of V_{go} with trap density N_{ts} at doping concentration of N=1E16 CM^{-3}.

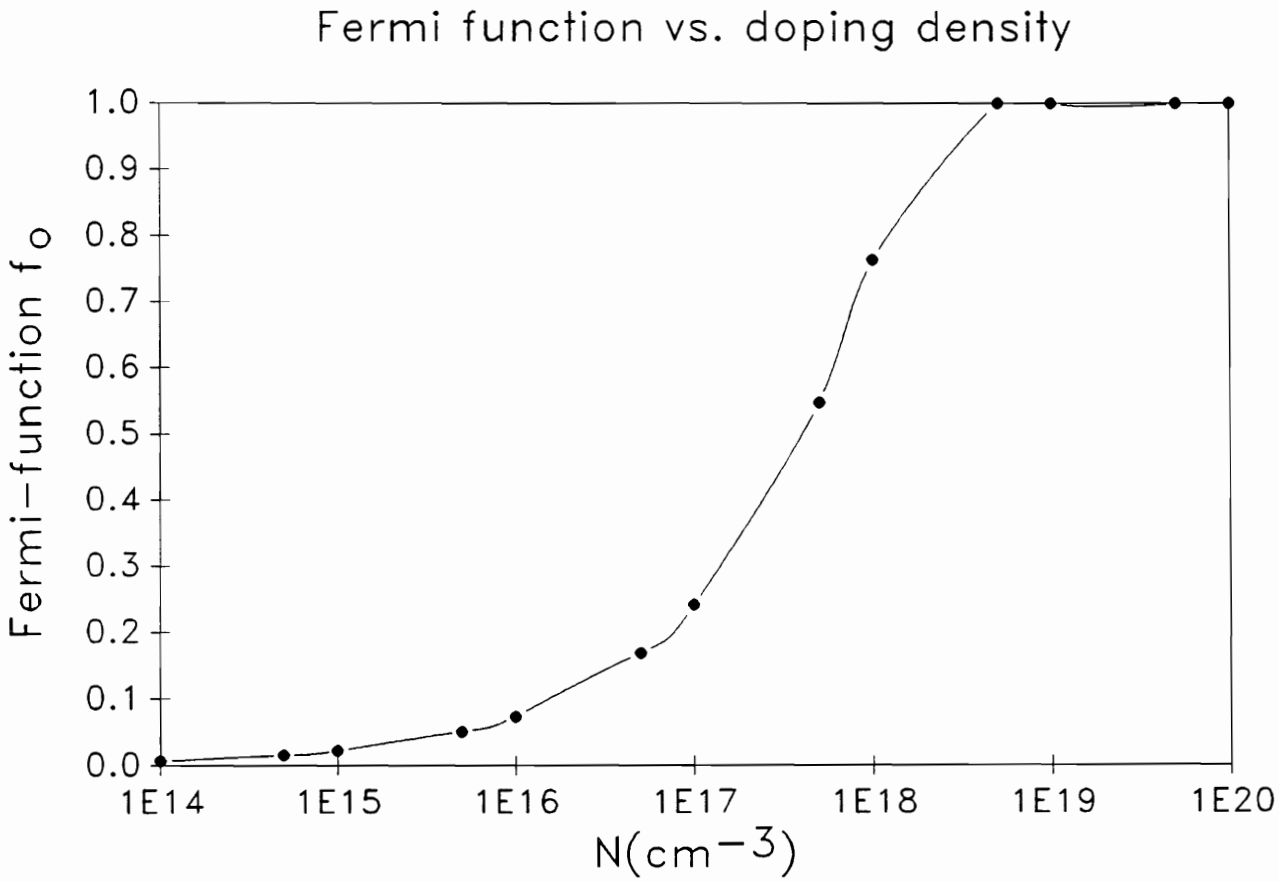

Fig.3.3 Fermi function variation with doping concentration for $N_{ts}=5x10^{12}(cm^{-2})$

calculate V_{go} and f_o under equilibrium condition.

Fig.3.1 shows the calculated V_{go} as a function of doping density N for both n- and p-type poly-Si at different trap densities N_{ts}. The variation of V_{go} with N_{ts} for n-type is shown in Fig.3.2. The equilibrium Fermi-function f_0 as a function of N is shown in Fig.3.3. It can be seen that f_o increases rapidly with N and saturates at N of about $10^{19}cm^{-3}$. It is noted that only at low doping is $f_o \approx 0$ satisfied.

3.4 The GB potential V_g under illumination

Under optical illumination, a new occupancy of trap states will be established, and the equilibrium Fermi function should be replaced by the quasi-Fermi function. The minority carriers generated by the illumination will be attracted electrically to the charged trap states which were filled by the majority carriers. Recombination will occur at the GB, and the accumulated charge will be reduced until a new balance is reached. The new balance leads to reduction of the GB potential from its dark value. In order to describe this reduction quantitatively, a relation between illumination level and V_g is desired. Eq(3.4) gives V_g in dark, a limiting case of illumination. All the quantities before f_o on the right side of Eq.(3.4) should not change significantly with illumination. The GB potential barrier height under illumination can thus be expressed as

$$V_g = \frac{qN_{ts}^2}{8\epsilon N} f^2(E_t, E_f) \qquad (3.10)$$

Here a quasi-Fermi function f is introduced, which is a function of illumination. Combining Eq.(3.10) and (3.4), the V_g can be expressed as

$$V_g = V_{go}\beta^2 \qquad (3.11)$$

where ß=f/f_o, the ratio of quasi-Fermi function under illumination to the Fermi function at equilibrium. The ß and f can be solved by considering the dynamic balance between capture and emission of carriers at GB trap states. Under steady illumination condition, the carrier photogeneration rate is given by

$$G = (R_c - R_e) \qquad (3.12)$$

where G is the photogeneration rate, R_c and R_e are the capture and emission rate respectively

$$R_c = \sigma V_{th} n\, N_t (1-f) \qquad (3.13)$$

$$R_e = \sigma V_{th} n_1\, N_t f \qquad (3.14)$$

where n is the majority carrier density in GB region, N_t is the trap density states per (cm^3) σ and V_{th} are the capture cross-section and thermal velocity for majority carriers respectively, and n_1 is given by

$$\begin{aligned} n_1 &= n_i\, e^{(E_t - E_i)/kT} \quad (for\ n\text{-}type) \\ p_1 &= n_i\, e^{(E_i - E_t)/kT} \quad (for\ p\text{-}type) \end{aligned} \qquad (3.15)$$

Substituting Eqs.(3.13) and (3.15) into Eq.(3.12) and using Eqs.(3.6) and (3.11), we obtain

$$G = \sigma V_{th}\left(\frac{6N_{ts}}{d}\right)\left[Ne^{-qV_{go}\beta^2/kT}(1 - \beta f_o) - n_1\beta f_o\right] \qquad (3.16)$$

where d is grain size, and $N_t=6N_{ts}/d$ [1].

Since V_{go} and f_o can be determined by equations (3.8) and (3.9), if G is given, ß can be solved from Eq.(3.16) and the quasi-Fermi function f and GB potential V_g under illumination can also be determined.

It should be noted that if G is set equal to zero in Eq.(3.16), replacing n_1 and f_o (Eqs 3.8 and 3.15) into Eq.(3.16), we have the solution of ß=1. This is just what is expected, since, when G=0, the value of the quasi-Fermi function should be the same as the Fermi-function at the equilibrium condition. Eq.(3.16) is valid for both dark and light cases, so the sufficient illumination condition is not necessary in applying Eq.(3.16), which was required in previous works [2,6].

Using Eq.(3.16) allows one to calculate the dependences of the barrier height on the trap density, grain size and doping concentration. In particular, it provides a relationship between G and V_g. It is a basic relation utilized in our investigations on

---

1. Since for a cubic grain with a side of length d, the number of grains per unit volume is $1/d^3$, the total grain boundary surface area per cube is $6d^2$. If the trap density of states per unit area is N_{ts}, then there are $6d^2N_{ts}$ recombination center per grain, and there are $6d^2N_{ts}/d^3 = 6N_{ts}/d$ recombination center per unit volume. Therefore, $N_t = 6N_{ts}/d$.

the depth variation of grain boundary potential.

Computed values for GB potential, in dark and under illumination ($G=10^{20}\ cm^{-3}s^{-1}$) for both n- and p-type polysilicon, are presented in Fig.3.4 It can be seen that V_g increases with doping concentration N at low doping region and then decreases rapidly with further increase in N. The initial increase in V_g is due to the increasing Fermi-function with N. When f reaches its maximum value of unity, V_g is dominated by 1/N, thus V_g decreases rapidly with N in high doping region. The other feature of Fig.3.4 is that the light modulation effect on V_g is much more significant for a lowly doped sample than for a heavily doped sample. This is because the quasi-Fermi function in low doped region can be adjusted in a relative larger range than that in highly doped region. Fig.3.5 shows the effects of grain size d on V_g for different illumination level G. It can be seen that the larger d and higher G result in lower V_g. A strong illumination dependence of V_g is shown in Fig.3.6. It appears that V_g can be modulated significantly by photogeneration rate G.

As mentioned in chapter 2, photogeneration rate G is a strong function of depth from the semiconductor surface, under optical illumination. Under the AM1 condition, G changes more than three orders of magnitude from the surface to 100 μm depth. Thus the uniform photogeneration model may oversimplify the problem. For silicon, the data of G variation with depth, under solar illumination, can be found from refs.[16,17]. However these references give only numerical values. In our work, the Gauss-Quadrature approximation method was used to determine an analytical

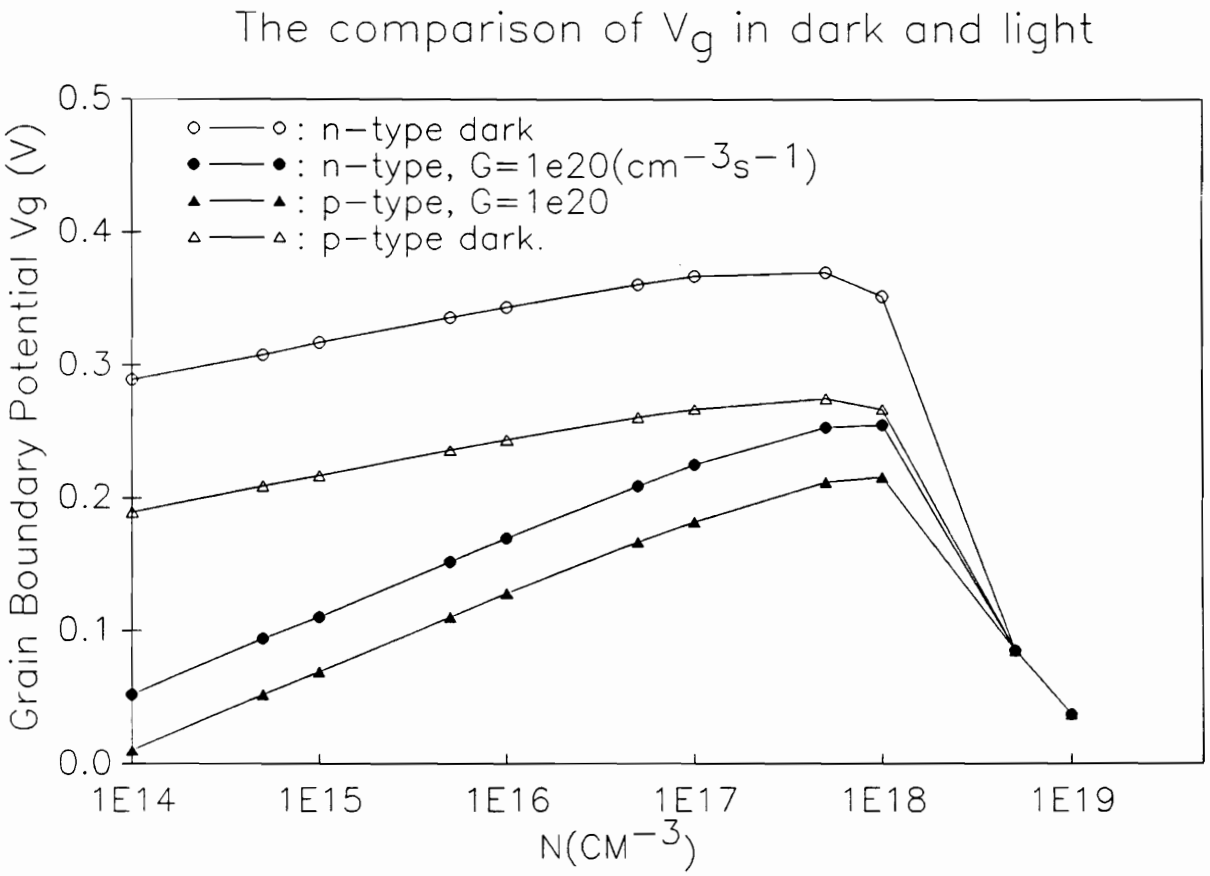

Fig.3.4 GB V_g as a function of doping concentration for both n and p type poly–Si at $N_{ts}=5x10^{12}(cm^{-2})$

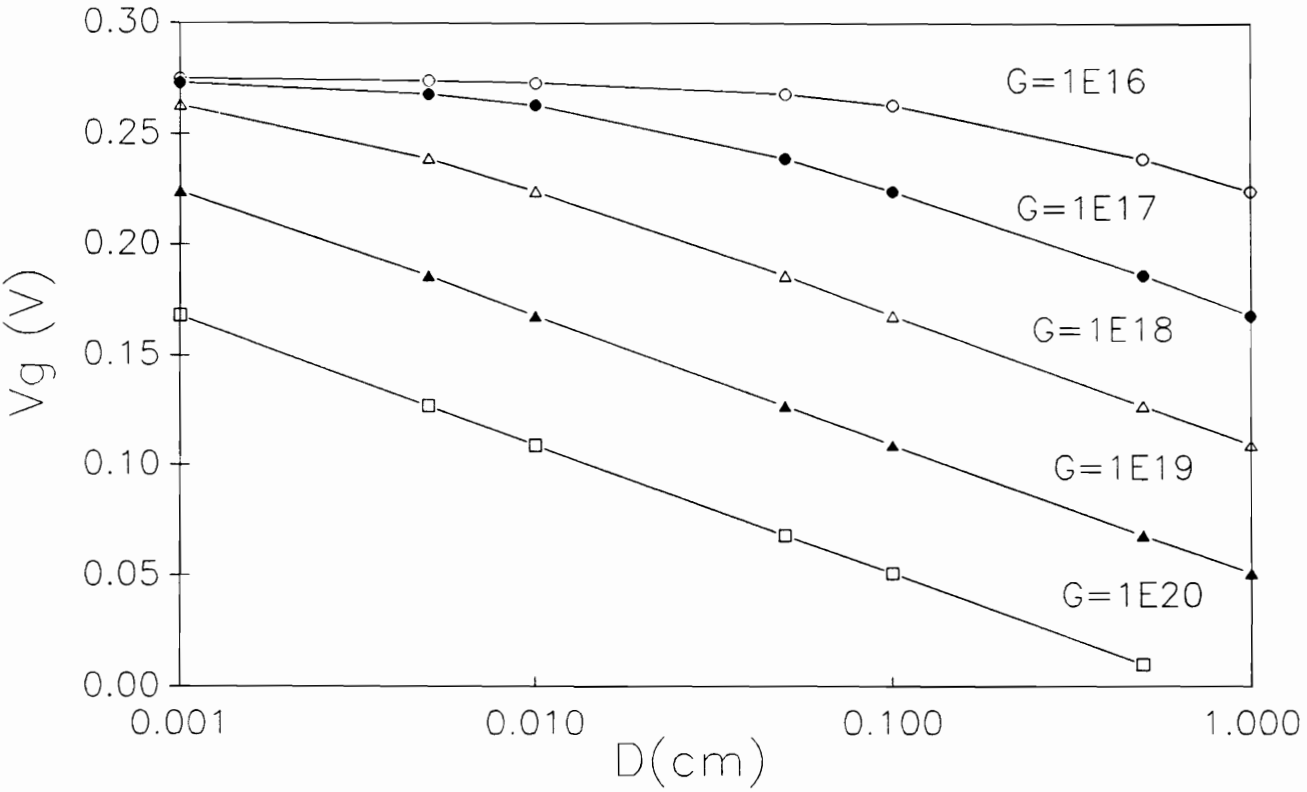

Fig.3.5 GB V_g as a function of grain size at N=1E16 and N_{ts}=5E12 for different generation rates G

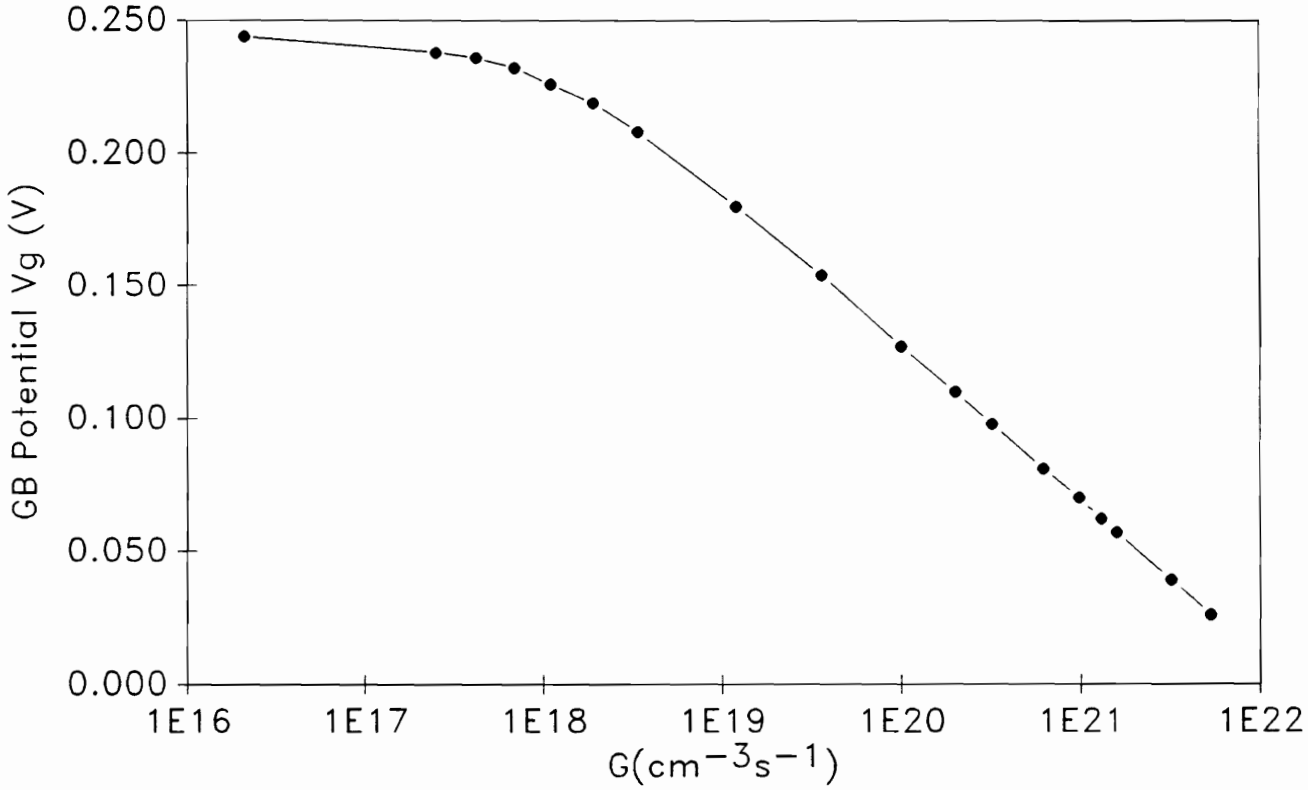

Fig.3.6 V_g as a function of generation rate for p-type poly-Si at Na=1E16(cm^{-3}), Nts=5E12(cm^{-2}) and d=0.5mm.

expression for G(x) [18]. By substituting this G(x) into Eq.(3.16), ß(x) can be determined, as can the depth variation of $V_g(x)$. Fig.3.7 demonstrates the depth variation of V_g in p-type material under three different solar illuminations and grain sizes. It shows that high level illumination can reduce the grain boundary barrier significantly and under same level illumination the smaller grain size results in larger V_g. Also, for large grain size (0.3 or 0.5mm) under 50 Sun illumination there is a flat band region where V_g equals zero (see (b) and (c) in Fig.3.6) and the larger the grain size, the longer is the flat band region. The flat band condition can be readily derived from Eq.(3.16) by setting $V_g=0$. This condition is characterized by the product of G and d, i.e.

$$(G\ d)_{flat} \geq 6\sigma_p V_{th} N_{ts} N \qquad (3.17)$$

as expected, high illumination, large grain size and low trap density facilitate the flat band condition.

It is shown from the above results that V_g is a strong function of depth. It is this variation of V_g that makes electrical parameters, such as τ, μ, and L, a function of depth in polysilicon.

3.5. Minority Carrier Transport Parameters

a). Minority carrier lifetime

Electron lifetime in p-type material is limited by grain boundary recombination and

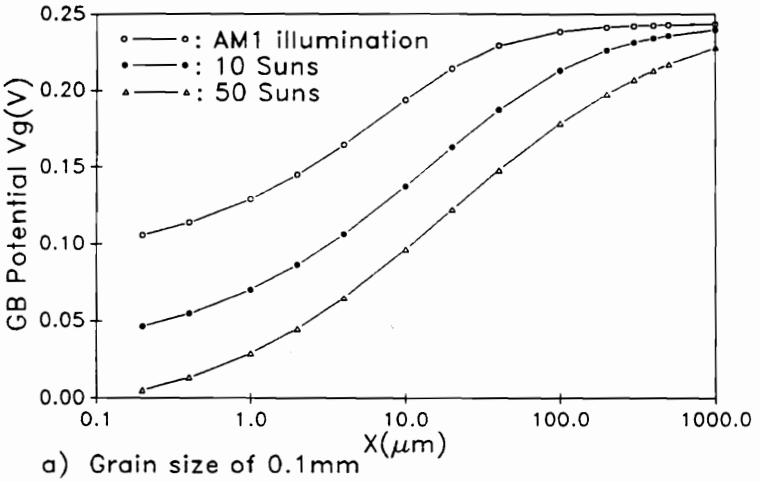

a) Grain size of 0.1mm

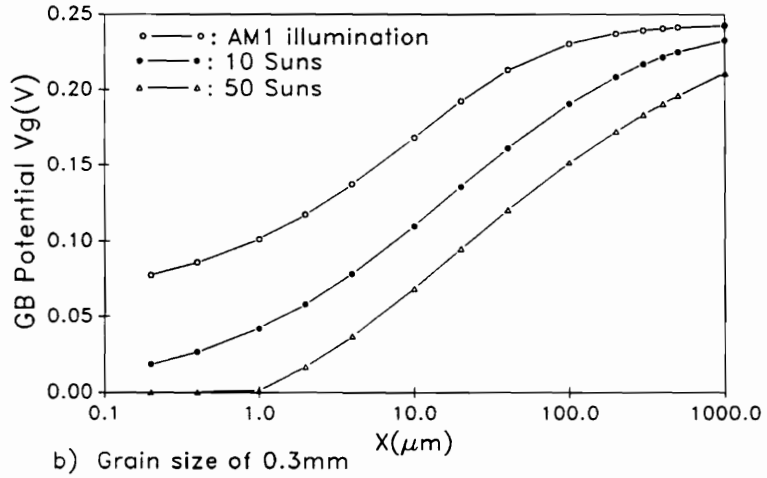

b) Grain size of 0.3mm

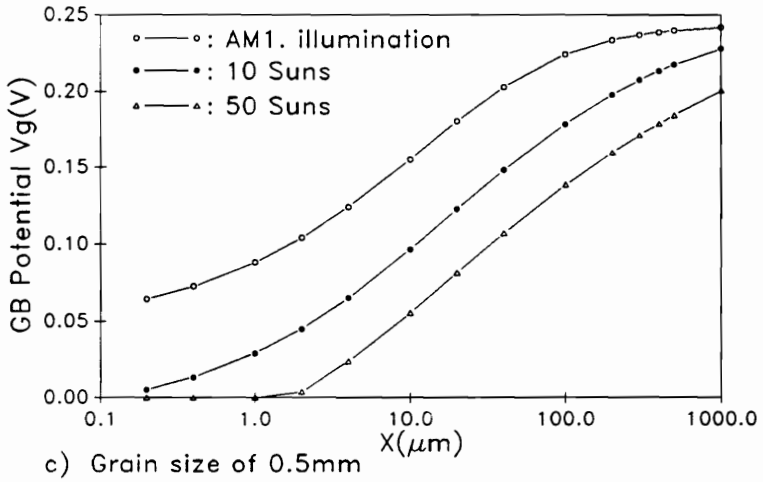

c) Grain size of 0.5mm

Fig.3.7 Depth variation of V_g for p-type poly-Si with N_{ts} of 5e12(cm^{-2}) for different illumination and grain size.

is given by

$$\tau_g = \frac{1}{\sigma_n V_{th} N_t} \tag{3.18}$$

where σ_n is the electron capture cross section, N_T is the effective grain boundary recombination center density per cm^3. For cubic geometry crystallites the conversion between N_T and N_s is expressed as

$$N_T = \frac{6\ N_s}{d} \tag{3.19}$$

where N_s is the effective recombination center density per cm^2 located at the edge of the GB space charge region. On the other hand, the effective GB surface recombination velocity, S_n, is defined as

$$S_n = \sigma_n V_{th} N_s \tag{3.20}$$

Therefore, τ_g can be expressed by

$$\tau_g = \frac{d}{6\ S_n} \tag{3.21}$$

In order to find the effective surface recombination velocity, we need to consider the recombination current at GB region which is expressed as [19]

$$J_r(0) = \frac{qV_{th}N_{ts}\sigma_n\sigma_p\ [p(0)n(0) - n_i^2]}{\sigma_n(n(0)+n_1) + \sigma_p(p(0)+p_1)} \tag{3.22}$$

where the zero point is chosen at the grain boundary center, p_1 and n_1 are expressed by Eq.(3.15), and σ_n and σ_p are the capture cross sections for electrons and holes. For polysilicon, the values of σ_n and σ_p were assumed to be 10^{-15} cm^{-2} and $2x10^{-16}$ cm^{-2} respectively [2,11].

For simplicity, Eq.(3.22) is evaluated for two cases:

(i). High level illumination: ($n(0) \approx p(0)$)

In p-type polysilicon, (E_i-E_t) is about 0.17eV; then $p_1 \approx 1x10^{13}cm^{-3}$, so that $n(0) \approx p(0) >> p_1 > n_1$ holds. Thus Eq.(3.22) becomes

$$J_r(0) = (1/6)[qV_{th}\sigma_n N_{ts} n(0)] \qquad (3.23)$$

(ii). Low level illumination: ($p(0) >> n(0)$ and $n(0)p(0) >> n_i^2$)

In this case, Eq.(3.22) simply becomes

$$J_r(0) = qV_{th}\sigma_n N_{ts} n(0) \qquad (3.24)$$

Thus, in general, we abtain

$$J_r(0) = \gamma qV_{th}\sigma_n N_{ts} n(0) \qquad (4.25)$$

where γ is a constant in the range of $1/6 \le \gamma \le 1$.

Considering that where are two space charge regions for each boundary and an effective recombination plane is located at the edge of depletion region, W, we have the following relation

$$J_r(0) = 2J_r(W) = 2qS_n(W)n(W) \qquad (3.26)$$

Rearranging Eq.(3.25) and (3.26) we obtain

$$S_n(W) = \frac{\gamma V_{th}\sigma_n N_{ts}}{2} e^{qV_g/kT} \qquad (3.27)$$

(In the above derivation n(0)=n(W)exp(qV$_g$/kT) has been used.) Substituting Eq.(3.27) into Eq.(3.21), an expression for the lifetime associated with GB recombination was derived as:

$$\tau_g = \frac{d}{3\gamma V_{th}\sigma_n N_{ts}} e^{-qV_g/kT} \qquad (3.28)$$

Eq.(3.28) shows the dependencies of τ_g on V_g, N_{ts} and temperature T.

The effective minority carrier lifetime τ_{eff} can be expressed as

$$\frac{1}{\tau_{eff}} = \frac{1}{\tau_g} + \frac{1}{\tau_s} \qquad (3.29)$$

where τ_s is the lifetime in single crystal material.

In most cases, τ_g is much smaller than τ_s, thus τ_{eff} is dominated by τ_g. Since V_g is a function of depth, the depth variation of the lifetime can be determined. This is presented in Fig.3.8. This shows that large grain size and high illumination intensity improve the lifetime significantly. A strong depth dependence of more than two orders of magnitude, from the surface to 100 μm depth, is also seen. From Fig. 3.8 (b) and (c), a constant τ is observed within a certain depth. This results from the flat band region of the grain boundary potential discussed in section 3.4.

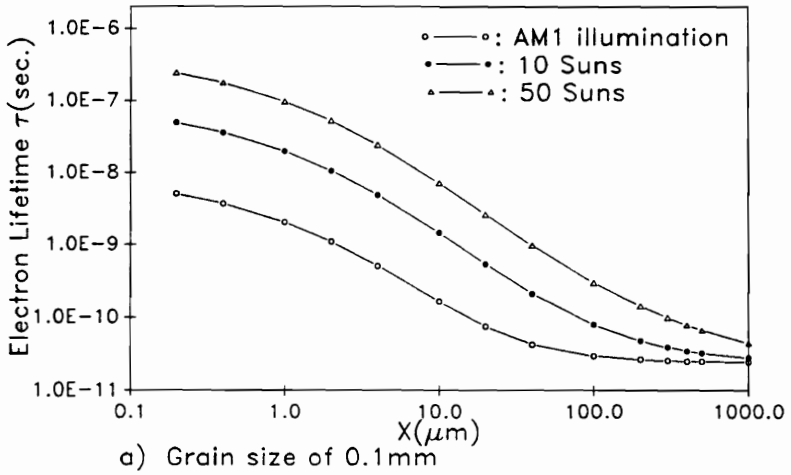

a) Grain size of 0.1mm

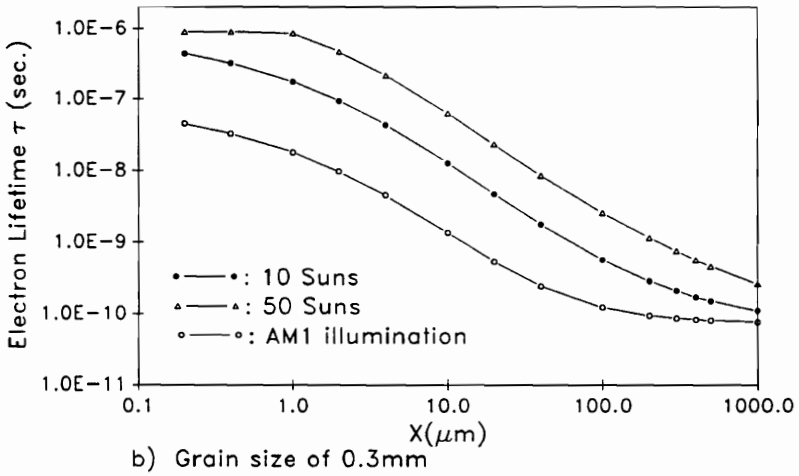

b) Grain size of 0.3mm

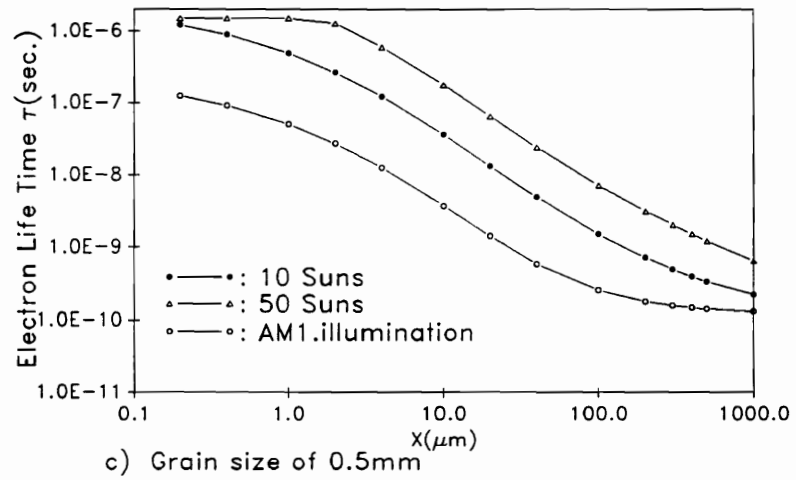

c) Grain size of 0.5mm

Fig.3.8 τ as afunction of x for p-type poly-Si with N_{ts} of $5e12(cm^{-2})$ for different illumination and grain size.

b). Minority carrier mobility μ and diffusion length L

Electron mobility and diffusion length in p-type polysilicon are discussed in this section. Several approaches were proposed to find μ in previous works. A model assuming that μ depends only on grain size was proposed in ref.[20]. A constant value of μ was used to calculate L in ref.[5,6]. Another assumption was made in which the mobility of minority carriers was considered to be the same as that of majority carriers [21].

It is difficult to calculate or measure mobility for the minority carriers directly. Such is not the case, however, for majority carriers. There is experimental evidence that the ratio of these two mobilities is almost a constant in both single crystal and poly-silicon [22]. Therefore, we propose a new way to estimate the minority carrier mobility, in which the ratio of the minority carrier mobility to that of the majority carrier is used. This experimental ratio is about 2.5 [22]. Both grain boundary and grain size effects are considered in our model.

For doped n- or p-type material, the measured mobility, μ_{eff}, is very close to majority carrier mobility, and μ_{eff} can be determined by voltage drop analysis. If a voltage V is applied to a sample of length ℓ, V_b is the voltage drop at each grain boundary, ρ_s is resistivity of grain region ($\rho_s = 1/(qN\mu_s)$, and μ_s is the mobility in the grain region, then V can be expressed as

$$V = (\ell/d) [V_b + J (\rho_s d)] \qquad (3.30)$$

where ℓ/d is the number of grains (for $\ell >> d$, the number of grain ~ the number

of boundary), J is the current density and (ρ_s d) is the resistance for each grain. V can also be expressed by an effective resistivity ρ_{eff}, such that

$$V = J \ell \rho_{eff} = J \ell /(q N \mu_{eff}) \qquad (3.31)$$

Combining Eqs.(3.30) and (3.31), one obtains

$$\mu_{eff} = \frac{1}{\frac{qNV_b}{Jd} + \frac{1}{\mu_s}} \qquad (3.32)$$

The current density J is given by [23,24]

$$J = A^* T^2 e^{(-qV_g+\delta)/kT} \left(\frac{qV_b}{kT}\right) \qquad (3.33)$$

where A^* is effective Richardson constant, and

δ = kT ln(N_c/N), for n-type

δ = kT ln(N_v/N), for p-type.

in which N_c is the effective density states at the bottom of the conduction band and N_v is the effective density states at the top of the valence band.

Substituting Eq.(3.33) into Eq.(3.32), one obtains

$$\mu_{eff} = \frac{1}{\frac{NkT}{A^* T^2 d} e^{(V_g+\delta)/kT} + \frac{1}{\mu_s}} \qquad (3.34)$$

and the minority carrier mobility μ can be determined from

$$\mu = r\,\mu_{eff} \tag{3.35}$$

where r = 2.5.

Applying Eqs.(3.28) and (3.35), the diffusion length L can be expressed as:

$$L = \left[\frac{kT}{q}\left(\frac{d}{3\gamma V_{th}\sigma_n N_{ts}} e^{-qV_g/kT}\right)\left(\frac{r}{\frac{NkT}{A^*T^2 d} e^{(V_g+\delta)/kT} + \frac{1}{\mu_s}}\right)\right]^{1/2} \tag{3.36}$$

The depth variation of μ and L under different illuminations and grain sizes is shown in Figs.3.9 and 3.10. Once again, high illumination and large grain size improve the parameters. From Fig.3.9, it can be seen that μ is less sensitive to the depth for the case of high illumination and large grain size than for of low illumination and small grain size. For 0.1mm grain size under the AM1 condition, μ changes by one order of magnitude from the surface to 100 μm depth, whereas it is almost a constant within the same depth for 0.5mm grain size and 50 Suns illumination. Two constant L regions are shown in Fig.3.10 (b) and (c), respectively. They are associated with the flat band regions. The difference in the two constant L values is caused by grain size effect only. From Figs.3.8 - 3.10, it is seen that the variations of the transport parameters with depth are significant and they are improved greatly by high level illumination and large grain size.

The trap density N_{ts} effect on the transport parameters is shown in Fig.3.11 It is seen (Fig.3.11 a) that τ decreases more than two orders of magnitude as N_{ts} increases from 10^{12} to 10^{13} cm^{-3}. It is interesting to note (Fig.3.11 b) that μ is almost

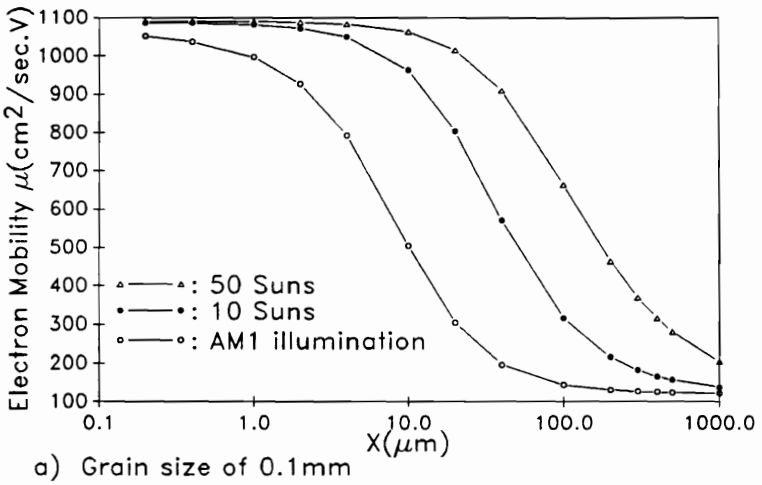

a) Grain size of 0.1mm

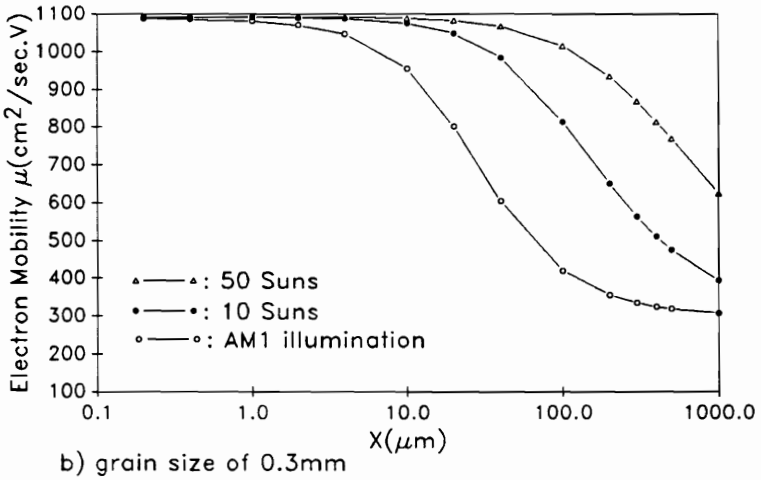

b) grain size of 0.3mm

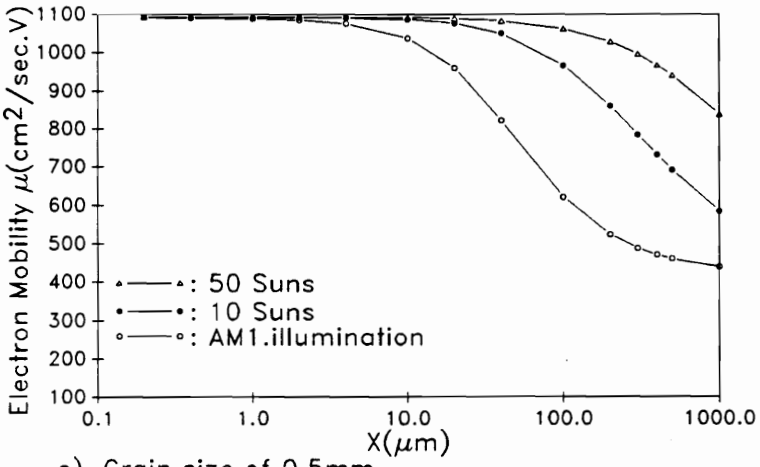

c) Grain size of 0.5mm

Fig.3.9 μ variation with depth x for p−type with N_{ts} of 5e12(cm^{-2}) for different illumination and grain size.

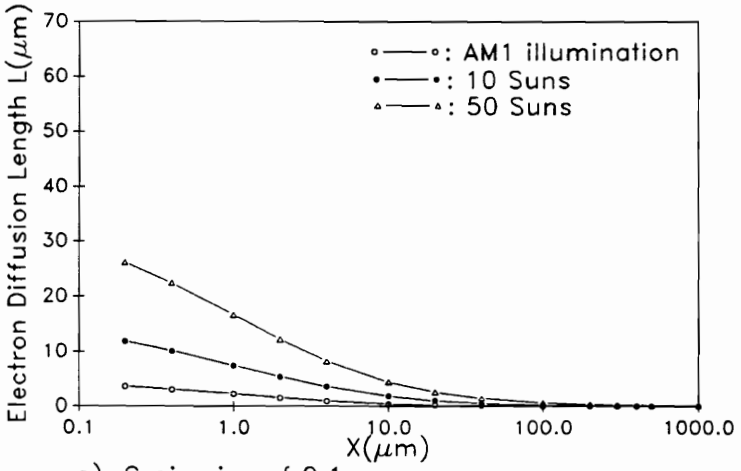

a) Grain size of 0.1mm

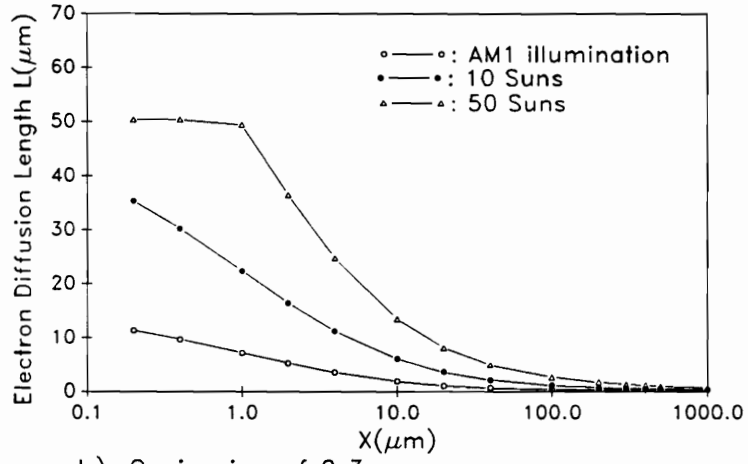

b) Grain size of 0.3mm

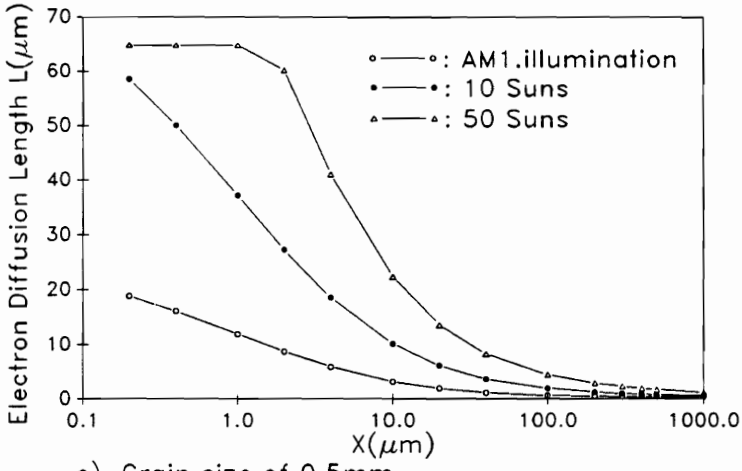

c) Grain size of 0.5mm

Fig.3.10 L variation with depth for p-type with N_{ts} of 5e12(cm^{-2}) for different illumination and grain size.

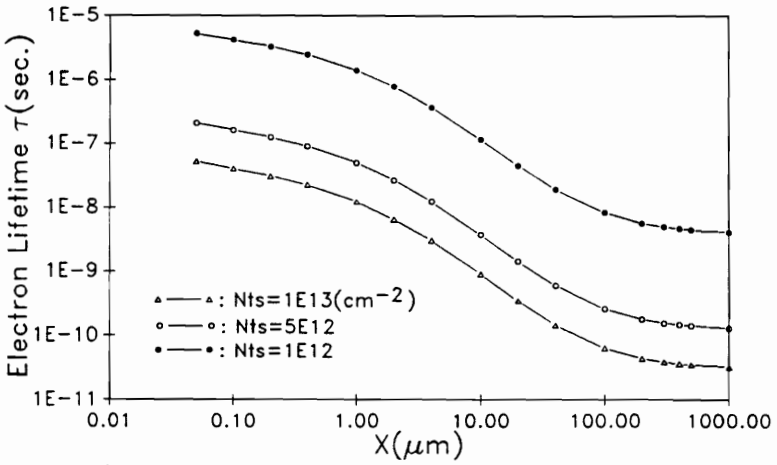

a) The lifetime τ

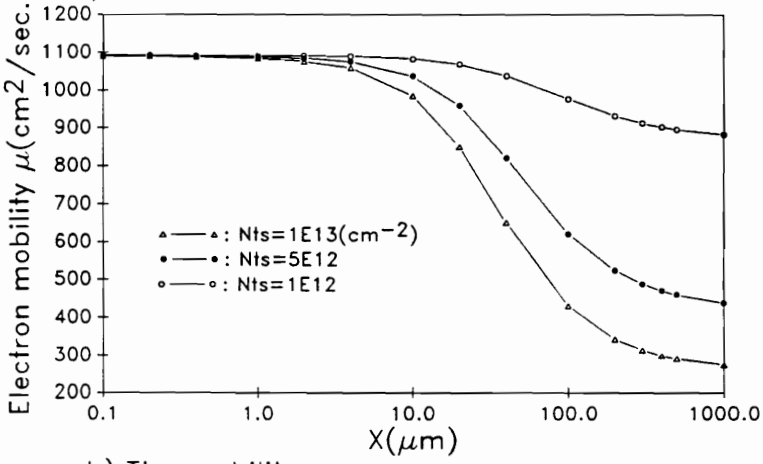

b) The mobility μ

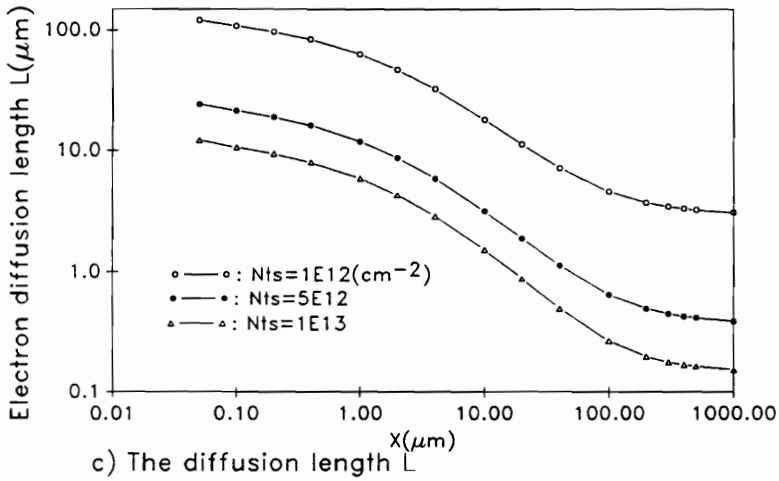

c) The diffusion length L

Fig.3.11 a) τ, b) μ, and c) L variations with depth x under AM1 illumination at grain size of 0.5mm, for different N_{ts}

constant in the region near the surface, ($x < 10\mu m$), and decreases with increase of x and N_{ts}. The results also suggest that N_{ts} has more effect on μ in the dark than in the light. L is also seen, from Fig.3.11 c, to decrease with increase of N_{ts}. These results suggest that N_{ts} is another important factor controlling the transport parameters.

3.6 Experimental results on trap density N_{ts}, electron capture cross section σ_n, and electron lifetime τ

a. Determination of N_{ts} and σ_n

N_{ts} can be obtained from Eq.(3.9) once the boundary barrier height is determined experimentally. Grain boundary capacitance measurements provide a widely used method to find the barrier height [2,11]. Based on a symmetrical Schottky barrier model [25], the capacitance of a grain boundary can be expressed as

$$C = \frac{q \epsilon A}{2 W} \qquad (3.37)$$

where ϵ is the dielectric constant, A is the area of a grain boundary and W is the width of grain boundary depletion region which was described by Eq.(3.3). By substituting Eq.(3.3) into Eq.(3.37) one obtains [25, 11]

$$C = A\left(\frac{q\epsilon N}{8 V_g}\right)^{1/2} \qquad (3.38)$$

Therefore by knowing doping concentration N, the barrier height V_g can be obtained from the capacitance measurements.

Two p-type boron doped samples with resistivity of 10 ±3 and 20 ±5 ohm-cm were used for our capacitance measurements. The samples were chemically polished in CP-4A solution (3ml HF; 5ml HNO_3; 3ml CH_3COOH) to eliminate saw damage from the surfaces. Aluminum was evaporated to form contacts near a grain boundary and the contacts were sintered at 450 °C for 10 min. in N_2 to form ohmic contacts. The sample configuration used in capacitance measurements is shown in Fig.3.12 (a). The capacitances were measured by a HP 4192A Impedance Analyzer at a frequency of 1MHz and zero DC bias condition [11]. The doping densities N of two samples were $1.16x10^{15}$ and $7.2x10^{14}$ cm^{-3} respectively, determined by the conventional $1/C^2$ vs. V method [26]. In order to obtain a reliable N_{ts} value, temperature dependence of grain boundary capacitance was measured in a temperature range of 200 K to 300 K. The measurement was done in an MMR cryogenic microminiaturized refrigerator (model K 2205). The system is cooled via high purity nitrogen gas under a pressure of 1800 psi through a fine capillary. The temperature control is achieved by a silicon diode and a resistor heater located at the sample mounting stage. The barrier height at each temperature was found from Eq.(3.38). The experiments showed an increase of the capacitance (or a decrease of the barrier height) with the increase of temperature (see Fig.3.13). Substituting expression 3.9 developed in section 3.3, into Eq.(3.38), N_{ts} can then be determined by non-linear least-square fitting. In the fitting

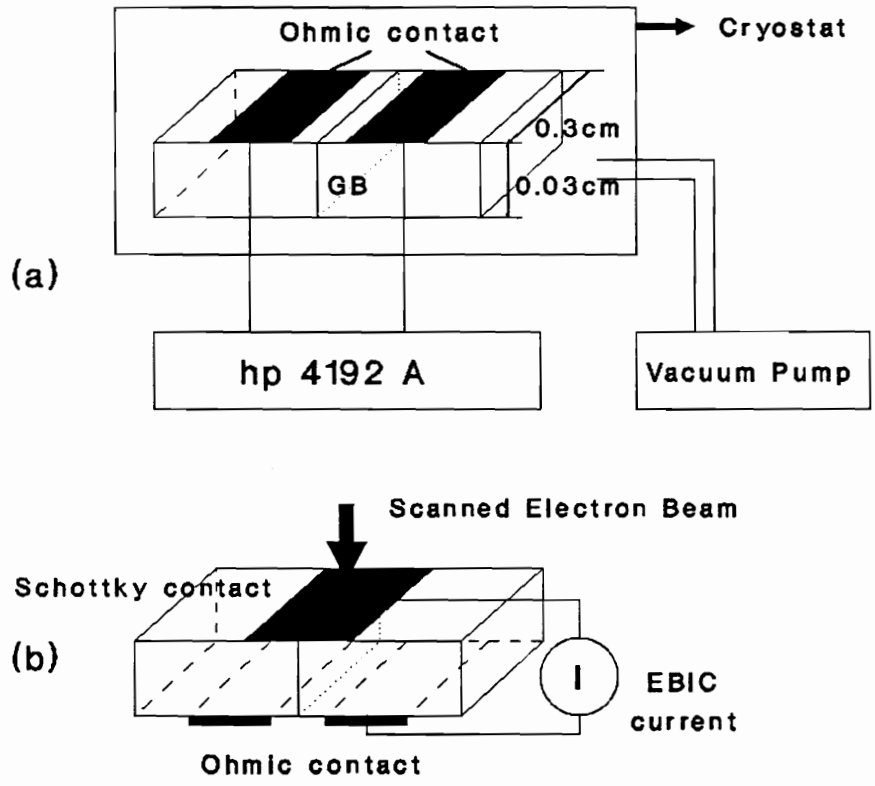

Fig.3.12 (a) Configuration for capacitance measurements:
(b) configuration for EBIC measurement

process, the temperature dependence of intrinsic carrier density n_i and energy band gap E_g were determined by [26]

$$n_i = BT^{3/2}e^{-\frac{E_g}{2kT}} \tag{3.39}$$

$$E_g = 1.17 - \frac{4.73x10^{-4}T^2}{T+636} \tag{3.40}$$

where B is a known temperature independent constant.

N_{ts} is the only one parameter to be determined in the least-square fitting. The experimental data and theoretical fitting are shown in Fig.3.13. The best fitting of N_{ts} for two samples is $7.02x10^{12}$ and $3.1x10^{12}$ cm^{-2} respectively. It is noted that the theoretical model fits the capacitance data quite well.

Once N_{ts} is obtained, the minority carrier capture cross-section σ_n can be deduced from the measurement of grain boundary surface recombination velocity according to Eq.(3.20). The surface recombination velocity S_n was measured by the electron beam induced current (EBIC) method. (The details of the method will be discussed in Chapter 5). EBIC was performed on the same samples as used in the capacitance measurements, except a Schottky barrier was formed on the other side of the sample, as shown in Fig.3.12 (b). The Schottky barrier acts as a collector of the electron beam generated current. The average values of S_n for the two samples were $8.77x10^4$ and $2.79x10^4$ cm^{-2} respectively, measured by EBIC. Substituting these two values along with the values of N_{ts} into Eq.(3.20), the electron capture cross-section σ_n for

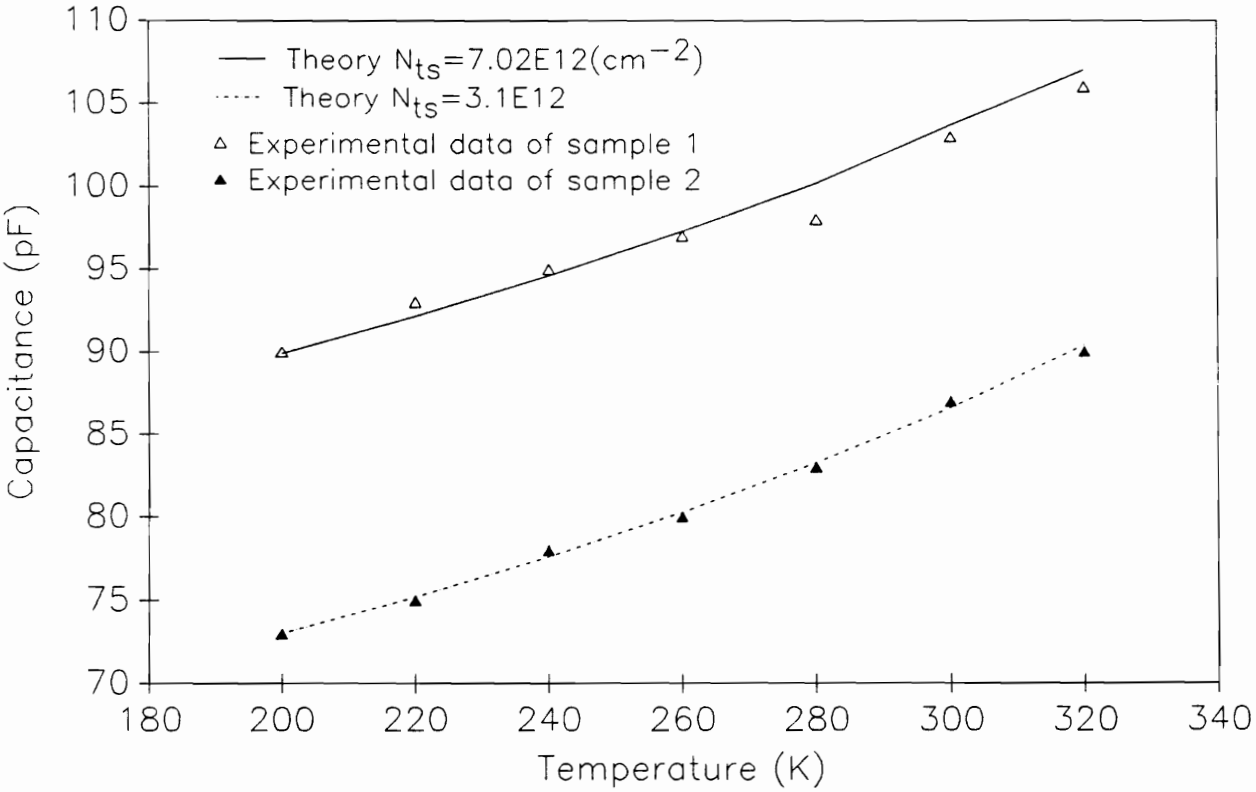

Fig.3.13 Grain boundary capacitance variation with temperature for two p−type samples with doping densities of 1.16E15 (▵) and 7.2E14(cm^{-3}) (▲).

the two samples were found to be 2.5×10^{-15} and 1.8×10^{-15} cm^2 respectively. These results are in the same order of magnitude ($1 \times 10^{-15} cm^2$ and $8 \times 10^{-15} cm^2$) as suggested in the literature [11,27].

b. Minority carrier lifetime measurements

The open circuit voltage decay (OCVD) method is often used to determine the minority carrier lifetime. The principal of the method is as follows [28]. When a forward bias voltage V is applied to an n/p junction, the excess electron density Δn near p side of the junction is given by the Boltzman relation

$$\Delta n = n_o(e^{\frac{qV}{kT}}-1) \qquad (3.41)$$

where n_o is the equilibrium electron density.

Eq.(3.41) can also be expressed as

$$V = \frac{kT}{q}\ln(1+\frac{\Delta n}{n_o}) \qquad (3.42)$$

If V_o is the junction voltage and Δn_o is the excess electron density after removal of the forward pulse, by using

$$\Delta n = \Delta n_o e^{-\frac{t}{\tau}} \qquad (3.43)$$

one obtains

$$V = \frac{kT}{q} \ln[1+(e^{\frac{qV_o}{kT}}-1)e^{\frac{-t}{\tau}}] \qquad (3.44)$$

Under conditions of $qV_o >> kT$ and $(qV_o/kT - t/\tau) >> 1$, Eq.(3.44) simplifies to

$$V = \frac{kT}{q}(\frac{q}{kT}V_o - \frac{t}{\tau}) \qquad (3.45)$$

and the lifetime can be expressed as

$$\tau = -\frac{kT}{q}(\frac{1}{dV/dt}) \qquad (3.46)$$

Therefore τ can be determined by measuring the slope of the voltage decay.

The samples used in our measurements were n^+/p junction solar cells. The circuit configuration used in OCVD measurements is shown in Fig.3.14. The minority carriers were injected into the base of the cell by a dc pulse applied in forward bias from a Tektronix TM503B PG508 50MHz pulse generator. A square pulse was used with amplitude of 6V, duration of 10μs, period of 100μs and delay time of 10ns. The voltage decay was recorded by a Tektronix Oscilloscope, model 2213A. Two typical open circuit decay curves are shown in Fig.3.15. The electron lifetime τ was determined by measuring the slope of the decay curve in linear region. It was noted in the measurements that one slope was found from the poly-Si cell, while two slopes were observed for the crystal Si cell. Such a two slope curve has also been observed by others [29]. They suggested that the first slope corresponded to a high injection

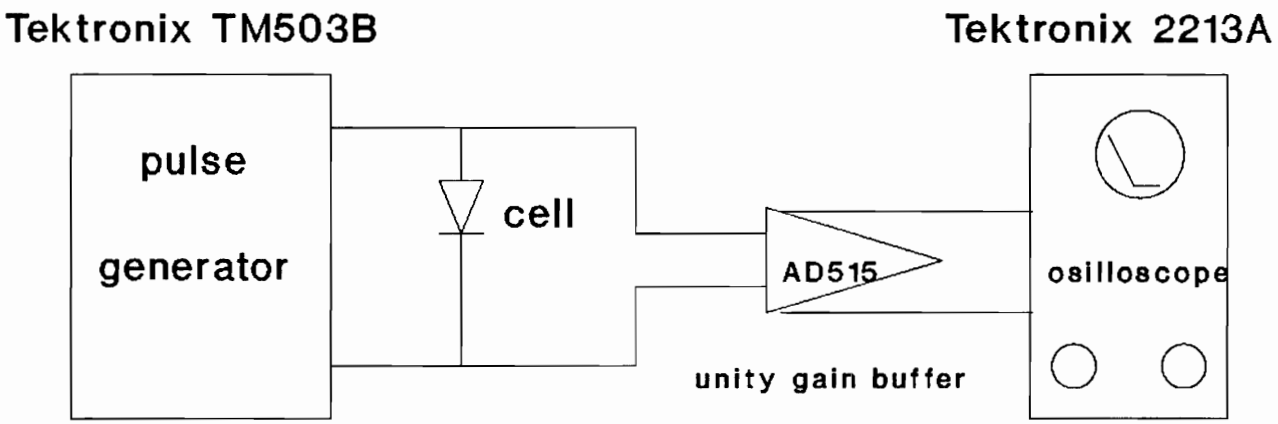

Fig.3.14 Schematic of open circuit voltage decay measurement

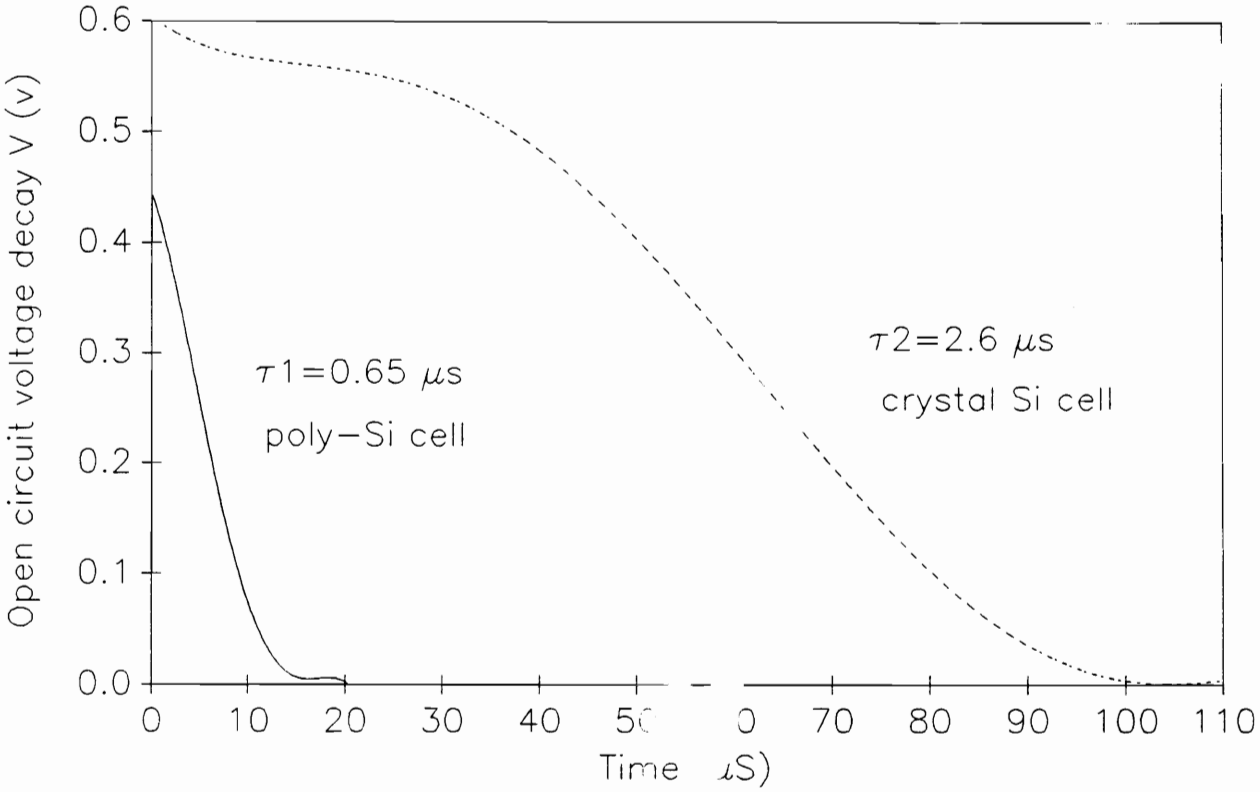

Fig.3.15 Open circuit voltage d cay measurements on poly−Si and crystalli e Si cell

condition lifetime and the second slope was a low injection condition lifetime. The $\tau 2$ shoen in Fig.3.15 was determined from the second slope.

In order to study the effects of illumination level on the minority carrier lifetime, the OCVD curves were measured under different light bias conditions. A tungsten light source was used and the light bias was controlled by adjusting the voltage applied to the tungsten light source. Higher voltage results in a higher illumination level. No calibration was made except for the voltage of 81V which gave an approximate AM1 illumination condition, calibrated by a standard cell. The voltage dependence of the electron lifetime in both poly and crystalline Si cells are shown in Fig.3.16. It can be seen that the lifetime in the poly cell increases with the voltage. The change in the crystalline cell, however, is not as significant as in the poly cell. A Similar result for the crystalline Si cell was reported by other authors [29]. In their experiments, the lifetime was measured at different distance between the sample and light source. No significant change of the lifetime was observed in their experiments. The illumination level dependence of the lifetime in poly cell can be explained by illumination effects on the grain boundary barrier height V_g, which has an exponential relationship with the lifetime. These experimental results qualitatively supported the analysis of illumination effects on the barrier height and lifetime developed in sections 3.4 and 3.5.

The effects of temperature on the lifetime of the poly cell were also investigated in a range of 200 to 550K. For T lower than 350K, the measurement

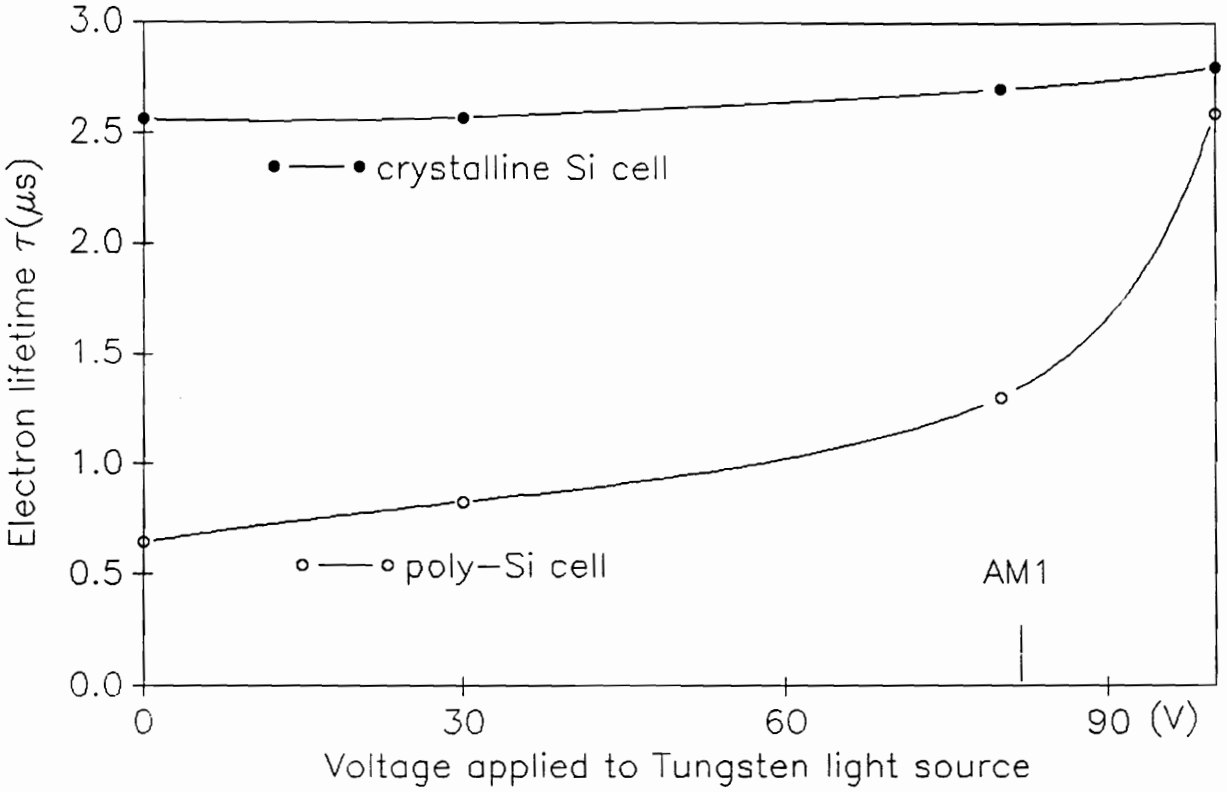

Fig.3.16 Electron lifetime variation with illumination level for crystalline and poly–Si cells, (the voltage corresponding to AM! is indicated)

was done in the MMR refrigerator (model K 2205). For T higher than 350K, the sample was measured in a temperature controlled oven, in a N_2 atmosphere.

The temperature dependence of the lifetime is shown in Fig.3.17. An increase in lifetime with temperature was found in the low temperature region (T < 400 K). The lifetime tends to saturate in the high temperature region (T > 450 K). The temperature dependence of τ can be interpreted by the relations developed in the previous section. From Eq.(3.28), the lifetime can be expressed as

$$\tau = \tau_{max} e^{-\frac{qV_g}{kT}} \qquad (3.47)$$

where τ_{max} is a temperature independent constant, and the maximum value of τ for a given sample. From the temperature dependence of grain boundary capacitance measurements, V_g decreasing with increase of temperature has been observed. Thus in the low temperature region the rapid increase of τ with temperature results from the decreasing V_g. At high temperatures, $qV_g/kT \leq 1$, and Eq.(3.47) can be simplified to

$$\tau = \tau_{max}(1-\frac{qV_g}{kT}) \qquad (3.48)$$

So a saturation behavior at high temperature is expected.

The data in Fig.3.17 were fitted by combining Eq.(3.9) and Eq.(3.47). Two parameters τ_{max} and N_{ts} were determined by fitting based on the least-square method. A doping density N of 5.1×10^{16} cm^{-3} was determined by the $1/C^2$ vs.V

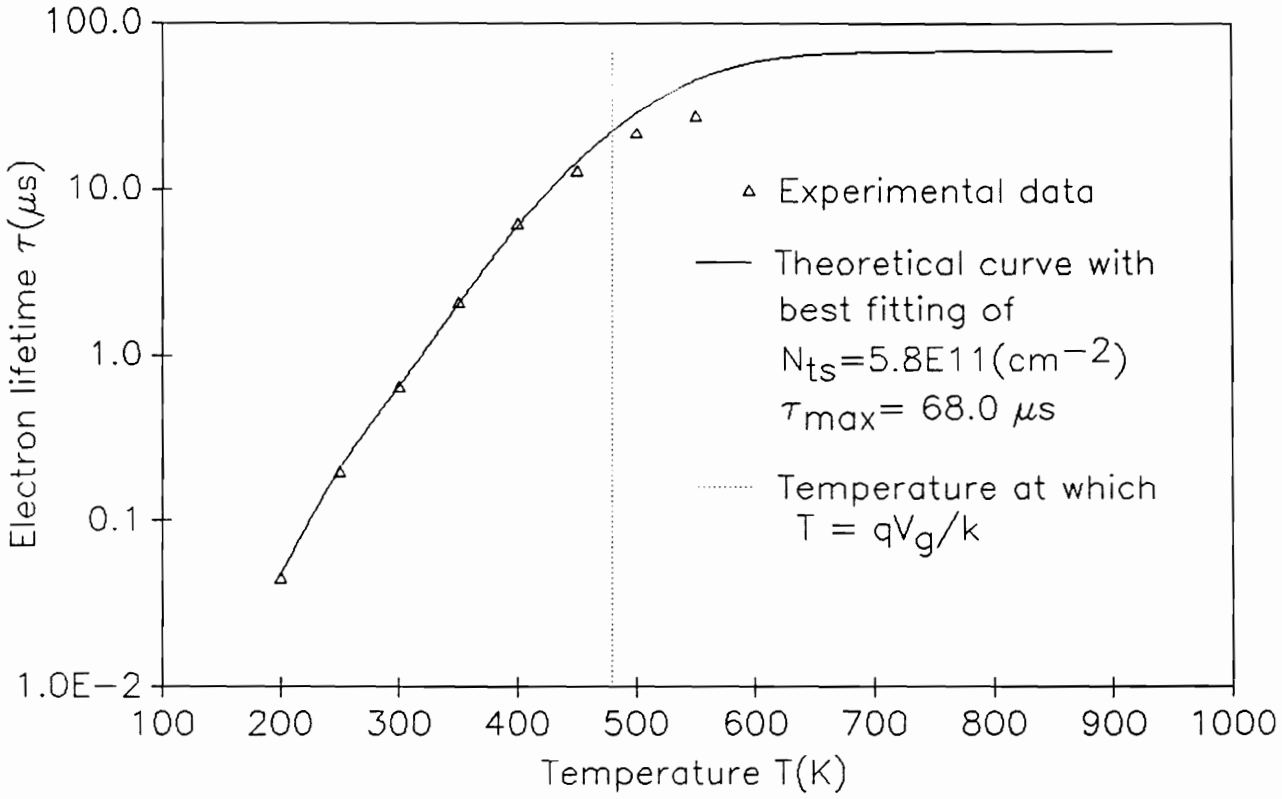

Fig.3.17 Temperature dependence of electron lifetime measured by open circuit decay method

measurements. Eqs.(3.39) and (3.40) were applied in the fitting process for the temperature dependence of n_i and E_g. The theoretical result in the range of 200 K to 1000 K was also plotted in Fig.3.17. The best fitting gave the value of N_{ts} of 5.8×10^{11} cm^{-2} and τ_{max} of 68.0 μs. A similar τ_{max} of 60.1 μs was reported by others [30]. It can be seen from Fig.3.17 that our grain boundary recombination model fits the experimental data very well in the low temperature region but deviates somewhat in high temperature region. This is because, in the above analysis, only grain boundary recombination was considered. It is true that at temperatures below 400 K, V_g is much higher than kT, thus the effective lifetime is dominated by grain boundary recombination. As T increases, however, the barrier height decreases and the grain boundary recombination is reduced. Meanwhile, phonon scattering becomes a dominant recombination mechanism. Therefore a model combining grain boundary recombination and phonon scattering is needed to explain the high temperature data. This was not undertaken in this thesis.

3.7 Conclusions

New relations for the grain boundary (GB) potential barrier height (V_g) for both the dark and light cases were developed. The barrier height as a function of doping density, grain size, photogeneration rate and depth from the surface, under solar illumination was studied theoretically. The dependences of electron lifetime (τ), mobility (μ) and diffusion length (L) on the GB V_g, the depth, the illumination levels,

trap density, and grain size were discussed. It was shown that V_g increases whereas τ, μ, and L all decrease drastically with increasing depth, under solar illumination. The results also showed that under high level illumination, V_g is reduced, the minority transport parameters improved significantly, and a flat band region in which V_g equals zero could appear at certain conditions. These results suggest that using polysilicon solar cells under concentrated illumination would significantly improve their performance. From the temperature dependence of the grain boundary capacitance and lifetime measurements, the decrease of V_g with increase of temperature was observed experimentally. A method to determine trap density was developed, based on temperature dependence of the capacitance. The grain boundary model closely follows the capacitance and lifetime measurements.

References

[1] H.C.Card and E.S.Yang, IEEE.Trans.Electron Devices ED-24,397, (1977)

[2] C.H.Seager, J.Appl.Phys. 52(6),3960 (1981)

[3] J.G.Fossum, IEEE.Trans.Electron Devices ED-27 692 (1980);ED-29, 1185 (1982)

[4] D.P.Joshi, Solid-State Electron. 29, 19 (1986)

[5] D.P.Joshi and R.S.Srivastava, J.Appl.Phys. 59(8),2549 (1986)

[6] D.P.Joshi and R.S.Srivastava, Phys.State,Sol.(a) 84,311, (1984)

[7] C.A.Dimitriadis,A.Alexandrou and N.A.Economou, J.Appl.Phy.60, 3651 (1986)

[8] P.Rai-Choudbury and P.L.Hower, J.Electron Soc.120,1761 (1973)

[9] T.I.Kamins, J.Appl.Phys.42,4357 (1971)

[10] J.Y.W.Seto, J.Appl.Phys.46,5247 (1975)

[11] C.H.Seager and T.G.Castner, J.Appl.Phys.49,3879 (1978)

[12] G.Baccarani,B.Ricco and G.Spadini, J.Appl.Phys.49,5565, (1980)

[13] J.Martinez and J.Piqueras, Solid-State Electron.23,297 (1980)

[14] N.C.C.Lu,L.Gerzberg,C.Y.Lu and J.D.Meindl, IEEE Trans. Electron Devices,ED-28, 818(1981)

[15] S.Noor and C.E.Rogers, Solid-State Electron,31,1157 (1988)

[16] J.G.Fossum, Solid-State Electron, 19, 269,(1976)

[17] H.C.Heieh, C.Hu and C.I.Drowley, IEEE Trans,Electron Devices,ED-27,883 (1980)

[18] Chapter 2 section 2.2 of this dissertation

[19] M.Sze, Physics of Semiconductor Devices, p48, New York,Wiley(1969)

[20] A.K.Ghosh, C.Fishman and T.Feng, J.Appl.Phys.51,446,(1980)

[21] K.Sen, J.Electronics,54,341 (1983)

[22] G.Mathian,H.Amzil,M.Zehhaf,J.P.Crest,E.Psaila and S.Martinuzzi, Solid-State Electron, 21,1045 (1978)

[23] G.J.Korsh and R.S.Muller, Solid-State Electron. 21, 1045, (1978)

[24] M.L.Tarng, J.Appl.Phys.,49, p4049, (1978)

[25] W.E.Taylor, N.H.Odell and H.Y.Fan, Phys. Rev. 88, 867 (1952)

[26] S.M.Sze, Semiconductor Devices John Wiley & Sons, 1985

[27] D.P.Joshi and D.P.Bhatt, IEEE Tran. Electron Devices, 37, 237, (1990)

[28] A.G.Millens, Semiconductor Devices and Integrated Electronics, Van Nostrand Reinhold Company, (1980)

[29] J.E.Mahan and R.I.Frank, IEEE Tran. Electron Devices, 26, 733, (1979)

[30] P.C.Mathur,P.R.Sharma, P.Saxena and L.D.Arora, J.Appl.Phys., 52, 3651, (1981)

Chapter 4

Hydrogen Ion Implantation in Poly Silicon Solar Cells

4.1 Introduction

a. Background

Recent investigations have shown that the use of hydrogen ion implantation to passivate grain boundary defects and defects inside the grain is an effective way to improve the electrical quality of cast and ribbon polycrystalline silicon [1,2]. Backside hydrogenation of poly-Si solar cells has been reported with some success recently [3,4]. But a systematic study of the implantation conditions, such as H^+ ion beam energy, beam current, temperature and implantation duration has not been reported. The work reported in this chapter, efforts wre made to find optimum implantation conditions in terms of solar cell efficiency improvements. FTIR (Fourier Transform Infrared) study and the TEM (Transmission Electron Microscopy) study on hydrogen implanted samples are also discussed.

b. Why hydrogen ?

Incorporation of atomic hydrogen into amorphous, polycrystalline and crystalline silicon causes significant changes in both electrical and optical properties [5]. The principal interest in hydrogen treatment of semiconductors arises from its ability to passivate electrical defects such as dangling bonds, dislocations and impurity complex defects. The work of Spear and his collaborators [6] has shown that a-Si (amorphous

Si) prepared by low temperature glow discharge in silane is " dopable " over many orders of magnitude of resistivity in almost the same fashion as crystalline silicon. On the other hand, investigations of a-Si prepared by sputtering or vacuum evaporation have indicated that the conductance of these samples was insensitive to the addition of impurities from groups III and IV of the periodic table. These conflicting results have been clarified by studies which showed that Spear's sample appeared to contain large amount of hydrogen [7]. Others investigators have shown that at least part of the role that hydrogen plays is to reduce the trap density making the Fermi level unpin and thereby permitting conventional doping methods to succeed. These traps were thought to arise from the dangling bonds resulting from frozen-in atomic configurations [8].

The same unfavorable configurations exist in polycrystalline silicon. Hydrogen thus appear to be a prime candidate for passivating the electrical trap states. The fact that hydrogen has high mobility in many solids has suggested that diffusing hydrogen into poly-Si material is feasible. It is now well established that such hydrogenation can reduce the minority carrier recombination center density at grain boundaries and dislocations [9,10].

c. Why H^+ ion implantation ?

Two most common and controlled hydrogen incorporation methods used today are H_2 plasma and implantation of low energy H^+ ions from a broad beam source.

The plasma is usually excited by an RF glow discharges method [11]. Samples

are heated typically to 100 to 350 °C in plasma for a period of several hours. The advantages of this method are that it is simple and cheap compared to ion implantation. The disadvantage is that the dose rate is not well controlled because the mechanism of hydrogen incorporation from a plasma source is still not well understood [9]. Another major disadvantage is the long duration required, typically a few hours, or even more than ten hours, since the whole process is limited by the surface absorption of hydrogen.

The alternative method is to implant hydrogen ions generated by the Kaufman ion source system at low energy and high current density. Typically the ion energy can be adjusted in the range of 0.4 - 2 KeV, the current in the range of 0.2 - 1.5 mA/cm^2, and the temperature in the range of 200 - 350 °C. The details of Kaufman ion source will be discussed in the next section. The advantages of H^+ ion implantation are close control of the H^+ energy, dose rate, and short duration, generally less than twenty minuets. The short duration is possible because a higher hydrogen concentration layer (higher than the surface absorption limits) is formed at the surface, which acts as an internal diffusion source of H species. Therefore the surface absorption limitation is not a problem in hydrogen implantation. However, there is a major disadvantage for the implantation, that is, the extensive damage layer is created at the surface by high hydrogen flux. In order to reduce the influence of the surface damage on solar cell performance, backside hydrogen ion implantation method was proposed [3,4].

d. Restrictions of frontside hydrogenation

Implantation of hydrogen from the junction side or frontside of a solar cell can passivate defects near the junction easily. The frontside implantation, however, damages the surface near the junction and thus limits the performance of the solar cell [12]. Also, frontside hydrogenation places a lot of restrictions on solar cell fabrication processes [13]. It requires that all the cell processes involving temperature in excess of 300 °C be carried out before hydrogen implantation, because heating at temperature above 300 °C results in release of hydrogen from the sample, as we will see in an annealing experiment in the next chapter. Consequently, hydrogen must be introduced after front and back metallization. It must also be introduced prior to deposition of antireflection coating (AR coating), since hydrogen cannot easily pass through the AR coating. Thus, AR coating after the implantation has to be done by low temperature processes such as a spraying method, which lack uniformity control on large areas and do not produce high quality AR coatings [13]. Also, fill factor (FF) decreases in frontside implanted solar cells because of the H^+ bombardment and the interactions between hydrogen and front metallization [14]. Another drawback of the front side implantation is that it introduces undesirable impurity contaminations near the junction region, which is crucial for solar cells. Impurities such as tungsten, molybdenum, chromium and copper have been detected at the implanted surface [15]. The impurities can come from the filament, extraction grids and target of the sample holder. These contaminations together with a heavily

damaged front surface will result in a high recombination velocity at the front surface.

Back side hydrogenation can eliminate many of these problems. Hydrogen can be implanted either before the backside metallization or after all the cell processes are finished by using a gridded back contact. In the former case, the back metallization serves as a blocking layer to the hydrogen and forces hydrogen to diffuse into the bulk during the metal sinttering [13]. It should be mentioned that the backside hydrogen implantation also causes surface damage and impurity contaminations. But the back surface is far from the junction region, and the effects of the damage on solar cell performance are far less significant than that in front side implantation.

4.2 Ion implantation system, ranges of implantation parameters and samples

a. Kaufman ion beam system

Hydrogen ion implantation experiments were carried out in a Commonwealth Scientific Corporation's Mollatron model IV Kaufman ion beam system, equipped with a blazers TSH 511 trobomolecular pump and a mechanical pump connected in series (see Fig.4.1). The base vacuum pressure for the system is about 2 - 4 $x10^{-6}$ Torr. The hydrogen implantation was done by backfilling with highly pure hydrogen gas (99.999 %) to a pressure of about 3 - 4 $x10^{-4}$ Torr by a automatic gas pressure regulation control. The 4 inch diameter Kaufman ion source is equipped with a aligned molybdenum grid and is capable of producing an ion beam energy in the

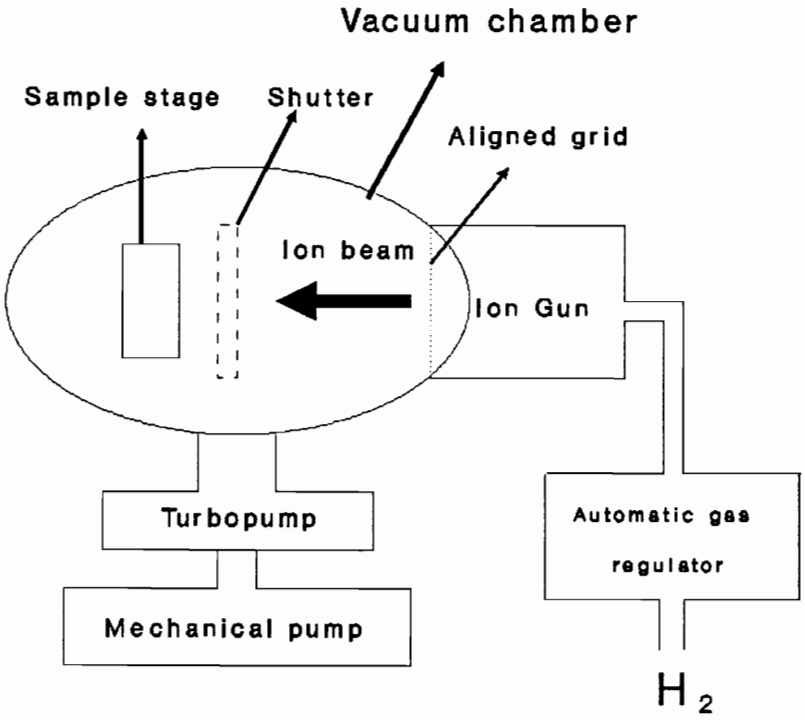

Fig.4.1 Schematic of the Kaufman ion beam system

range of 0.4 - 2 keV ±10 eV and beam current up to 150 mA ±5mA. The 3 inch diameter, rotating, water cooled sample stage is quipped with a heater which is capable of heating samples to 450°C ±5°C. Samples were held with sample surface perpendicular to the ion beam.

A hot filament is used as a electron source to ionize a source gas, such as H_2 or Ar. The positive ions are accelerated out of the gun by applying a positive voltage with respect to the grounded sample stage. To assist the ionization process, a weak magnetic field with longitudinal flux lines is used. The magnetic field makes the electrons travel in a spiral path from the hot filament toward the anode. It lengthens the electron's path and thus increases the probability of colliding with the source gas atoms. The sample holder is attached to a stem driven by a chain. The resulting rotatory motion improves implantation uniformity from sample to sample. The holder is equipped with both a heater and circulating water cooler. Since the ion beam is not stable for the first several minutes after turning on the ion gun, a shutter is used to cover the samples. The shutter provides a steady state condition for implantation, and makes the experiement more controllable and reproducible. The sample stage can be tilted with respect to the beam direction by an external manual control.

b. Ranges of the implantation parameters

A systematic study on implantation parameters was carried out in the following ranges:

Ion energy: 500 - 2000 eV

Beam current: 10 - 80 mA

Temperature: 150 - 400 °C.

c. Samples

Samples used in the experiments to optimiz implantation conditions were poly-Si n^+-p junction solar cells supplied by Solarex. The junctions were formed by conventional thermal diffusion processes. The junction depth was about 0.3 - 0.5 m. Small 2x1 cm^2 solar cells were cut from 4.5 x 4.5 in^2 wafer by laser or by diamond saw. I-V characteristics did not change after cuting by the diamond saw, but did change after beingcut by the laser. Shorted p-n junctions or large leakage currents were observed after laser cuts due to p-n junction melting at the edge during the laser process. The shorts and leaky p-n junctions were eliminated by edge polishing with sand paper.

Polycrystalline silicon materials used in the FTIR and TEM experiments were Wacker cast and ribbon samples. The materials were p-type boron doped with resistivity in the range of 0.5 - 1.5 ohm-cm.

4.3 Optimum implantation parameters

Four variables were chosen in the following hydrogen implantation experiments. They were ion beam energy, E, ion beam current, I_b, sample holder temperature, T,

and implantation duration, t. A systematic experiment with these four parameters was carried out and the optimum condition was determined based on improvements of solar cell parameters such as open circuit voltage, V_{oc}, short circuit current, J_{sc} and cell efficiency, EFF. More than 60 small (2x1 cm^2) poly-Si cells without antireflective coatings have been measured under the AM1 condition before and after hydrogen implantation. The cells were selected to have close initial V_{oc}, J_{sc}, and EFF so that the changes after hydrogen treatment were comparable. The initial values were selected as: V_{oc}=530 ±5mV, J_{sc}=19 ±0.5mA and EFF=7 ±0.5%.

a. Beam energy E

Ion beam energy varied from 0.5 to 2 keV, (2 keV is the upper limit for the ion gun), in a increment of 0.5 keV. Beam current of 50 mA and 10 minutes implantation duration were kept unchanged Fig.4.2 (a) and (b) show the improvements of V_{oc} and J_{sc} as a function of the beam energy. Each data point was an average value on three cells. It can be seen that both V_{oc} and J_{sc} increase with E and level off around 1.5 keV. In the range of 1.5 to 2 keV the plot is basically a flat line. So E=1.5 keV was determined as the optimum beam energy.

b. Beam current, I_b

Experiments on ion beam current were performed in a range of 10 to 80 mA, which corresponds to beam flux of 0.1 to 1mA/cm^2. The beam energy was set at 1.5 keV based on the result of Fig.4.2. The improvements of V_{oc} and J_{sc} as a function of I_b at two temperatures (150 and 250 °C) are shown in Fig.4.3 (a) and (b),

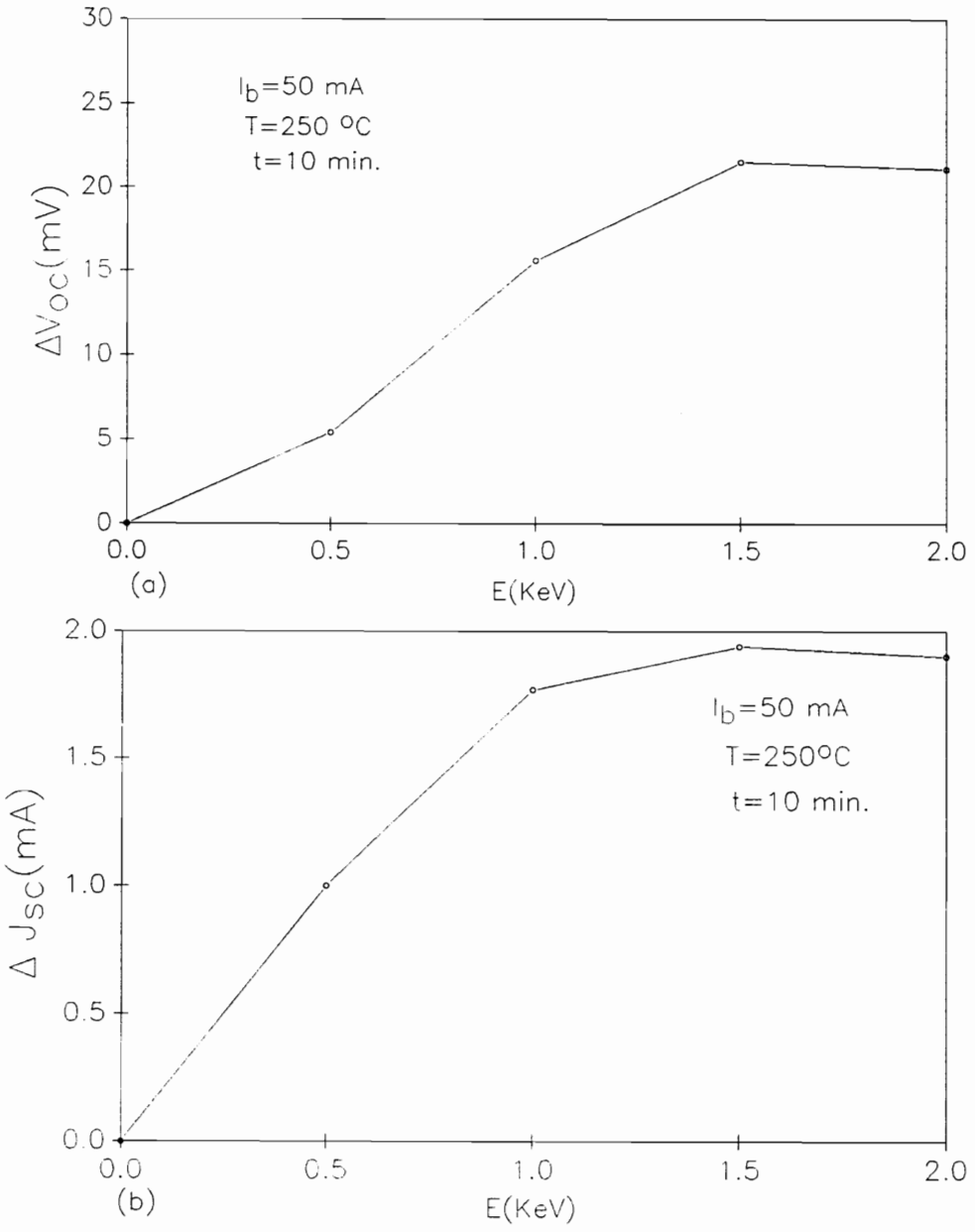

Fig.4.2 Hydrogen ion beam energy effect on V_{oc} (a) and on J_{sc} (b)

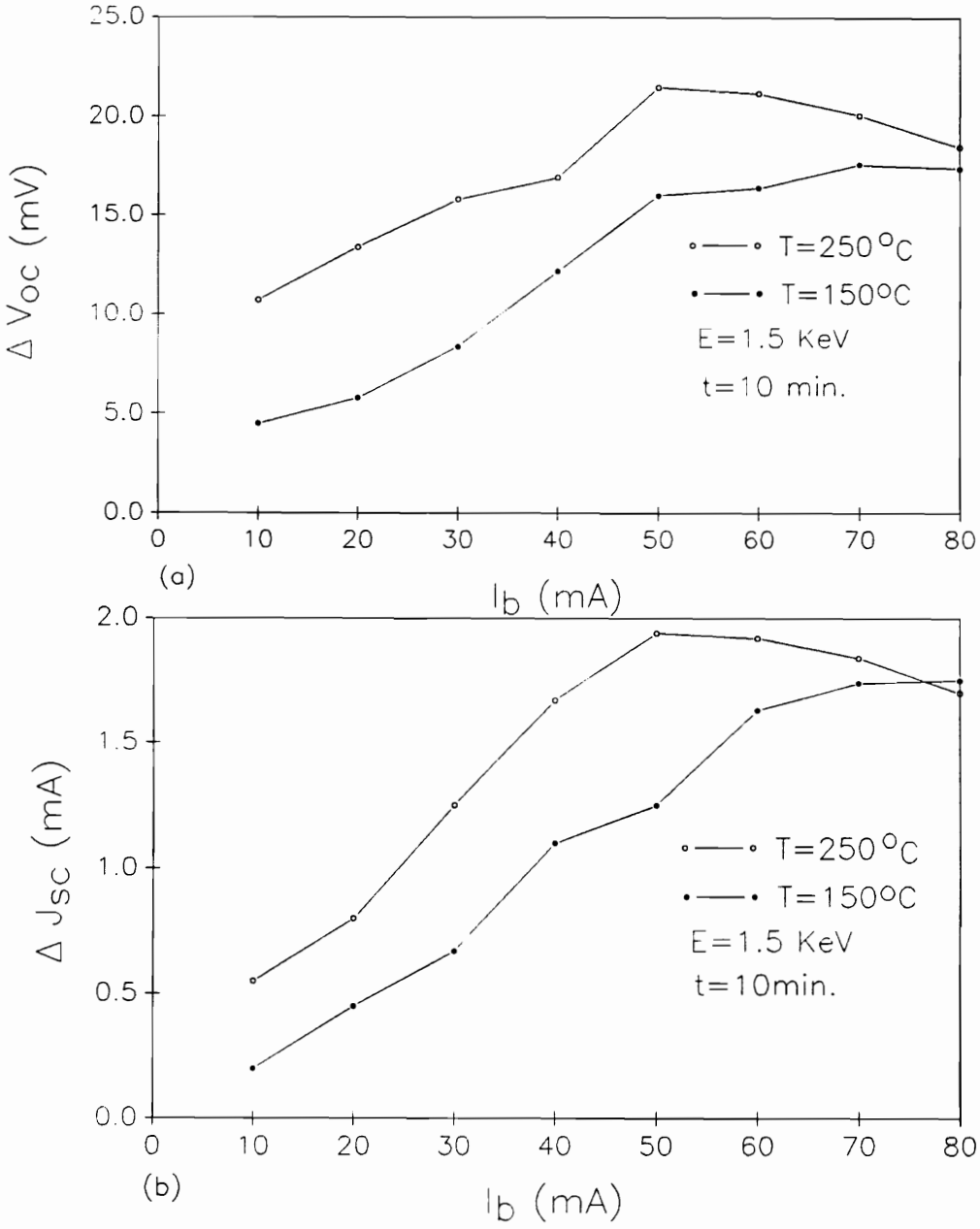

Fig. 4.3 Ion beam current effect on V_{oc} (a) and on J_{sc} (b)

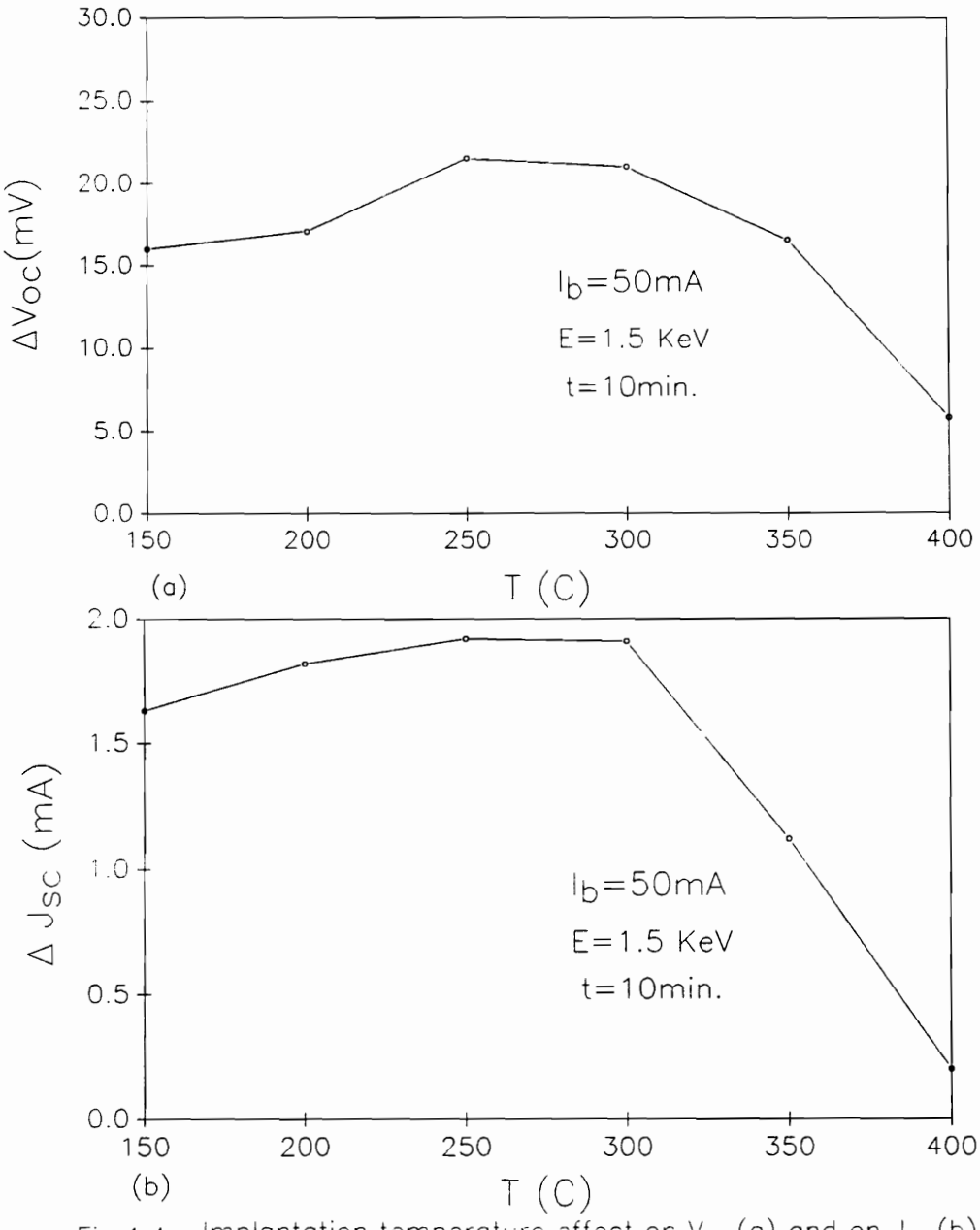

Fig.4.4 Implantation temperature effect on V_{oc}(a) and on J_{sc}(b)

respectively. It can be seen that the improvements were greater at 250 °C than at 150 °C, except at high beam current region (>70mA). When the beam current is high, the temperature of the sample is not controlled completely by holder temperature because the ion beam itself heats up samples during the implantation. It can be seen that the optimum I_b is around 50mA at T=250^{0}C.

c. Sample holder temperature T

Experiments on the temperature were made from 150 to 400 °C. The beam energy and current were set at 1.5 keV and 50 mA based on the above results. The improvements of V_{oc} and J_{sc} as a function of the temperature are shown in Fig.4.4 (a) and (b). It can be seen that both V_{oc} and J_{sc} increase slowly with the temperature until 250 °C, then decrease rapidly above 350 °C. The decreases may be caused by hydrogen diffusing out the samples at high temperature, as we will see in an annealing experiment in the next chapter. Fig.4.4 also suggests that the optimum temperature is in the range of 250 to 300 °C.

d. Implantation time

Implantation duration was varied from 4 to 20 minutes. Fig.4.5 (a) and (b) show the improvements of V_{oc} and J_{sc} as a function of time. These show that the improvements increase with the time, and then tend to become saturated. Fig.4.6 shows a variation of relative improvement of cell efficiency with time. In this experiment, the initial cell efficiency was about 7%, hydrogen treatment increasesd the efficiency to 8.3%, about 18% improvement. It can be seen that both Fig.4.5 and

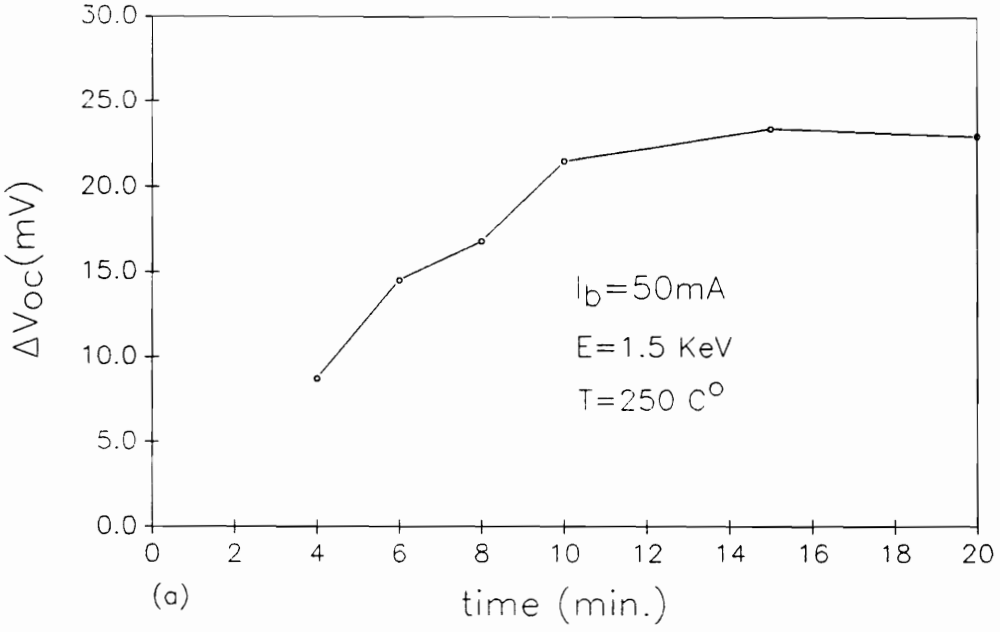

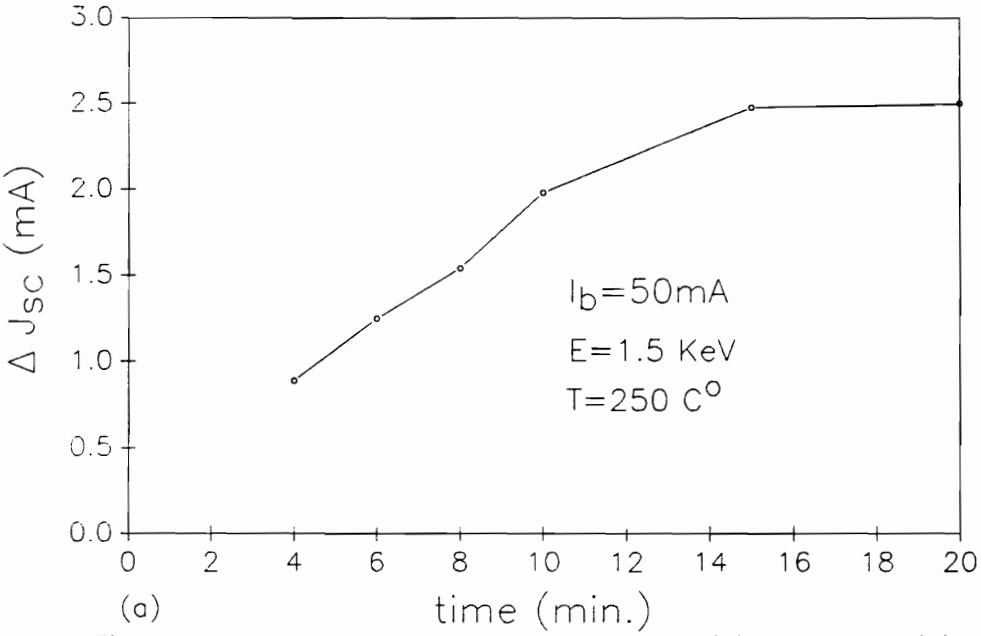

Fig.4.5 Implantation duration effect on V_{oc}(a) and on J_{sc}(b)

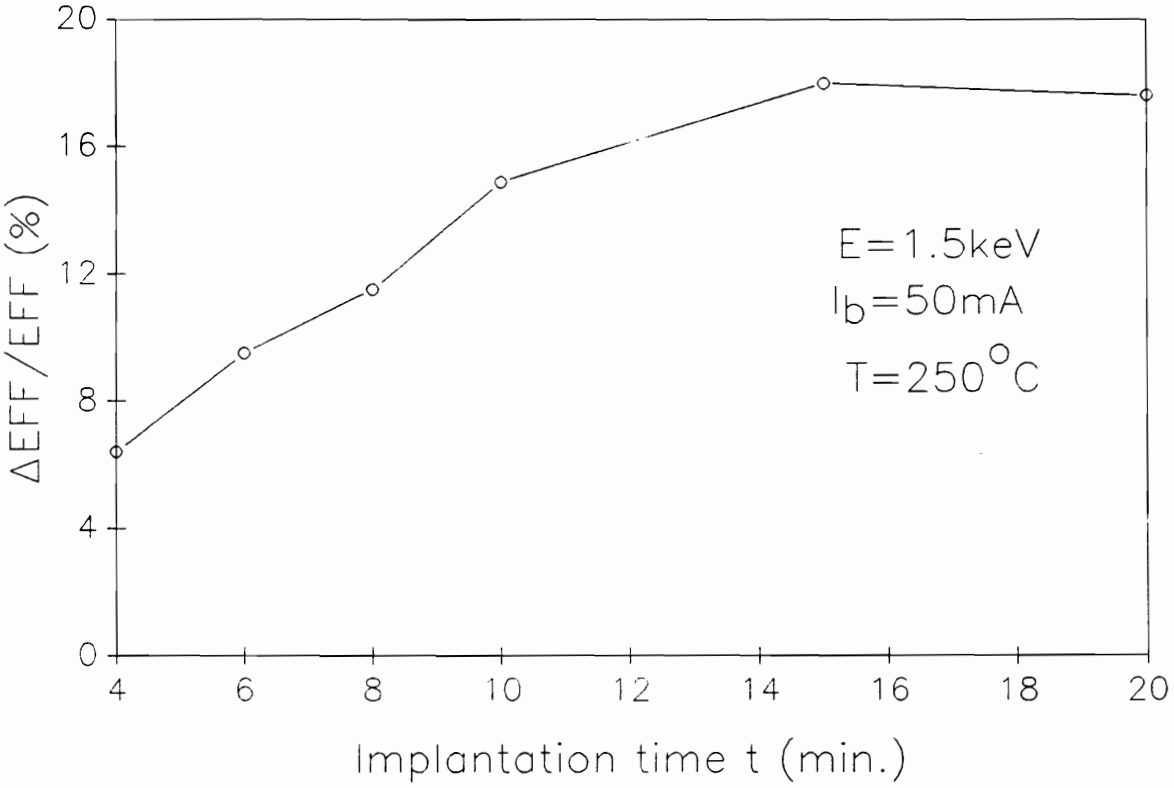

Fig.4.6 Relative EFF improvement vs. implantation time

4.6 show a similar saturation behavior. The saturation time in this experiment is about 15 minutes. The cell performance will not change significantly with implantation time longer than the saturation time. Similar results were also reported by other authors [3], but no explanation was given. The reasons for the saturation are still not clear. The following two possible reasons are suggested:

i. Complex effect

A certain percent of implanted hydrogen will form acceptor-hydrogen complexes. For instance, boron-hydrogen complexes have been confirmed from hydrogen implantation experiments on p type boron doped materials by FTIR measurements [18]. The hydrogen atoms in these complexes act as compensators for boron, and increase the sample's resistivity near the surface. Six-fold increase in resistivity has been reported based on spreading resistivity measurements [19]. Thus, the result of the complexes is to decrease carrier concentration in p-type material and increase the contact and series resistance of cells. The number of complexes will increase with hydrogen dose or implantation duration.

ii. Implantation defects

The longer implantation duration increases the total hydrogen dose and produces more implantation defects near the surface region. As we will see, in our TEM experiments, the surface damage strongly depends on hydrogen dose. If the surface is seriously damaged, most of the hydrogen may just be trapped at the surface region to passivate the defects caused by the implantation.

Both the implantation defects and complexes increase with the implantation duration. However, before the saturation time, they may play a secondary role and hydrogen passivation effects dominate the implantation process. After the saturation time, the negative effects would compete with the passivation effects and tend to compensate each other. It should be mentioned that the saturation time varied with materials of different defect concentration. As we will see in the next section, the saturation time changes with different initial cell efficiencies.

4.4. Cell initial parameters and their improvements

Hydrogen passivation effects on solar cells with different initial values of V_{oc}, J_{sc} and EFF were examined. Fourteen cells were deliberately chosen to give a range of the initial cell parameters. The ranges of these parameters were :

V_{oc}: 436 - 571 mV, J_{sc}: 16.12 - 21.82 mA

FF: 0.54 - 0.73 EFF: 3.79 - 8.85 %.

The implantation condition was: E=1.5 keV, I_b=50 mA, T=250°C and t=15 min. Table 4.1 lists the 14 cells' parameters before, (a), and after, (b), the hydrogen treatment.

It can be seen from the table that all the parameters changed in positive directions after the hydrogen implantation, except for fill factor, FF. FF increased in 10 cells, did not change in 2 cells, and decreased in two cells. In general, it did not change significantly. The other parameters, however, varied over large ranges according to

their initial values. In order to identify the effect of the initial value clearly, the improvement of each parameter was plotted as a function of its initial values. The results of V_{oc}, J_{sc} and EFF are shown in Fig.4.7 and 4.8, respectively. A general trend of these results is that a cell with a lower initial efficiency is expected to have larger improvement by hydrogen passivation. The linear regression and the slopes in Fig.4.7-4.8 indicated that there was a limit in initial values for the passivation. If a cell has an initial efficiency higher than the limit, the passivation would be inefficient. This limit will change for different materials with different defect structures, because the passivation effects varies with different kinds of defects [20].

It was also found that the saturation time, discussed in the last section, changed with initial cell efficiency. Fig.4.9 shows the cell efficiency improvement as a function of implantation duration for cells with three initial efficiencies, 6.3 %, 7.1 % and 8.8 %. The saturation time for the three cells were about 8, 15 and 20 min., respectively. The conclusion is that poor quality cell need longer passivation times.

Table 4.1 Improvements of cell parameters due to hydrogen passivation (a): before hydrogenation; (b): after hydrogenation.

V_{oc}(mV) (a)	(b)	J_{sc}(mA) (a)	(b)	FF(%) (a)	(b)	EFF(%) (a)	(b)	$\Delta EFF/EFF_o$ (%)
436	495	16.12	20.45	0.54	0.58	3.795	5.871	54.7
487	522	17.57	21.01	0.57	0.59	4.877	6.471	32.68
457	505	17.51	20.83	0.62	0.62	4.961	6.522	31.46
520	552	16.51	20.55	0.58	0.61	4.979	6.92	38.9
531	559	18.35	19.98	0.58	0.60	5.651	6.701	18.58
508	545	19.01	21.44	0.65	0.67	6.307	7.829	24.13
522	557	18.85	21.60	0.72	0.73	7.085	8.703	22.84
538	556	18.57	20.68	0.71	0.72	7.039	8.351	17.73
543	560	19.63	22.01	0.68	0.68	7.248	8.381	15.63
514	564	21.90	22.93	0.69	0.71	7.767	9.178	18.17
558	569	21.1	23.7	0.70	0.72	8.242	9.709	17.7
554	568	20.76	21.88	0.72	0.71	7.093	8.351	17.73
562	570	20.22	20.89	0.73	0.71	8.295	8.573	3.35
572	577	21.82	22.3	0.71	0.72	8.846	9.264	4.73

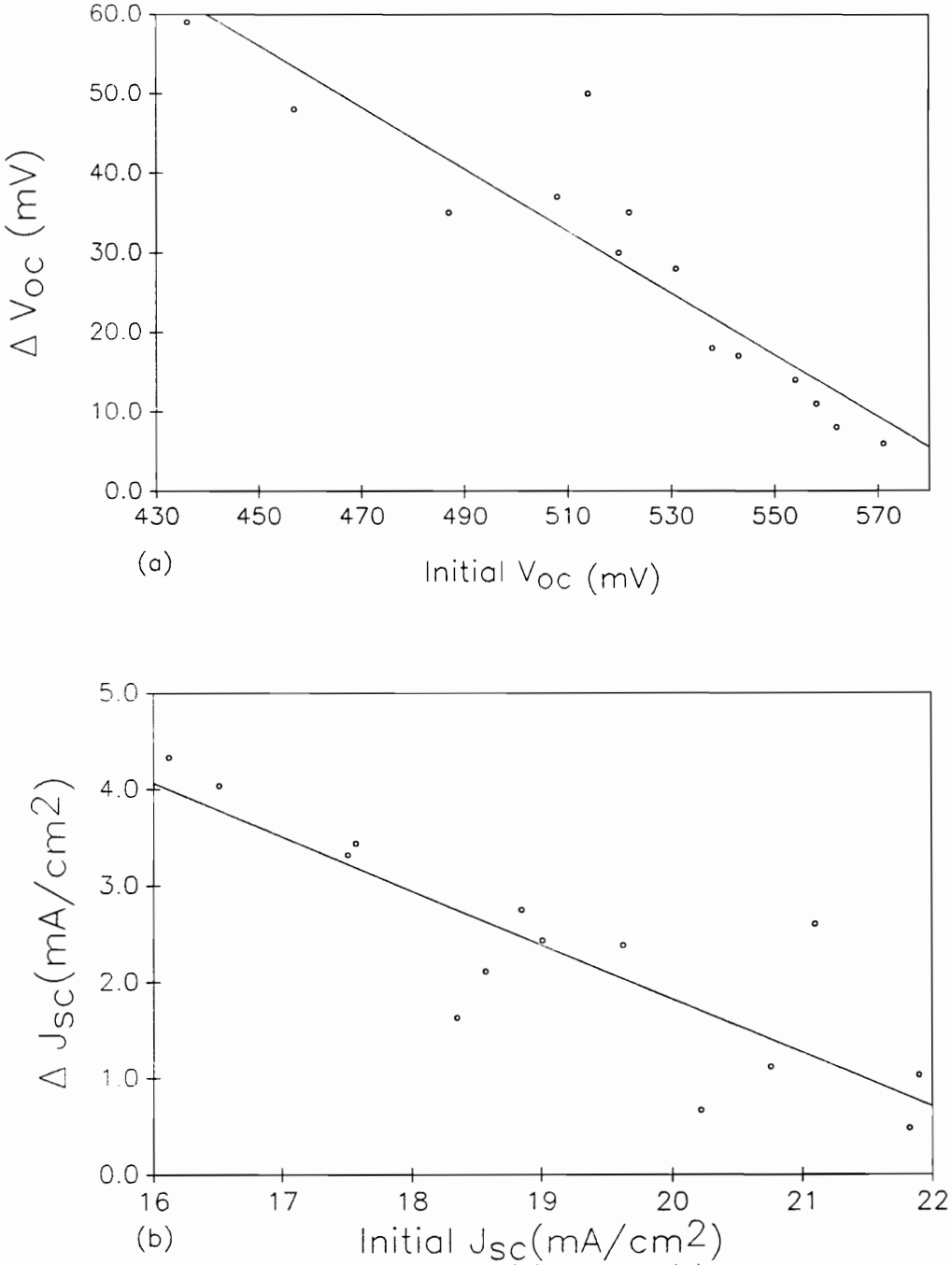

Fig.4.7 Improvements of V_{oc} (a) and J_{sc} (b) as a function of their initial values

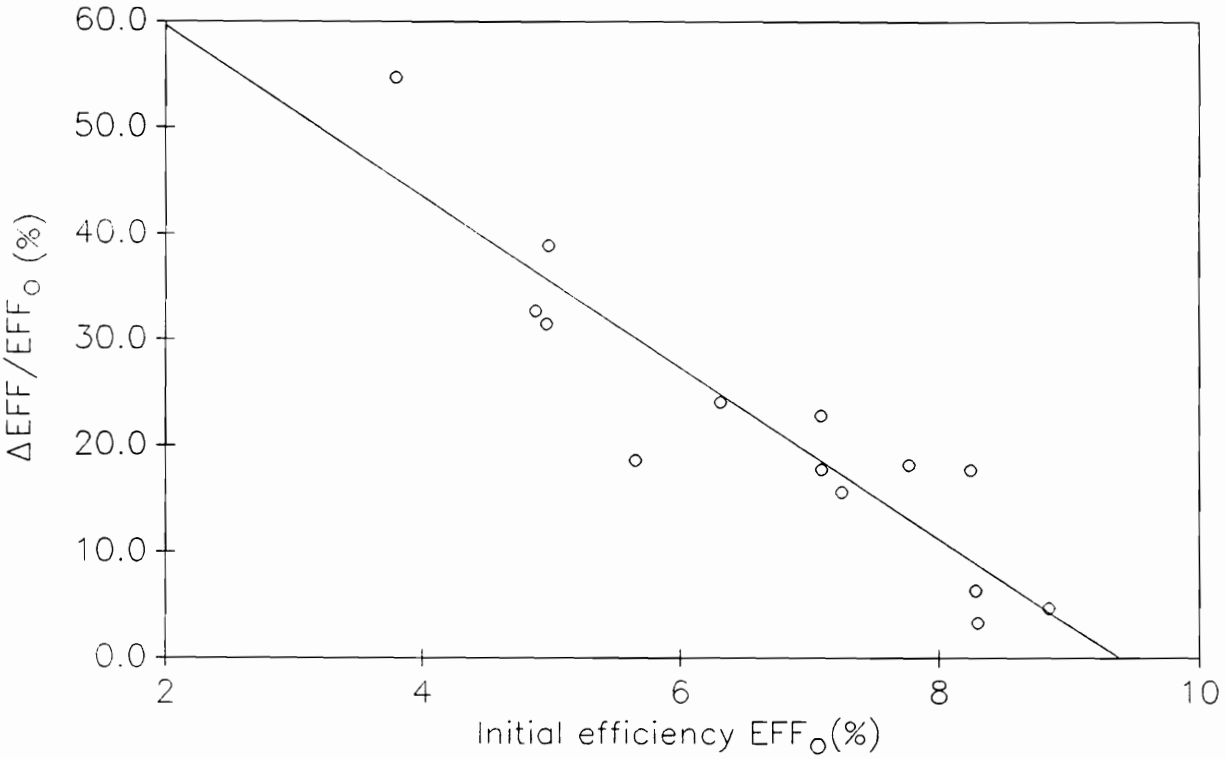

Fig.4.8 Relative efficiency improvement as a function of the initial efficiency values.

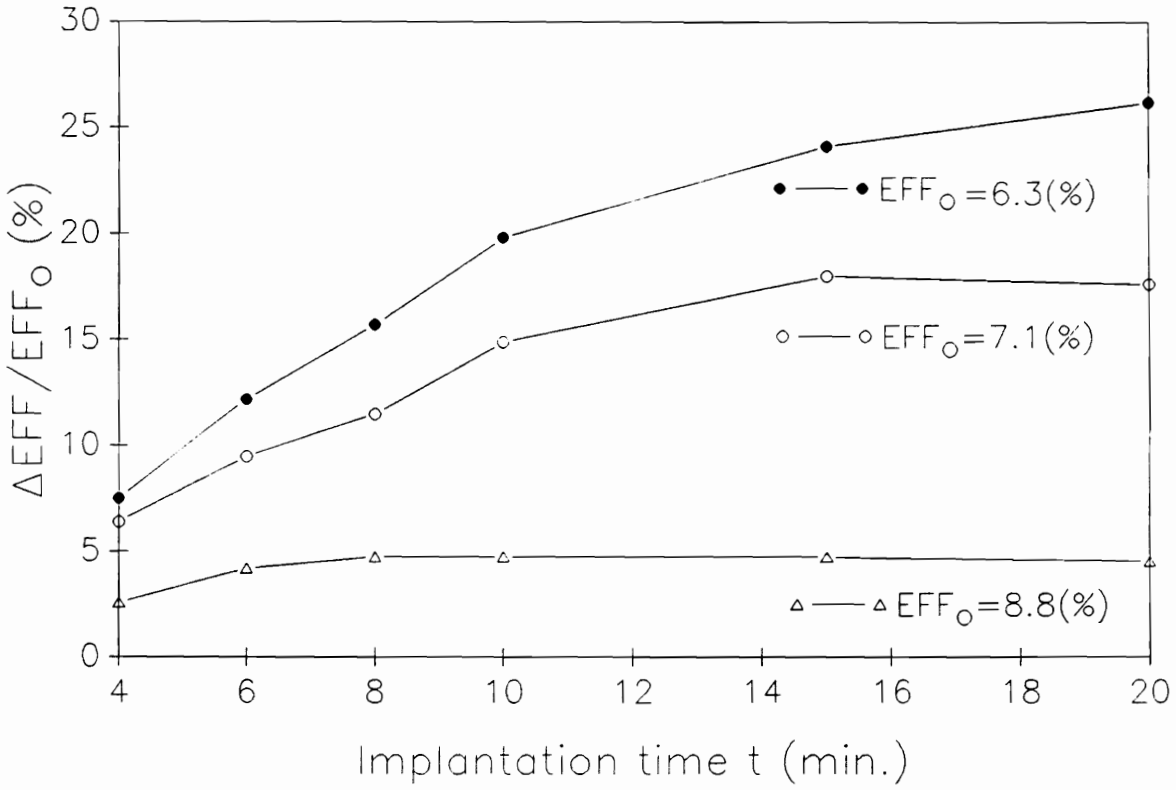

Fig.4.9 Relative efficiency improvements as a function of the time for different initial efficiencies EFF_O

4.5 FTIR study of hydrogen-silicon bonds

The purpose of this study was to assure that hydrogen was actually implanted inside the sample after the implantation. FTIR experiments were conducted on three Wacker polycrystal silicon samples from different batches. The samples were polished on both sides by use of a Nalco solution. The solution was made of deionized water and 2350 colloidal silica(B8L811) in a ratio of 7:1. Each side of the samples was polished under a pressure of 20 pounds for 1.5 hours, and then without pressure for 10 minutes. All three samples were implanted at same time under the following conditions: beam energy E_b of 1.5KeV, beam current I_b of 55 mA, sample holder temperature T of 250 °C, implantation time t of 20 minutes. IR spectra of the three samples measured at room temperature are shown in Fig.4.10. These three samples were assigned as S1, S2 and S3. Several peaks due to Si-H bond were expected in the IR spectra [5]. The most intensive one, a stretching band, was expected to appear around 2100 cm^{-1} wave number [16]. But the peaks shown in Fig.4.10 for all three samples were too weak to identify. This is because the Si-H bond has a very low IR absorption coefficient, and the peaks were suppressed by noise at room temperature. On the other hand, Si-O peaks around 1100 cm^{-1} wave number [17] were strong enough to be identified. Different oxygen content among the three samples appears, with S1 having the highest and S3 having the lowest oxygen content. In order to identify Si-H bond, FTIR measurements at low temperature, 14 K, were conducted. The results are presented in Fig.4.11. It can be

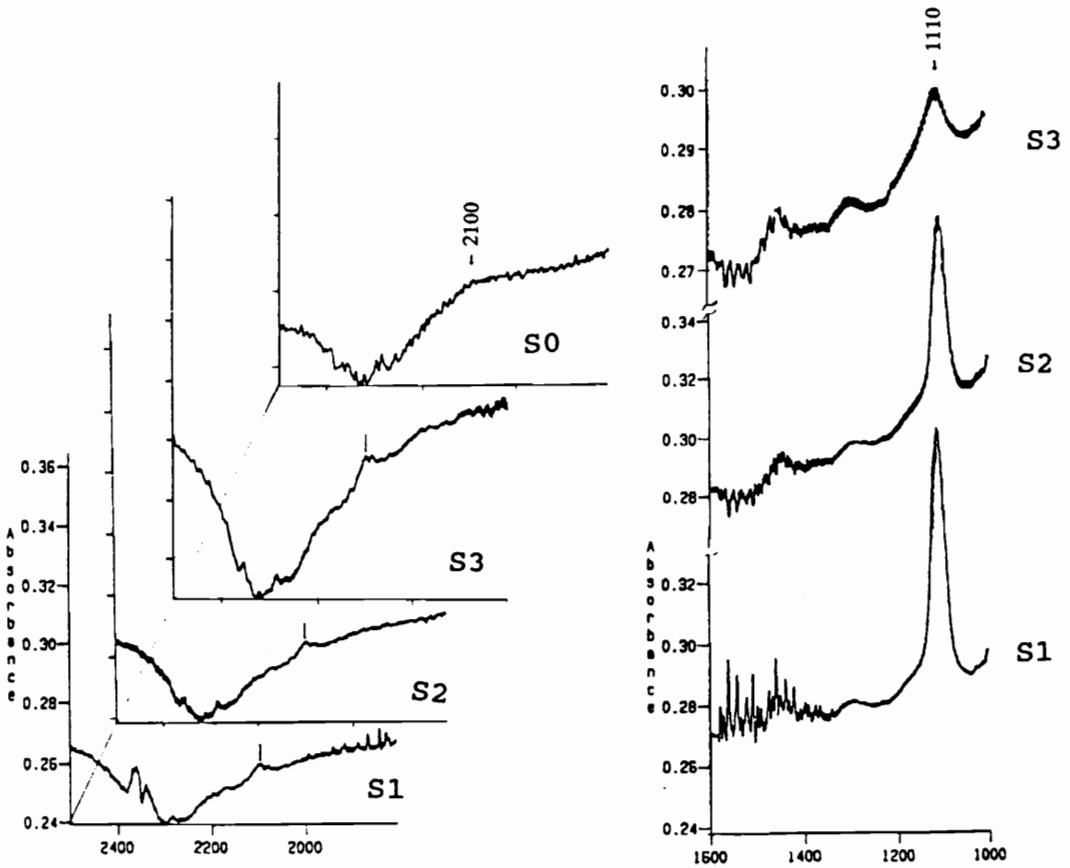

Fig.4.10 IR spectra at room temperature: (a) Si-H peaks at wave number about 2100 cm^{-1} for hydrogen implanted samples S1, S2, S3 and a virgin sample S0; (b) Si-O peaks at about 1110 cm^{-1} for samples S1, S2 and S3

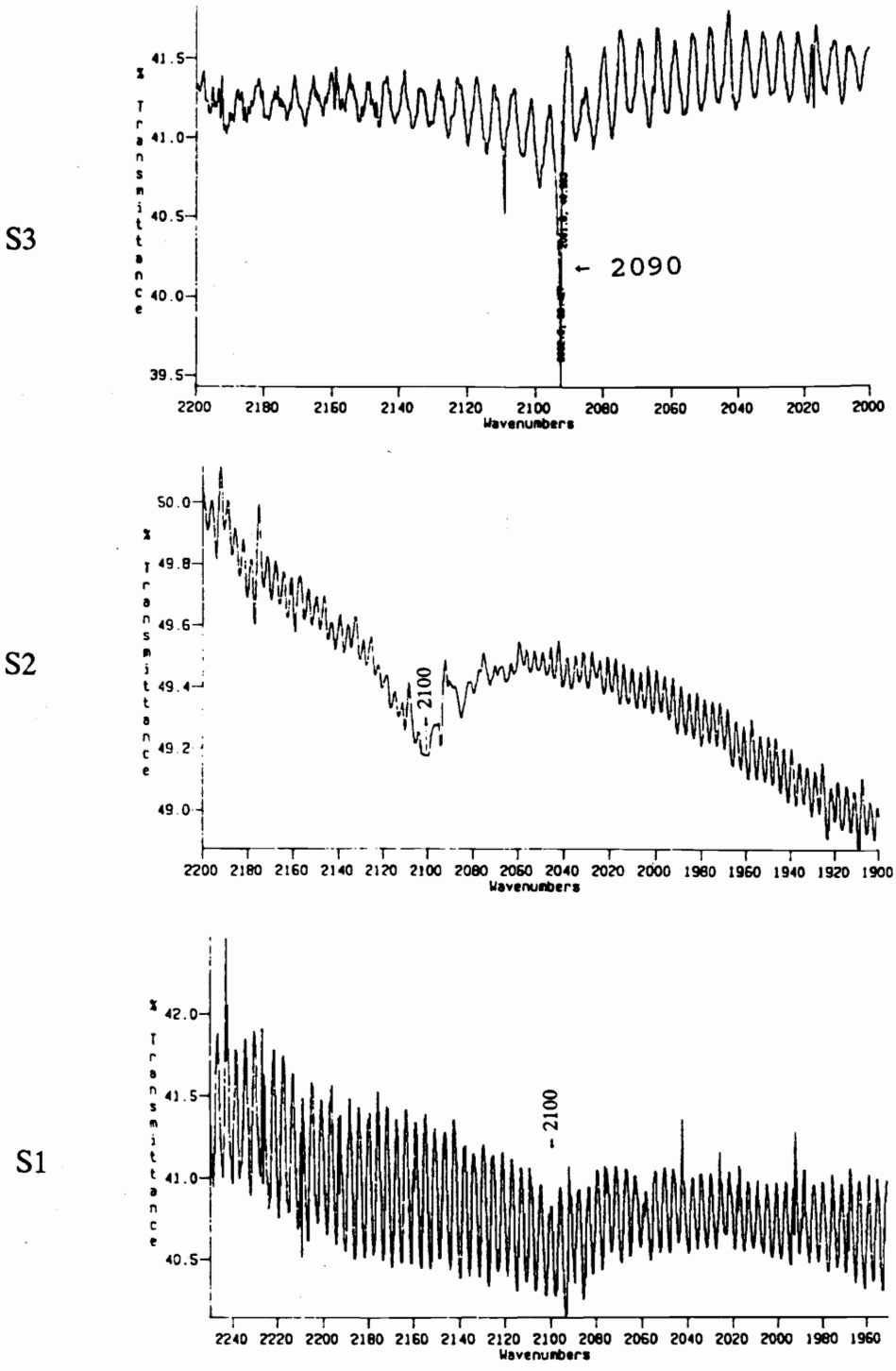

Fig.4.11 Si-H peaks at temperature of 14 K for hydrogen implanted samples S3, S2 and S1

seen that peaks around 2100 cm^{-1} appear clearly in samples S2 and S3. However, the peak is still weak in sample S1. These results indicated that S3 had the highest, and S1 the lowest hydrogen content.

Si-C peaks around 607 cm^{-1} wave number were also observed in the three samples, as shown in Fig.4.12. Relative contents of oxygen, carbon and implanted hydrogen for these three samples based on the IR intensities is summarized in Table 4.2.

Table 4.2 Relative Content of O, C, and H from IR Measurements

sample	oxygen	hydrogen	carbon
S1	high	low	medium
S2	medium	medium	low
S3	low	high	high

It can be seen from the table that the higher oxygen concentration corresponds to the lower implanted hydrogen into the polysilicon samples, and vice versa. However, a proportional correlation between oxygen and hydrogen content was reported in high energy hydrogen implantation experiments(above 400keV) on crystalline silicon materials [17]. A possible reason for the opposite correlation might be the different oxygen configurations in poly and crystalline silicon. In crystalline silicon, oxygen occupy the interstitial position in the crystal lattice and distort the

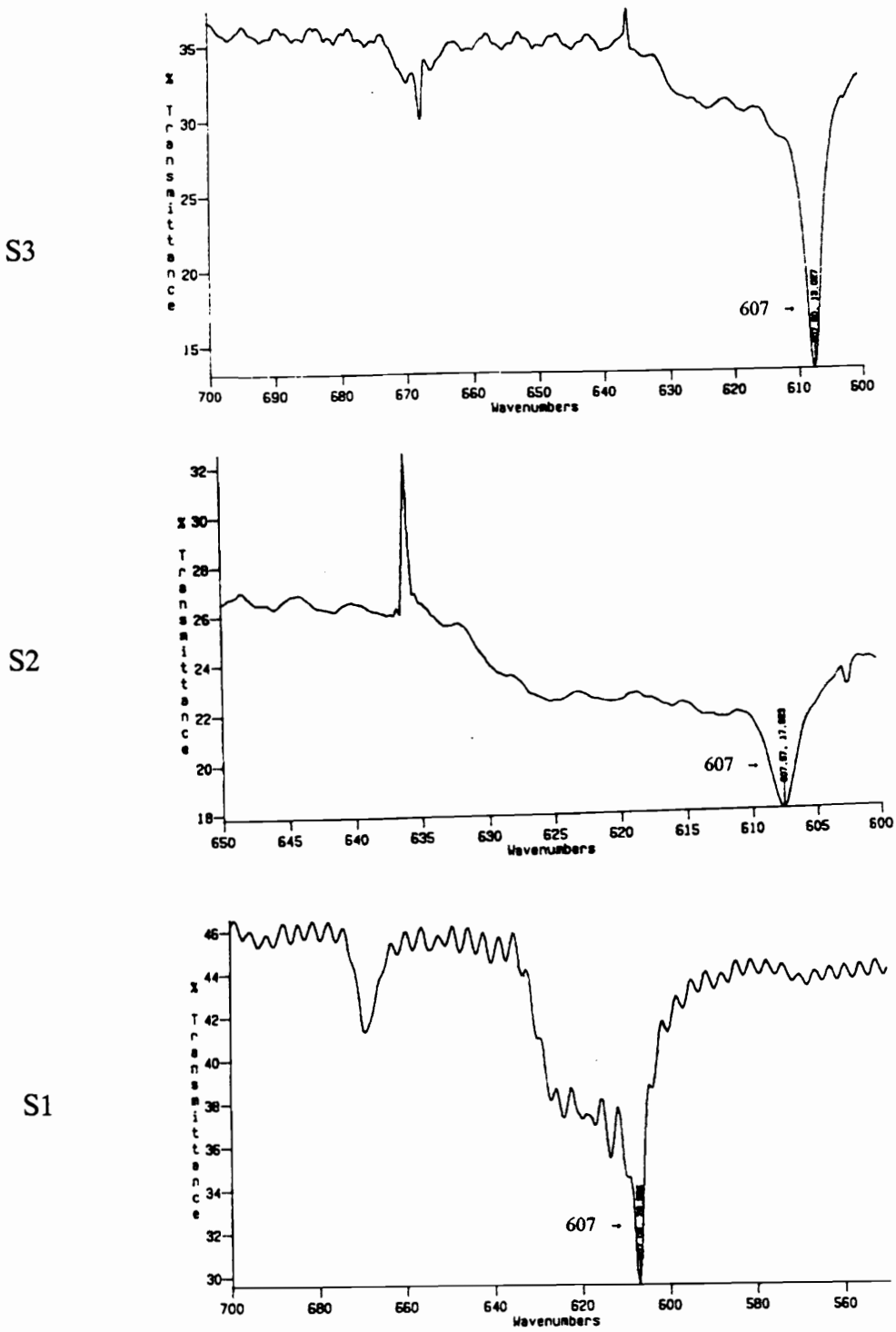

Fig.4.12 Si-C peaks around 607 cm^{-1} at 14 K for S3, S2 and S1

lattice structure, which may help hydrogen diffuse into the material. On the other hand, in poly silicon, oxygen segregation along grain boundaries and dislocations may be potential sites for the implanted hydrogen. In this case, oxygen may block hydrogen diffusion or trap hydrogen to form oxygen-hydrogen complexes. More experiments are needed to explain this conflict.

4.6. TEM studies of hydrogen implantation

a. Hydrogen diffusion through dislocations

An effort was made to see how hydrogen diffuses into poly-Si materials. TEM cross section experiments were performed on crystalline and polycrystalline ribbon Si materials. The crystal Si is a [100] orientation and dislocation free material. Both crystal Si and poly-Si ribbon underwent the same hydrogen implantation conditions. The condition was: beam energy of 1.5 keV, beam current of 55 mA, temperature of 250°C and duration of 20 minutes.

Fig.4.13 displays TEM cross section pictures for the crystal Si viewed at different positions. This shows that the implantation causes surface damage and produces some dislocation loops near the implanted surface, with some bubbles connecting the dislocations.

The TEM cross sections of ribbon materials are shown in Fig.4.14. It was found that more dislocations were extended into the bulk and there were more bubbles in the ribbon materials. A very clear bubble chain is shown in Fig.4.14 (b) and some

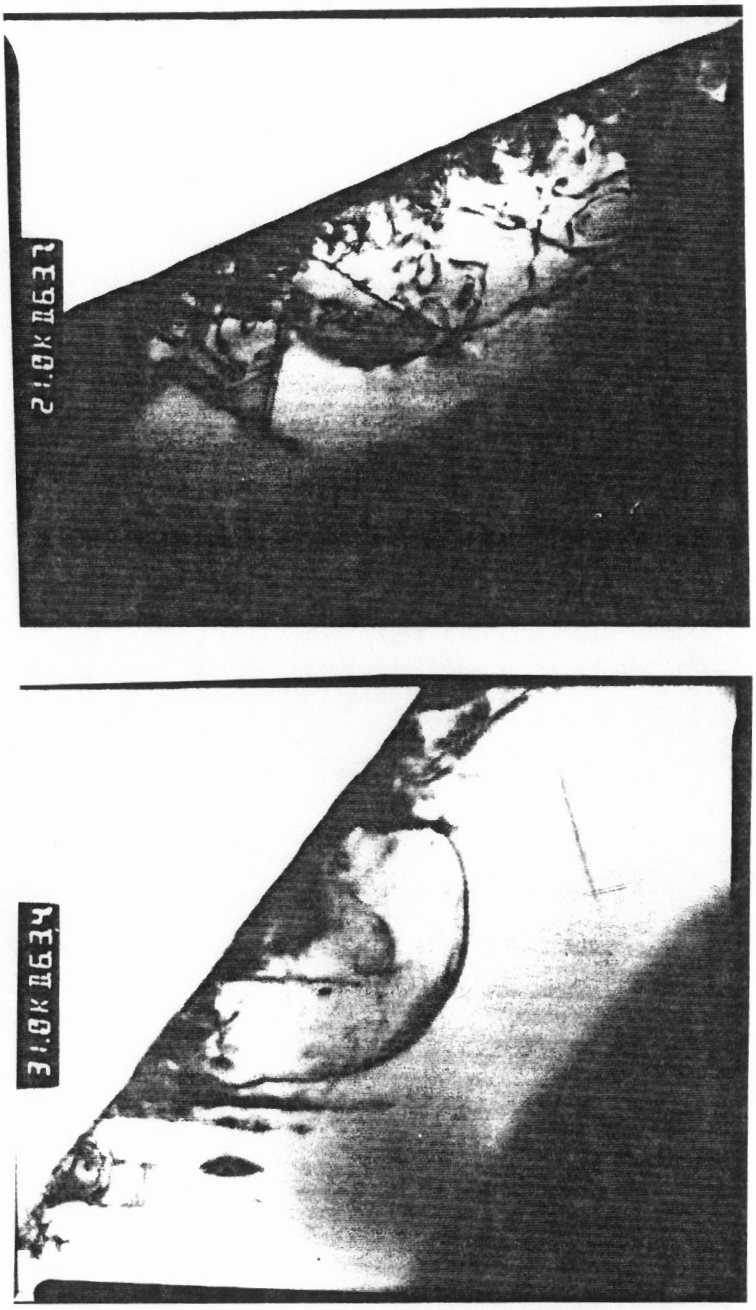

Fig.4.13 TEM cross-section at two view positions of crystalline Si sample bombarded with E=1.5keV and I_b=55mA hydrogen ion beam for 20 minutes

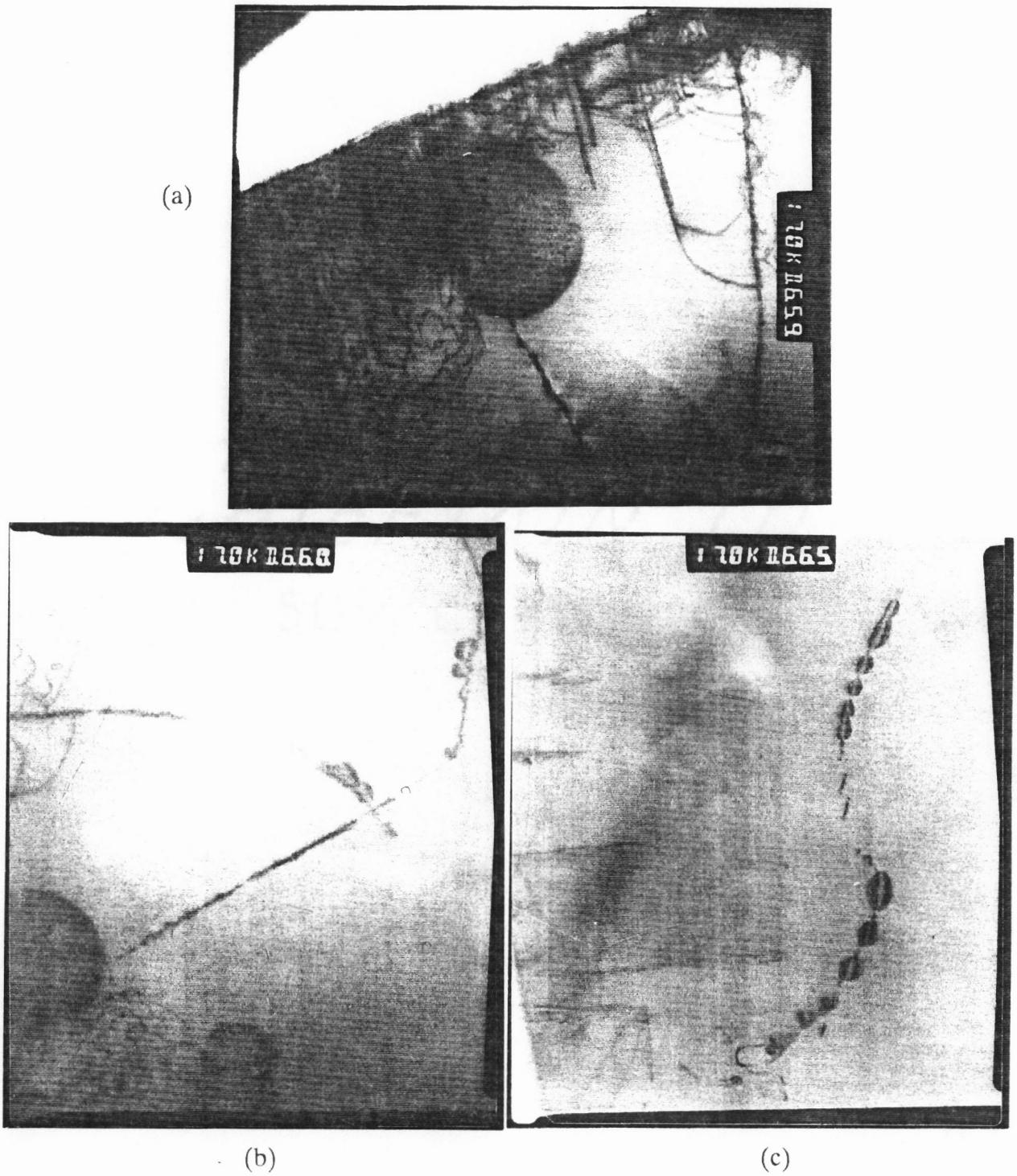

Fig.4.14 TEM cross-section pictures of Si ribbon sample (a) at the bombarded surface, (b) bubble chain in bulk, (c) bubbles in dislocations at depth about 30 μm

bubbles connected with a dislocation is shown in Fig.4.14 (c). These bubbles were observed at a depth about 30 μm from the implanted surface. No bubbles were found near the unplanted surface and in the virgin sample. Therefore, the results indicated that the bubbles were related to hydrogen implantation. It is very reasonable to believe that the bubbles in the TEM pictures are the strain field due to hydrogen at dislocations. The results provided experimental evidence for the postulation that dislocations act as paths for hydrogen diffusing into silicon. It also suggested that TEM cross-section measurements can be used to study hydrogen diffusion in poly-Si.

b. Surface damage due to implantation

Surface damage caused by implantation has been reported by several workers [12,15]. However, in low energy (1 - 2 keV) ion bombardment, which implantation parameter is the major factor responsible for the damage, and the degree of the damage, are still not clear. In order to answer these questions, the following experiments were designed. A series of samples was prepared by implanting hydrogen at different doses and ion beam energy E, at a constant temperature of 250°C. Then TEM electron diffraction patterns were taken.

In our experiments, beam current of 55 mA or 0.68 mA/cm^2 was used, and the bombardment duration varies from 10 to 90 minutes corresponding to total hydrogen dose in a range of 2.5×10^{18} to 2.3×10^{19} ion/cm^2. It was found that when the dose was less than 7×10^{18}/cm^2, a lattice structure of the surface was maintained. A typical

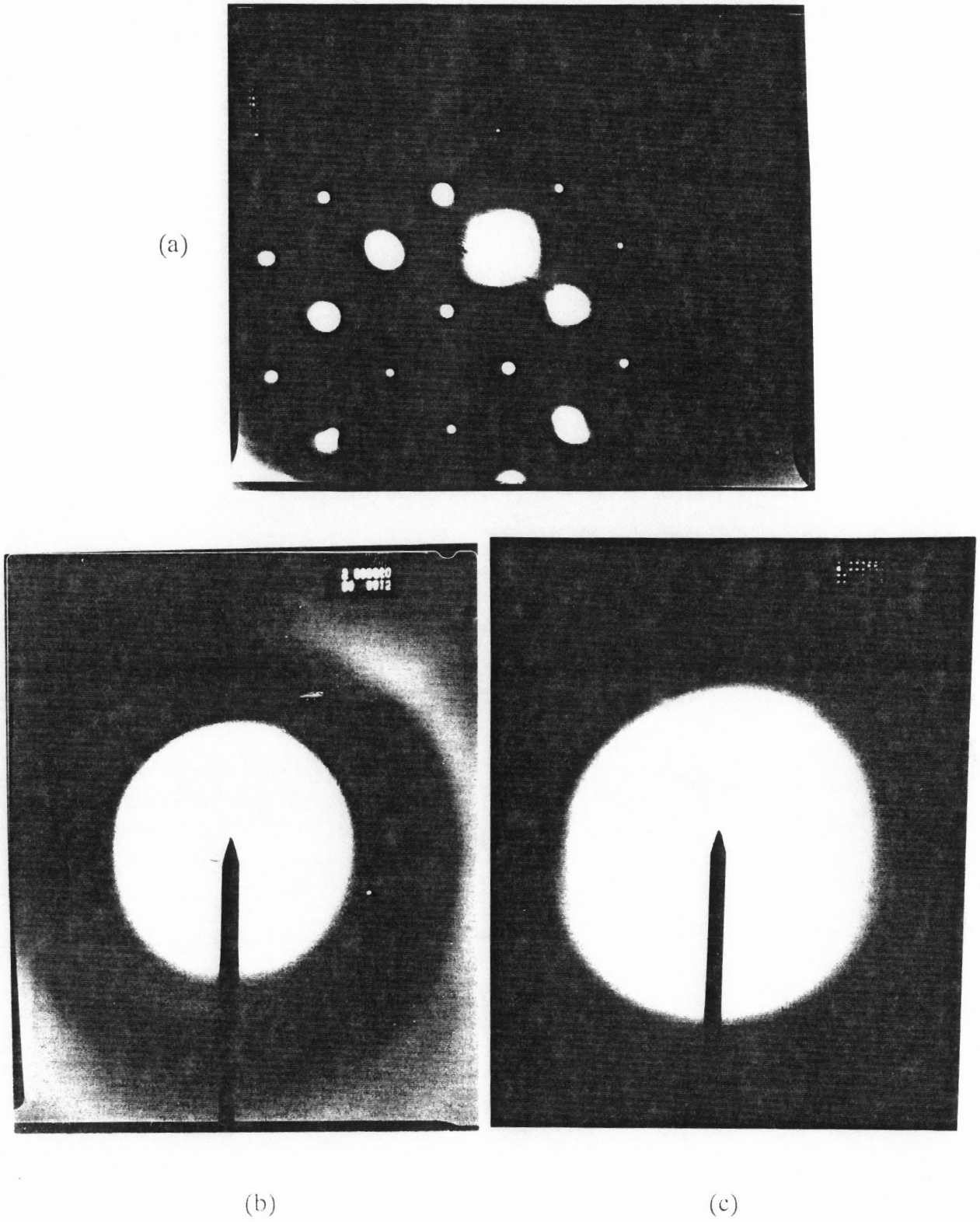

Fig.4.15 TEM electron diffraction patterns vary with hydrogen dose: (a) $7x10^{18}/cm^2$; (b) $1.5x10^{19}/cm^2$; (c) $2.3x10^{19}/cm^2$

diffraction pattern for a sample bombarded with $7x10^{18}$ ion/cm^2 at 2 keV beam energy is shown in Fig.4.15(a). However, when the dose was greater than $1x10^{19}$/cm^2, the surface became amorphous. Fig.4.15(b) and (c) show the diffraction patterns at 2 keV beam energy and dose of $1.5x10^{19}$ and $2.3x10^{19}$/cm^2, respectively. The experiments were repeated for a beam energy of 1keV, and no significant difference was observed in the diffraction patterns. Therefore, the results indicated that in low energy hydrogen implantation (below 2KeV), the total dose, not the beam energy, was the major factor for the surface damage.

4.7 Conclusions

A systematic study of implantation parameters for backside hydrogenation has been conducted. The optimum implantation conditions for the samples with initial efficiency about 7% were: beam energy of 1.5KeV, beam current in the range of 50-55mA, sample temperature in the range of 250-300 C and implantation duration of 15 minutes. Under these conditions, 18% improvement was achieved. The improvements were a strong function of the initial cell efficiency. It was found that the hydrogenation favored the cells with low initial efficiency. The lower the initial efficiency, the larger improvement is expected, but the longer implantation duration is needed.

The interaction of hydrogen-dislocation was observed by TEM cross-section measurements. The results provided experimental evidence that dislocations acted

as paths for hydrogen diffusing into silicon. The TEM electron diffraction patten measurements showed that in the low energy hydrogen implantation (below 2 keV), the total dose, not the beam energy, was a major factor responsible for the surface damage.

References :

[1] Y.S.Tsuo, andJ.B. Milstein, Appl. Phys. Lett. 45, p971, (1984).

[2] J.I.Hanoka, Appl. Phys. Lett. 42, p618, (1983).

[3] H.Yagi, H., et. al., 19th IEEE Photovoltaic Spec.Conf., p1600 (1988).

[4] S.Martinuzzi, et. al., 18th IEEE Photovoltaic Spec.Conf., P1069, (1987)

[5] S.J.Pearton, J.W.Carbett, and T.S.Shi, Appl. Phsy. A. 43, p153, (1987).

[6] W.E.Spear and G.P.LeComber, Phil. Mag., 33 p935, (1976).

[7] H.Fritzsche, M.Tamielian, C.C. Tsai and P.J.Gaczi, J.Appl.Phys.,50, p3366, (1979)

[8] K.Morigaki and S.Nitta, Noncrystalline Semiconductors, CRC, Vol.II, p53, (1987)

[9] J.Chevallier and M.Aucouturier, Ann. Rev. Mater. Sci., 18, p219, (1988).

[10] S.Matinuzzi, Rev. Phys. Appl., 22, p637, (1987).

[11] J.I.Pankove, "Semiconductors and semimetals", Vol. 21D, p261, (1984).

[12] Y.S.Tsuo and J.B.Milstein, J. Appl.Phys. 57, p5523, (1985).

[13] B.L.Sopori, J. Appl. Phys. 64, p5264, (1988).

[14] Y.S.Tsuo andJ.B.Milstein, Appl. Phys. Lett., 45, p971,(1984).

[15] J.C.Muller, et. al., Solar Cells, 17, p201,(1986).

[16] G.R.Bai, et. al., Solid State Commun., 56, p277, (1985).

[17] W.M.Qi, G.R.Bai, T.S.Shi and M.L. Xie, Mater. Lett., 3, p467,(1985).

[18] M.Stavola, S.J. Pearton, L. Lopata and W.C.Dautremont-Smith, Appl.Phys.Lett.,50, p1086, (1987).

[19] J.I.Pankove, D.E.Carlson, J.E.Berkeyheiser and P.O. Wance, Phys.Rev. Lett., 51, p2224, (1983).

[20] E.Courcelle, J.C.Muller, P.Siffert and C.Belouet, Solar Cells, 14, p157,(1985).

Chapter 5

SEM-EBIC Study of Silicon Grain Boundaries and Surface Recombination Velocities

5.1 Introduction

The scanning electron microscope (SEM) used in the electron beam induced current (EBIC) mode has become an important tool in semiconductor research during the past ten years. In this technique, the charge carriers generated by the electron beam of the microscope are collected by an electric field in the material of interest, such as a p-n junction or Schottky barrier, and are sensed as a current in an external circuit. When this current is supplied to the video of the SEM, its image reveals inhomogeneities in the electrical properties of a given material. A high resolution electron beam, typically a few hundred A° wide, can generate carriers in a relatively small volume, therefore, the EBIC method provides a measurement with a far greater resolution than other traditional methods.

The technique has been used to determine the minority carrier lifetime, diffusion length, and surface recombination velocity for semiconductors. Collection of the charge carriers generated by the electron beam reveals the location of defects, such as point defects, dislocations and grain boundaries. An important advantage of the SEM-EBIC results from the small volume probed by the electron beam. Standard Hall effect, lifetime and junction measurements sample a much larger volume and are

consequently insensitive to the local defects. In contrast, when an electron beam of an SEM scans such a defect, the trap density within the probed volume is many orders of magnitude larger than would be indicated by non-microscope measurements. Furthermore, the density of the carriers generated by the electron beam may be much larger than those in conventional measurements.

In this chapter, some basic concepts of the EBIC technique are reviewed, and are applied to the determination of grain boundary recombination velocity, the minority carrier diffusion length and surface recombination velocity. A technique combining EBIC and electron channeling to study Si grain boundaries is discussed. The use of EBIC to monitor the effects of backside hydrogen passivation of grain boundaries is presented.

5.2 Basic concepts of EBIC

a. Carrier collection and defects

In the SEM-EBIC technique, the sample itself acts as the detector or collector of the electronic charge that results in the video signal. If the specimen is a p-n junction or Schottky diode, and therefore capable of supporting an internal electric field, the mobil charge carriers generated by the impinging beam within the sample move in response to the field to produce a measurable signal. The incident electron beam is a known quantity. The collection efficiency of the carriers depends upon the properties of the sample. In particular, a spatially inhomogeneous carrier collection

due to defects, such as dislocations and grain boundaries, can be imaged in the EBIC through the point-by-point collection of a large number of individual charge carriers. Therefore, the collection efficiency and current signal are higher in a defect free region than in a region with defects. Thus, when these current signals are fed back to the SEM screen, regions with defects appear darker and defects free regions appear brighter.

b. Excitation range and generation rate

Electrons with keV energy striking solid materials lose energy during penetration by scattering valence and core electrons and generating electron-hole pairs. These events result in a deviation of the trajectory of high energy electrons, so that the process may be regarded as one in which electrons are continuously slowed. Also electrons may be scattered from the nuclei within the material with a small loss of energy and undergo a large angular deviation from their original trajectories. The result of this scattering is that the focused electron beam of the SEM becomes mushroom-shaped within the sample, leaving a trail of low energy secondary electrons and holes along the individual paths. In addition to the absorption of energetic electrons in a semiconductor by way of electron-hole pair generation, energy losses also occur due to backscattering and reflection of the electrons. The fraction of the total incident electrons that are backscattered is represented by a backscattering coefficient which has a relative flat response for a beam energy less than 50 keV [1].

An empirical expression for the depth of penetration of primary electrons,

(electron range R) is given by [2]:

$$R = \frac{C}{\rho} E^{1.75} \qquad 5.1$$

where C is a constant, ρ is the density of the material (gm/cm^3) and E is electron beam energy in keV.

For silicon, the following empirical relation has been found [2]:

$$R = 0.0171\ E^{1.75} \qquad 5.2$$

with R in μm and E in keV. Table 1 gives R for silicon for selected value of E according to Eq.(5.2). Similar relationships have been given for other semiconductors [3].

Table 5.1. The values of R(μm) in Si for different beam energies E(keV)

E	5	10	15	20	25	30	35	40	45	50
R	.3	1	2	3.2	4.75	6.6	8.6	10.9	13.3	16

In addition to R, the injected current, or the number of the electron-hole pairs, g_o, generated by the electron beam, is of interest. It is given by [4]:

$$g_o = \frac{E_b I_b (1-f)}{E_{eh} q} \qquad 5.3$$

where:

I_b = electron beam current

E_b = beam energy

f = fraction of election beam energy that is reflected by the sample

E_{eh} = the energy required to generate a single electron-hole pair

f can be determined experimentally but is most often estimated as half of the backscattering coefficient which is independent of beam energy. In silicon, f of 0.08 is used [5].

E_{eh} is a constant for a given material, and is independent of the beam energy. E_{eh}, however, is correlated with the band-gap energy. For most semiconductors, E_{eh} is very close to three times the band-gap energy [6].

Using relation (5.3), a simple numerical estimation can be made. If a 20 keV beam of 10^{-10} amp. current is applied, roughly 3.5×10^{12} carrier pairs will be generated per second in silicon. At 20 keV, with R=3.2 μm, the average generation rate within an excited volume of $4/3\ \pi\ R^3$ will be 2.5×10^{22} pairs/(sec.cm^3). This simple calculation shows that a beam in the SEM is capable of creating a enormous number of carriers in silicon. Of course, in the steady-state, the population is smaller because the carriers generated by the beam recombine and diffuse away from the generation region.

The one dimensional depth distribution of the pair generation has been determined experimentally for silicon by Everhart and Hoff [6] and has been verified

by Possin and Norton [7]. They approximated the generation function with a polynomial expression of the form

$$g(z) = \left(\frac{g_o}{R}\right)\left[0.6+6.21\left(\frac{z}{R}\right)-12.4\left(\frac{z}{R}\right)^2+5.69\left(\frac{z}{R}\right)^3\right], \quad 0 \le z/R \le 1.1 \qquad (5.4)$$

where z is in the electron beam direction, and the sample surface is set as z = 0.

5.3 EBIC characterization of grain boundaries

For polycrystalline silicon, such as the Wacker cast or the edge-defined film-fed growth (EFG) silicon ribbon, the grain boundaries are approximately normal to the plane of the slice or sheet and often have quite long segments of constant recombination. This favorable geometry suggests the possibility of an analytical description for induced current profiles by representing the grain boundary as a interface embedded in a semiconductor with uniform minority carrier diffusion length L, and having surface recombination velocity v_s, [8]. Such a model provides a basis for deducing the values of v_s and L from an experimental EBIC profile.

Marek [9] gave a treatment of this problem for the case of excitation by an election beam using a spherical generation volume. He showed that the value of L could be deduced experimentally from the half-width of the EBIC profiles. However, the determination of v_s was not considered. Zook [10] calculated the induced current profile and determined v_s by treating the grain boundary as a surface, but in his

calculation a numerical value for L was assumed.

Donolato's work [8] marks the first significant attempt to understand the EBIC current line scan across a grain boundary, and gives analytical expressions describing the induced current profile. A procedure based on these expressions was used. The values of v_s and L were extracted from an experimental current profile by using two related integrals, for the profile area and variance. This procedure is well established and widely used to characterize polycrystalline materials [11,12].

Donolato's theory is as follows (The mathematical details are in ref.8.). Fig. 5.1 illustrates the configuration used for EBIC observation at a grain boundary of a polycrystalline solar cell. A basic assumption used in the calculations is that the essential contribution to the collected current generated by the beam arises from the neutral base region of the cell. Therefore, the background current, which is the current collected far away from the grain boundary recombination centers, can be expressed as [13]:

$$I_o = \int_0^\infty g(z)\, e^{-\frac{z}{L}} dz \qquad 5.5$$

where g(z) is given by Eq.(5.4) and exp(-z/L) is the carrier collection probability. The EBIC signal I(x), collected near the grain boundary, depends upon the recombination center density in the boundary and is a function of x, the distance from the boundary. The expression for I(x) has been derived by Donolato [8] by applying a Green's function method to the diffusion equation and related boundary

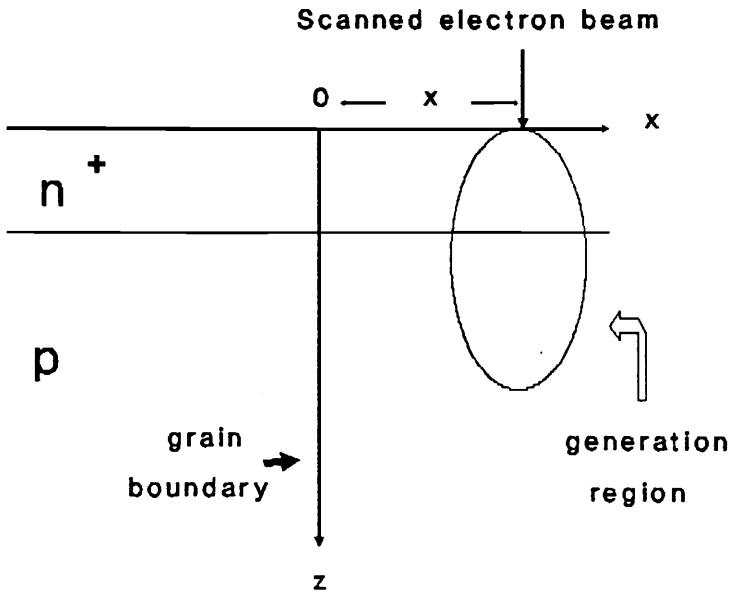

Fig.5.1 Diagram of a EBIC analysis of a grain boundary in a polycrystalline solar cell

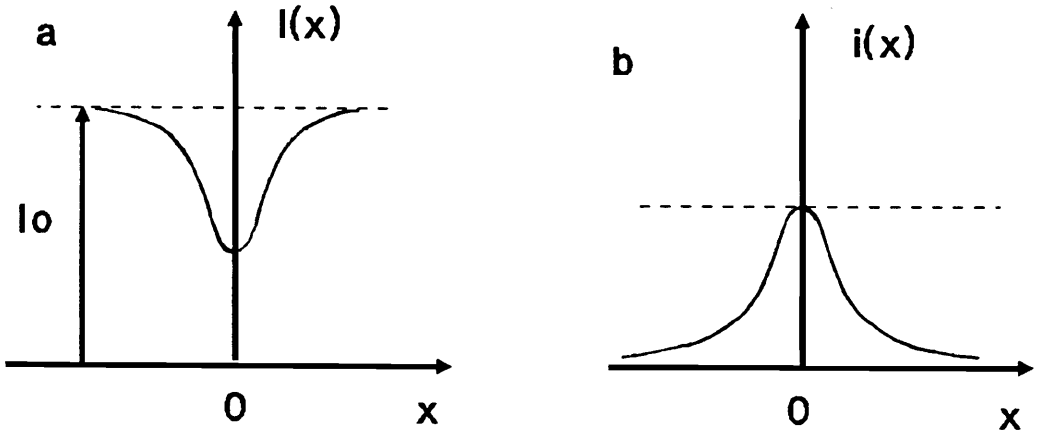

Fig.5.2 (a) EBIC signal profile at a grain boundary
(b) The related contrast profile

conditions. Both I_o and I(x) depend on the beam parameters. They can be determined experimentally as shown in Fig.5.2 (a). From I_o and I(x), the contrast current, i(x), is defined by:

$$i(x) = \frac{I_o - I(x)}{I_o} \qquad 5.6$$

The contrast profile is independent of E_b and I_b .

In order to extract the values of v_s and L from the contrast profile of a grain boundary, one should in principle describe the beam generation in a given experiment by a suitable function and then fit the theoretical profile to the observed one by an appropriate choice of v_s and L. However, a more convenient procedure to determine v_s and L is not by the fitting method, but from overall properties of the profile [14,15]. In this procedure, the two integrals related to the profile, the area of the contrast profile and the variance of the profile, are calculated. This allows one to determine the v_s and L simultaneously .

The area of the contrast profile is given by

$$A = \int_{-\infty}^{\infty} i(x)\, dx \qquad 5.7$$

This relation represents the integrated effect of a grain boundary on the collected current. The advantage of using A instead of i(x) is that the profile area is less sensitive to beam characteristics, such as beam size. As shown in ref.8, i(x) is

dependent upon the spot size, because the expression for i(x) involves lateral distribution of the generation. A is dependent only on the depth distribution of the generation, and is thus independent of the beam size. It should be pointed out that this advantage is somewhat offset by the complexity of the numerical integrations of the contrast profile.

The variance of the profile, σ^2, is a measure of profile spread, and is expressed as

$$\sigma^2 = \frac{1}{A}\int_{-\infty}^{\infty} x^2 i(x)\, dx \qquad 5.8$$

Thus both A and σ can be determined by numerical integrations of the contrast profile. It will seen that A is sensitive to the grain boundary surface recombination velocity, and σ is sensitive to the diffusion length L.

It would be desirable to use a single diagram capable of yielding directly v_s and L by entering values of A and σ. Such a diagram has been constructed on the basis of a plot of A/R and σ/R [8], and is shown in Fig.5.3. This plot relates the area and standard deviation of an induced current contrast profile for a grain boundary to the surface recombination velocity and the diffusion length.

In summary, the following steps are needed to determine v_s and L by EBIC :

1. Locate a grain boundary by using SEM-EBIC

2. Record the current signal as a function of distance from the boundary by applying

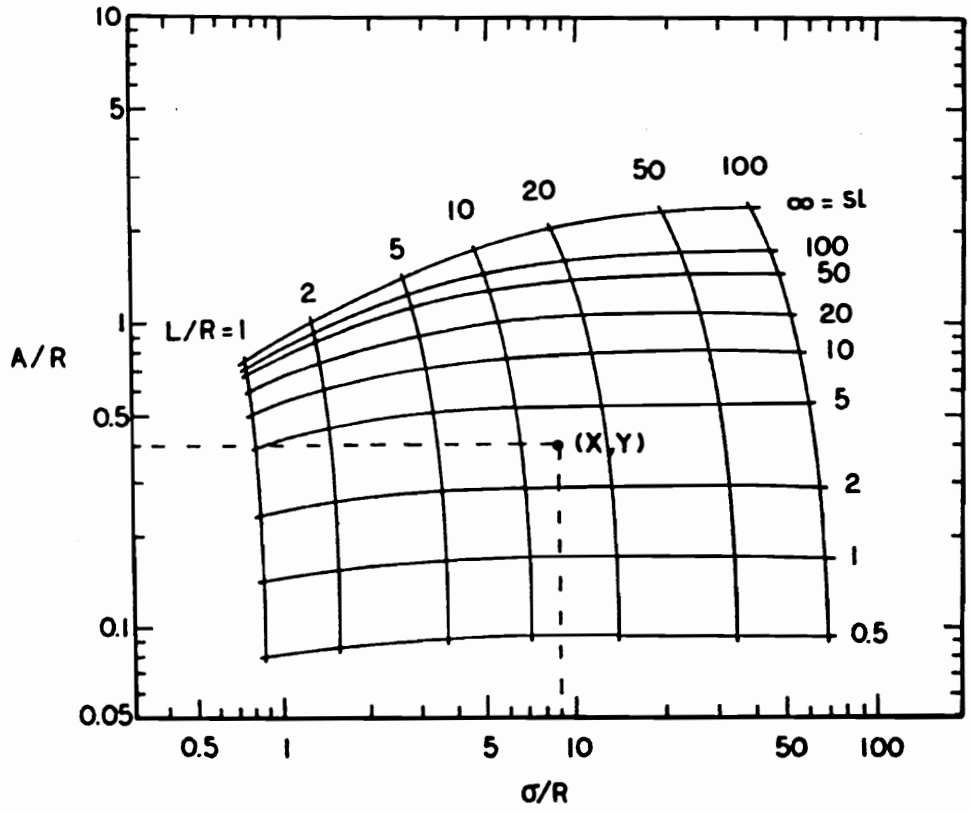

Fig.5.3 Diagram relating the A and σ of the EBIC contrast profile of a grain boundary to the interface recombination velocity and diffusion length, R is the electron range. after ref.[8].

an EBIC line scan across the boundary

3. Convert the current signal into a current contrast profile
4. Numerically integrate the profile to find A and σ
5. Find the values of L/R and SL, and hence v_s and L, by using the diagram of A/R vs. σ/R (Fig.5.3)

5.4 EBIC Measurements

a. The EBIC set-up

The SEM machines used for this study are Armary 120 and Jeol-35C types. The latter type was modified for EBIC measurements, and equipped with a lock-in amplifier to give better EBIC sensibility and image resolution. A schematic of the principal EBIC set-up is shown in Fig.5.4. A p-n junction solar cell serves as both the detector and the tested sample. The electron beam perpendicular to the surface of the sample generates electron-hole pairs inside the semiconductor. The excess carriers are collected by the p-n junction and amplified by a Kethley 427 or lock-in amplifier. The resulting video signals are used to modulate the brightness of the display cathode ray tube (CRT) and to produce EBIC maps on the SEM screen. For quantitative study of the grain boundary recombination velocity and diffusion length, an EBIC line scan is needed to get the experimental data for the contrast profile across the boundary. An analog-to-digital converter (ADC) is connected directly to the analog output of the current amplifier and the drivers for the vertical and

horizontal axes of the CRT of the SEM. A microconputer is used to digitize the EBIC signal and electron beam coordinates. A schematic of the hardware used for data acquisition of an EBIC line scan is shown in Fig.5.5. The flow chart of the routine used for the evaluation of an EBIC current contrast profile is presented in Fig.5.6.

b. The EBIC micrograph of grain boundaries

As shown in Fig.5.7(a), the grain boundaries are not very clear in the SEM picture but can be examined in the EBIC mode as shown in Fig.5.7(b). In general, the EBIC micrographs differ in darkness from one boundary to another as shown in Fig.5.8. Some of them are electrically active in recombination and are darker, and others are not that active, and are lighter. The darkness of a grain boundary in an EBIC picture is related to the recombination center density at the boundary. The darker boundary also results in larger current contrast, corresponding to higher grain boundary recombination velocity. In practical measurements, the current line scan profile is not symmetric with respect the boundary. Therefore, each half of a profile, on the left and right sides, is treated separately. This asymmetry may result from a nonuniform distribution of dislocation density causing different diffusion lengths in the adjacent grains. It may also result from a boundary which is not exactly perpendicular to the surface of the sample.

In order to evaluate A and σ, an average base line is needed in a line scan measurement. σ is very sensitive to the choice of the background and profile tails

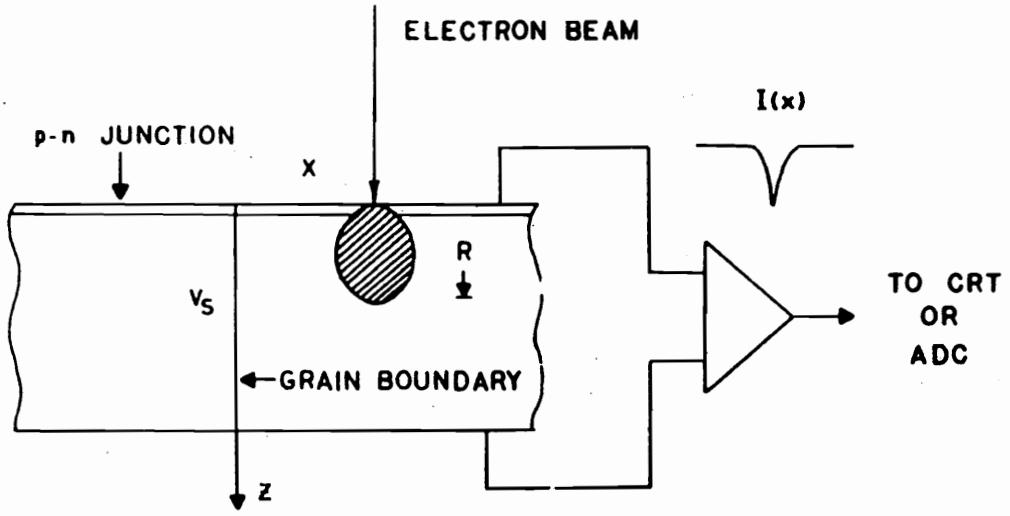

Fig.5.4 Schematic of EBIC method used to measure grain boundary recombination [8]

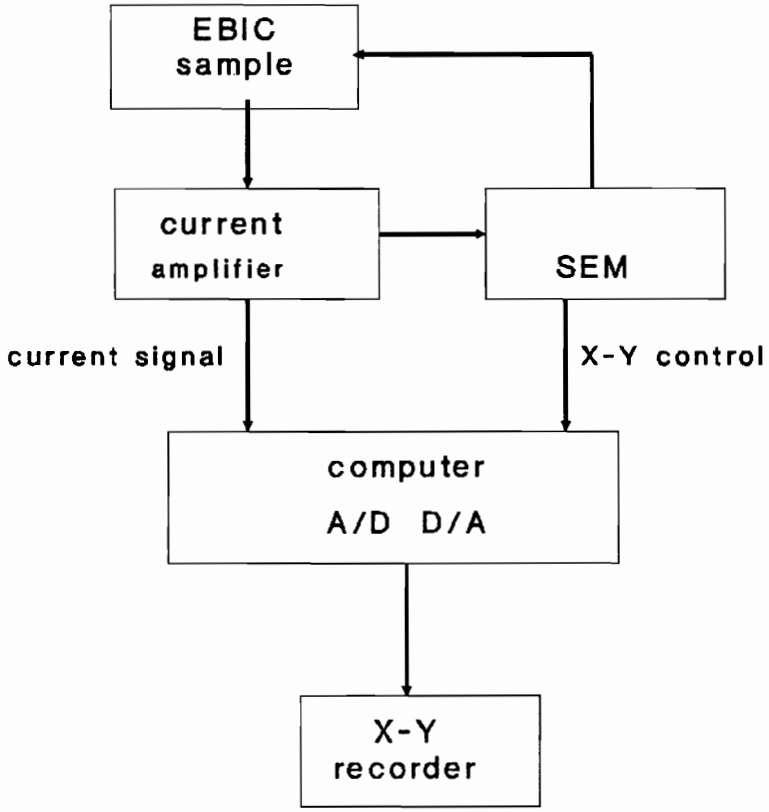

Fig.5.5 Hardware used for EBIC line scan data acquisition

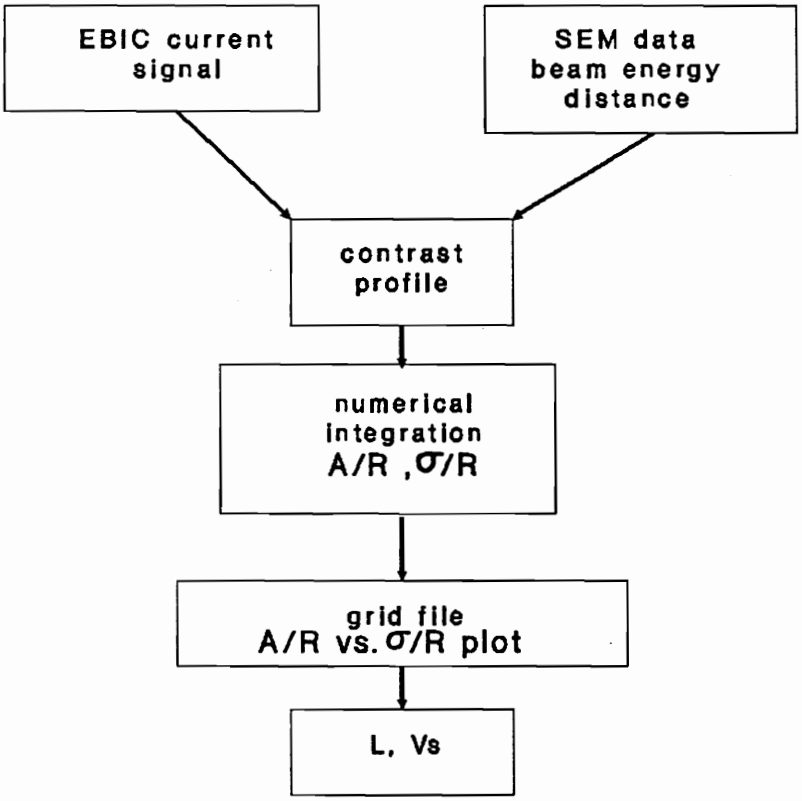

Fig.5.6 Flow chart for the evaluation of Vs and L

(a)

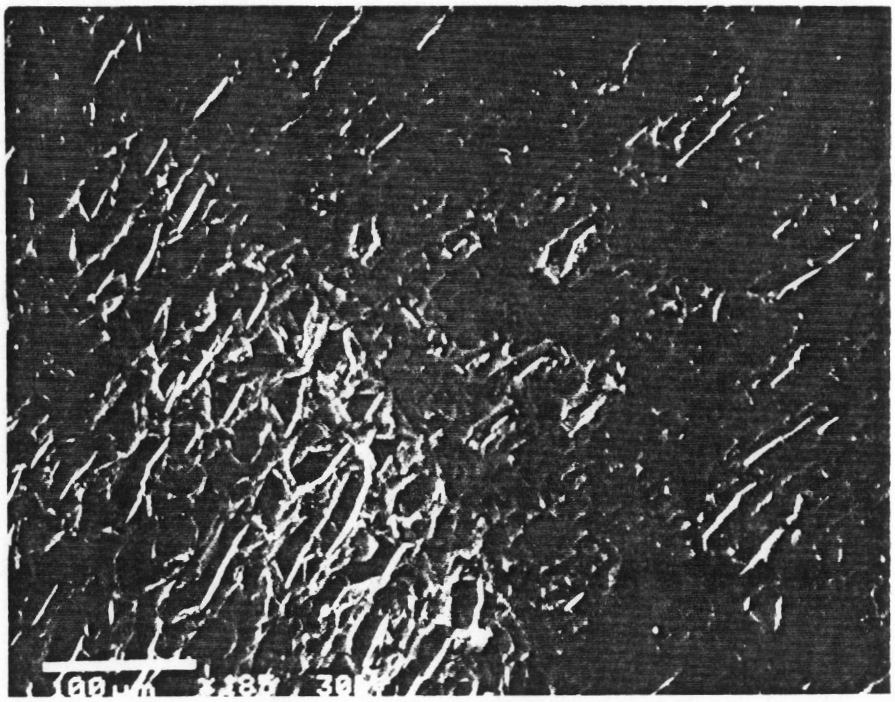

(b)

Fig.5.7 (a) A poly-Si grain boundary in the SEM picture and (b) the boundary as seen in EBIC

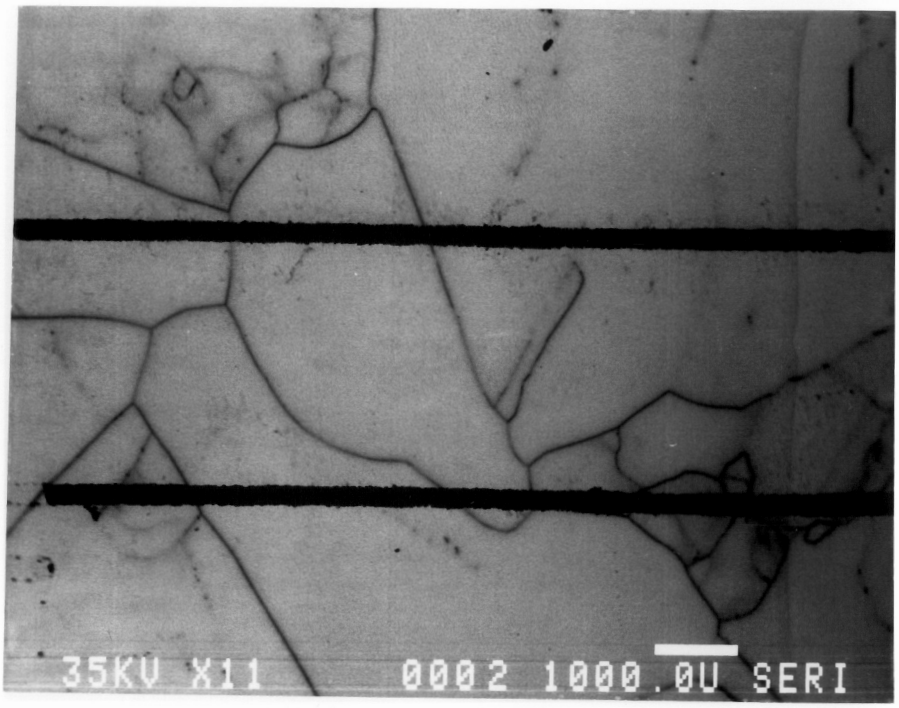

Fig.5.8 An EBIC map of nonuniformity in recombination from one boundary to another in a same sample

beause of the factor of x^2 in its definition. So a clean background signal is essential to get a reliable value of σ. A lock-in amplifier helps in this matter. Fitting experimental data by a least-square method is another way to get a smooth tail of the profile. It was found that a function in the form of

$$f(x) = \frac{1}{Ce^{Dx}+1} \qquad 5.9$$

was useful to get a smooth tail. The C and D in (5.9) are determined by the experimental data.

Table 2 shows values of v_s and L for five boundaries, which are determined from the left and right side of the boundaries separately.

Table 5.2. Values of v_s (cm/s) and L(μm) for five boundaries, determined from the left and right sides of the boundary

GB side	A (μm)	A/R	σ (μm)	σ/R	L/R	SL	v_s (cm/s)	L (μm)
left	6.163	0.72	15.48	1.8	2.5	18	2.1×10^5	21.5
right	5.735	0.67	11.84	1.4	2.0	15	2.6×10^5	17.22
left	2.74	0.32	8.731	1.02	1.6	3.5	6.3×10^4	13.78
right	4.28	0.5	16.26	1.9	2.7	5.7	6.1×10^4	12.9
left	2.56	0.3	17.12	2.0	2.8	2.78	2.8×10^4	24.11
right	3.94	0.46	9.46	1.1	1.5	5.7	2.9×10^4	23.25
left	5.56	0.64	7.66	0.89	1.2	20	4.8×10^5	10.33
right	5.15	0.60	6.15	0.72	0.8	20	5.4×10^5	7.0
left	1.027	0.12	21.4	2.5	3.1	0.7	6.5×10^3	26.69
right	1.284	0.15	22.25	2.6	3.5	0.8	6.7×10^3	30.14

It is interesting to note that the values of v_s obtained by analyzing the two halves

of the profile are very close to each other for a boundary, while L values can be quite different for both sides of the grains. It is also seen that variations of both v_s and L are quite large for different boundaries. An effort to explain these variations was made in this study by the electron channeling experiments described next.

c. Electron channeling patten (ECP) study

As shown previously, different grain boundaries have different recombination activities. This difference may be correlated with the crystal orientations of grains, and with nonuniform impurity distribution in the boundaries, or with both, since impurities have a larger probability to segregate in a high angle grain boundary. These conjectures were thought to be reasonable, but no direct experimental evident has been reported. However, combining the EBIC and ECP techniques provides a practical means to correlate the grain boundary combination and crystal orientations.

The electron channeling patten plays a role in the SEM similar to that of diffraction and Kikuchi pattens in the transmission electron microscope (TEM), but has the additional advantage that no thinning of the specimen is required. In most modern SEM machines, the EBIC and ECP procedures can be done alternately for the same area of a given sample. The technique of electron channeling of the SEM permits a rapid determination of whether a given specimen is amorphous or crystalline, and if crystalline, the type and orientation. Grain boundary angle can be determined by knowing the orientations of the grains. A detailed theory of electron channeling is presented in ref.[16]. Only basic principle of the ECP method will be

explained here.

The probability for an incident electron to be backscattered depends on how closely it approaches the nucleus of the atom that is deflecting it. If a beam of electrons is incident on an amorphous material, then irrespective of the direction of the beam relative to the surface normal, the packing density of the atoms will look the same, and the backscattering probability will be constant. In case of a crystalline material, however, the apparent packing density of the atoms varies with the angle of incidence. In particular, for certain directions, such as parallel to the crystal lattice planes, the packing density appears to be low because all the atoms are aligned. Therefore the electron has a high probability of penetrating deeply, ie channeling, into the sample before it is scattered, and consequently has a lower probability of being backscattered. The backscattering coefficient for a beam of electrons incident on a crystal surface will show modulations at angles related to the symmetry of the lattice.

Electron channeling pattens for three grains are shown in Fig.5.9(b). These three grains joint each other and form three grain boundaries. The EBIC images of these three boundaries are shown in Fig.5.9(a). From the EBIC micrograph, it can be seen that two boundaries are more active in recombination than the third. The orientations of these three grains were determined from the ECP pattens (Fig.5.9 (b) and (c)) through a calibrating ECP map shown in Fig.5.9(d) for silicon provided by SERI (Solar Energy Research Institute). In the map, the ECP pattens for the

(a)

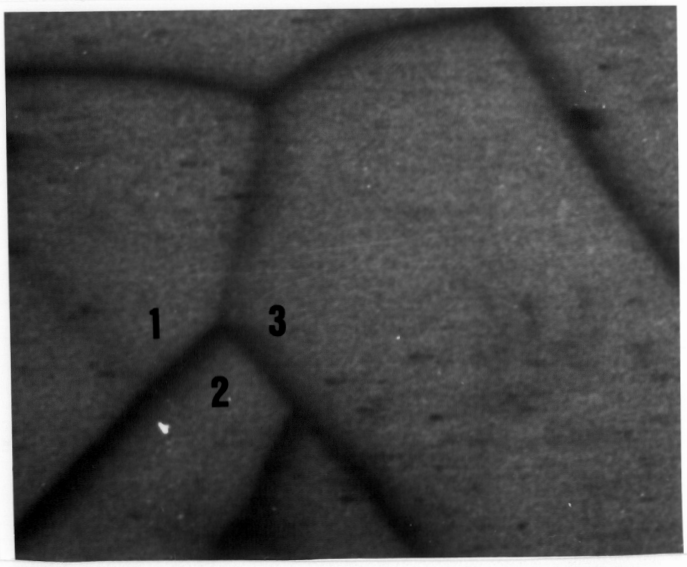

1

(b)

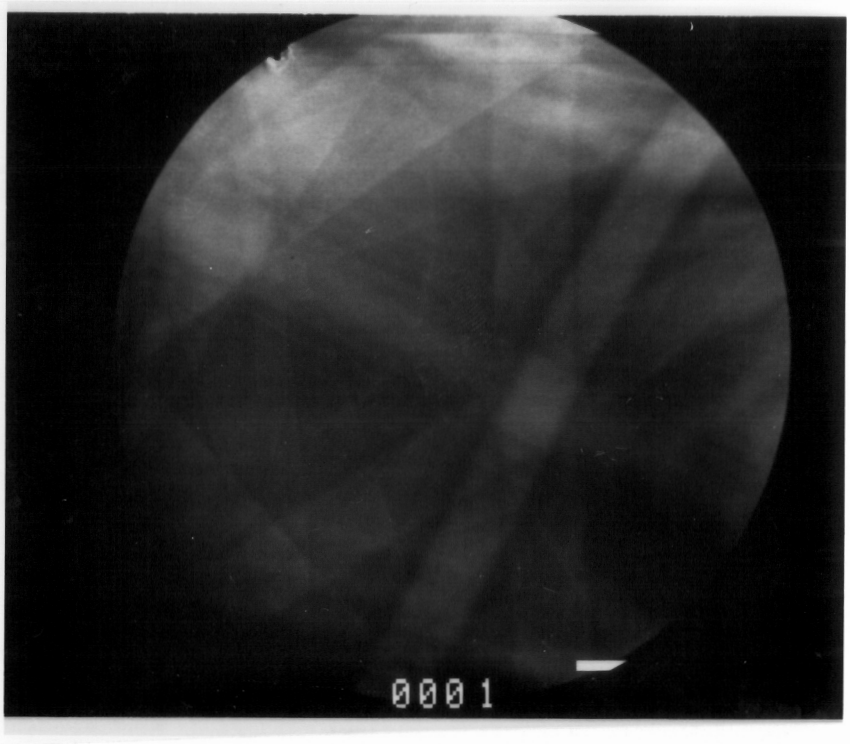

Fig.5.9 (a) EBIC pattern, showing three grain boundaries; (b) Electron channeling pattern (EPC) for grain 1, [112] orientation is indicated

2

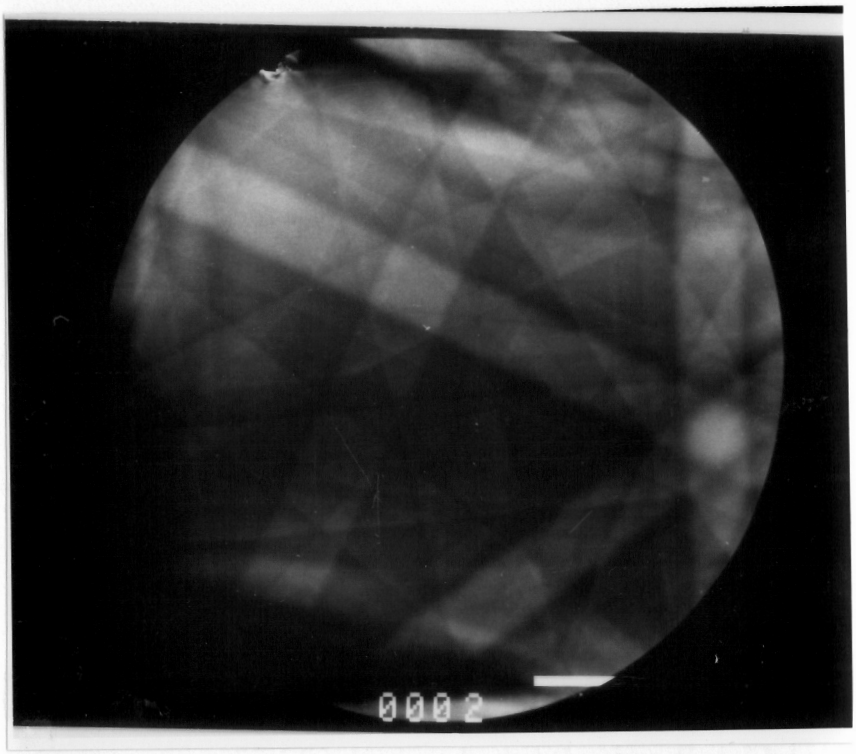

3

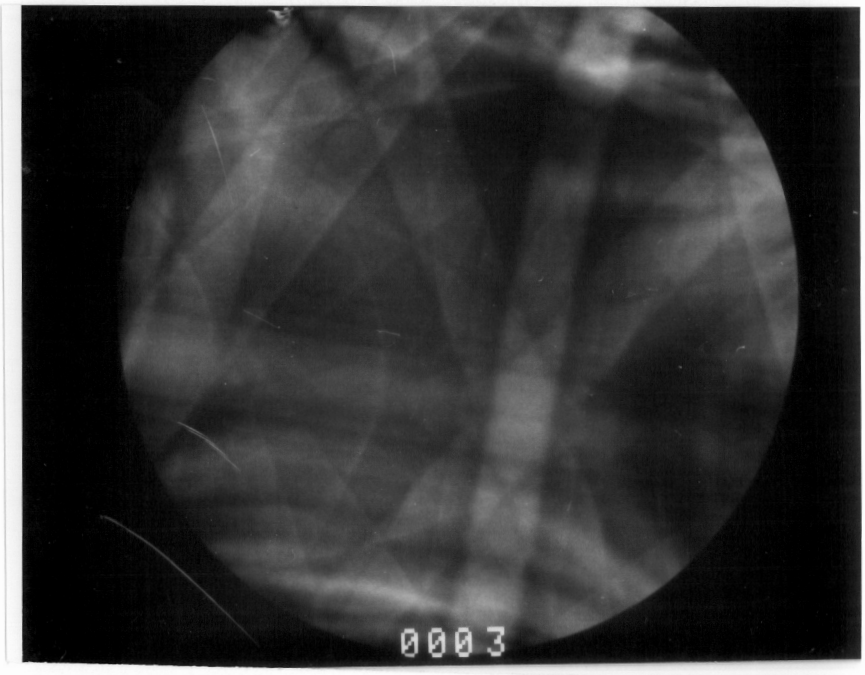

Fig.5.9 (c) ECP for grains 2 and 3, [111] and [112] orientations are indicated, respectively

Fig.5.9 (d) Electron channeling map used to determine the crystal orientation for silicon (provided by SERI).

different crystal orientations are assigned for Si. The numbers at the cross points of major bright lines are the Miller indices. Grains 1, 2 and 3 are in the [112], [111] and [112] crystallographic orientations, respectively. The angle between the [112] and [111] planes is 19.47 degrees. Similar results were also found for other grains. These results indicate that grains 1 and 3 have the same lattice parameters and the boundary is coherent. Grain 2 has different lattice parameters from grains 1 and 3 and the boundaries between them are incoherent. These results provide direct experimental evidence that an incoherent boundary is at least part of reason for the high recombination in the boundary.

Future efforts are needed to determine a quantitative correlation between the crystallographic mismatch and the recombination of the boundaries, and between the mismatch and impurity segregation.

5.5 EBIC study of hydrogen passivated grain boundaries

The improvements in solar cell performance due to the backside hydrogenation have been discussed in the previous chapter. In this section, the hydrogen passivation effect on grain boundary recombination was studied in micro-scale by the EBIC technique.

A major question which has not been answered in backside hydrogenation is how deep hydrogen can go. For solar cells, the crucial region is close to the p-n junction, so the hydrogen should diffuse to this depth. An indirect method to determine

passivation depth uses surface voltage profiles across the grain boundary. This method was developed by Seager and Ginley, and passivation depths of several hundred microns were inferred [26]. Hanoka et.al.[17], using EBIC to detected the passivation depth of frontside hydrogenation, indicated that at least a depth of 9 microns could be passivated. Dube et.al.[27] implanted hydrogen into a cleaved side surface and monitor the passivation depth along grain boundaries on the sample surface. Passivation depths varying from 5 - 200 microns were found. Experimentally, implanting hydrogen from a cleaved side surface is not very convenient. Additionally, grain boundary properties in the vertical direction (perpendicular to the sample surface) is not necessary to be the same as in the horizontal direction. The depth in the vertical direction is a major concern in practice.

In this study, we report for the first time the use of EBIC measurement to directly determine the passivation depth in the direction normal to the sample surface for backside hydrogen implantation. It is shown that EBIC is a simple and practical method to monitor grain boundary passivation for backside hydrogen implantation. Quantitative analysis for grain boundary recombination before and after hydrogen passivation, and the effect of annealing on grain boundary recovery, are also presented.

The samples used in this study were phosphorus-diffused n^+/p junction poly-Si solar cells supplied by Solarax. The junction depth was about 0.5 μm. Grain

boundaries were generally normal to the cell surface.

Hydrogen passivation was done in the Kaufman ion beam system (The details of the system were discussed in the previous chapter). The EBIC measurements were carried out in a modified JEOL-35C SEM machine. An EBIC picture for the whole sample was taken before hydrogen treatment. One specific grain boundary was located to be studied before and after hydrogen passivation. In our experiment one of the darker and easily relocated grain boundaries was chosen.

It was found in non-passivated samples that grain boundary recombination (as seen in EBIC line scan contrast) was nearly constant for different positions of the given boundary. Fig.5.10 (a) shows an EBIC micrograph of the recombination due to a grain boundary without hydrogen passivation. The picture was taken at an electron beam energy of 35 keV and magnification of 75. The wider dark line is a metallization contact. The narrow line is the grain boundary being studied. The upper white line is the EBIC line scan current signal and the lower one is a reference line corresponding to zero current. The maximum current contrast, C, defined as $(I_{max} - I_{min})/I_{max}$, for the boundary before hydrogen passivation is 0.48. The hydrogen implantation was done at an ion beam energy of 1.5keV and beam current of 55mA. The sample holder was maintained at a temperature of 250 °C. Fig.5.10(b) shows an EBIC picture for the boundary after fifteen minutes of hydrogen implantation. The picture was taken at the same location as Fig.5.10(a). It shows that after the hydrogen treatment the grain boundary becomes lighter and much more narrow than

(a)

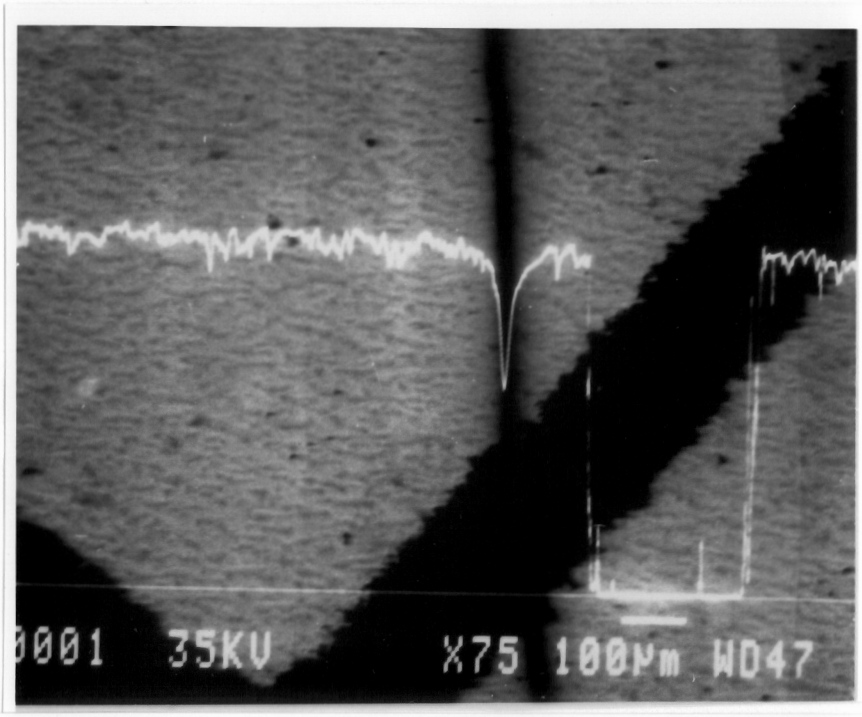

(b)

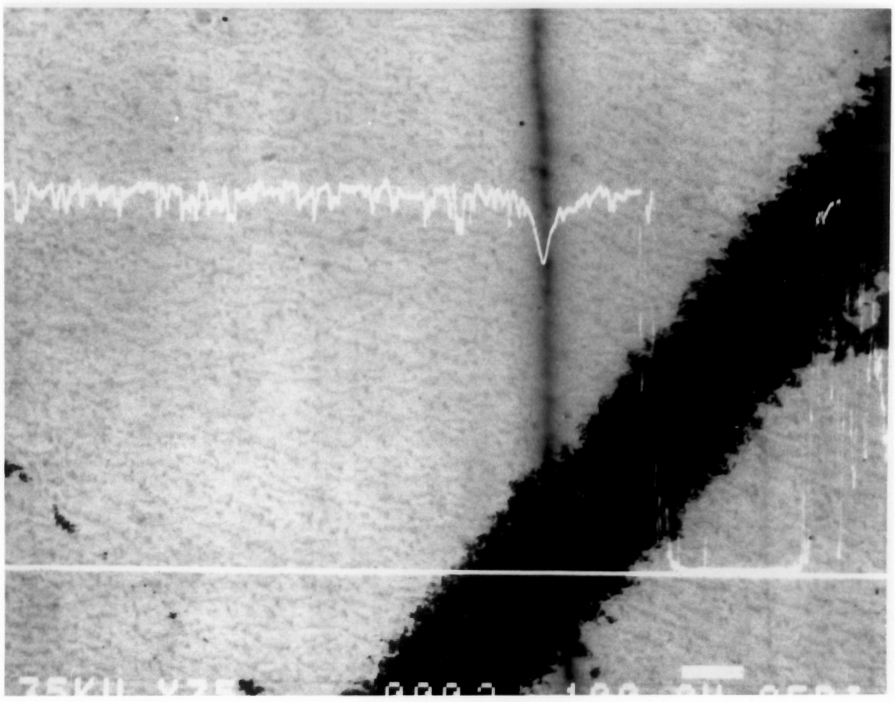

Fig.5.10 Superimposed EBIC image of a grain boundary and a current line scan before hydrogen passivation (a) and after passivation (b), for the same grain boundary (magnification of 75).

before the treatment, and that the contrast decreased to less than 0.2. It is also interesting to note that the EBIC image of the grain boundary shows a discontinuity of darkness following hydrogenation. The uniform boundary before the passivation becomes nonuniform and much lighter in appearance after the passivation. This indicates that the passivation depth is not uniform, even for the same boundary. This nonuniformity can be better seen at a larger magnification in Fig.5.11. A nonuniformity in the current contrast as high as 50% was measured. The maximum contrast in the range of 0.1 - 0.2 was determined at different positions for the boundary. Reasons for this nonuniformity are still not clear. They may relate to passsivation mechanisms and defect distribution in grain boundaries. Hydrogen may have better passivation effect on some of defects than on the others and distribution of defects may not be uniform in grain boundaries. Further investigation is needed.

The hydrogen diffusion depth (or passivation depth) can be determined by the EBIC measurements by knowing the thickness of the solar cell and the electron penetration depth. The thickness of the cell used in the experiment was about 250 μm. The electron beam energies used in the EBIC measurements are 35 keV. The corresponding penetration depth is less than 10 μm [13]. Since the hydrogen were implanted from the backside of the cell and the electron beam in EBIC probes the frontside of the cell, the EBIC can detect the passivation only when the hydrogen is deep enough. From Fig.5.10(a) and (b), the pasiivation effect is very clear in both the EBIC micrograph and the current contrast. Even if the nonuniformity of the

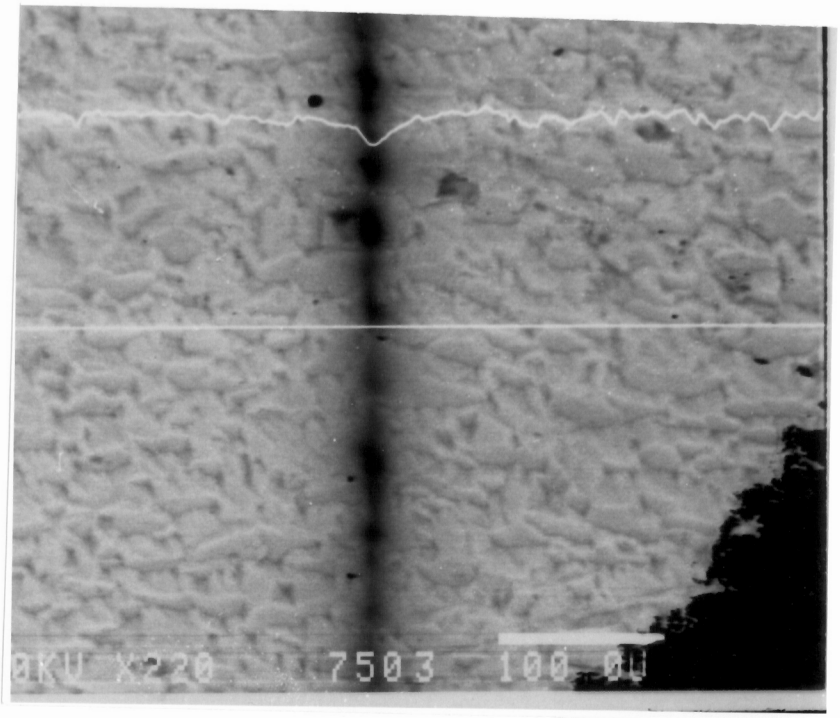

Fig.5.11 The grain boundary shown in Fig.5.10 under increased magnification of 220, showing non-uniformity along the grain boundary

boundary is taken into account, a dramatic decrease in the contrast from 0.48 to 0.18 is still seen. This confirms that the boundary has been partly passivated in a depth of 230 μm from the backside surface.

Besides grain boundary passivation, passivation of point defects and dislocation defects inside of the grains is also observed. This is seen in the clearer EBIC picture for the passivated sample. Fewer dark points appear in Fig.5.10(b) than in Fig.5.10(a). This can explain why the diffusion length is improved after passivation (as shown in Table 4.3) by means of a reduction in minority carrier recombination. Fig.5.12 shows the changes in the current contrast profiles before and after the passivation (these profiles are from one half of the current line scan measurements). In order to see the nonuniformity in the boundary recombination after the passivation, two line scans were shown in the Fig.5.12, which had maximum line scan, (LS), contrast of 0.2 and 0.1, respectively. They are noted as LS(.2) and LS(.1). Table 5.3 shows quantitative improvements in v_s and L due to the passivation.

Table 5.3. The values of grain boundary recombination velocity v_s(cm/s) and the diffusion length L(μm) before and after the passivation

	before left side	before right side	after left side LS(.2)	after right side LS(.2)	after left side LS(.1)	after right side LS(.1)
v_s(cm/s)	4.8×10^5	5.4×10^5	8.1×10^4	1.0×10^5	2.1×10^4	2.5×10^4
L(μm)	10.33	6.89	13.78	12.05	14.1	12.2

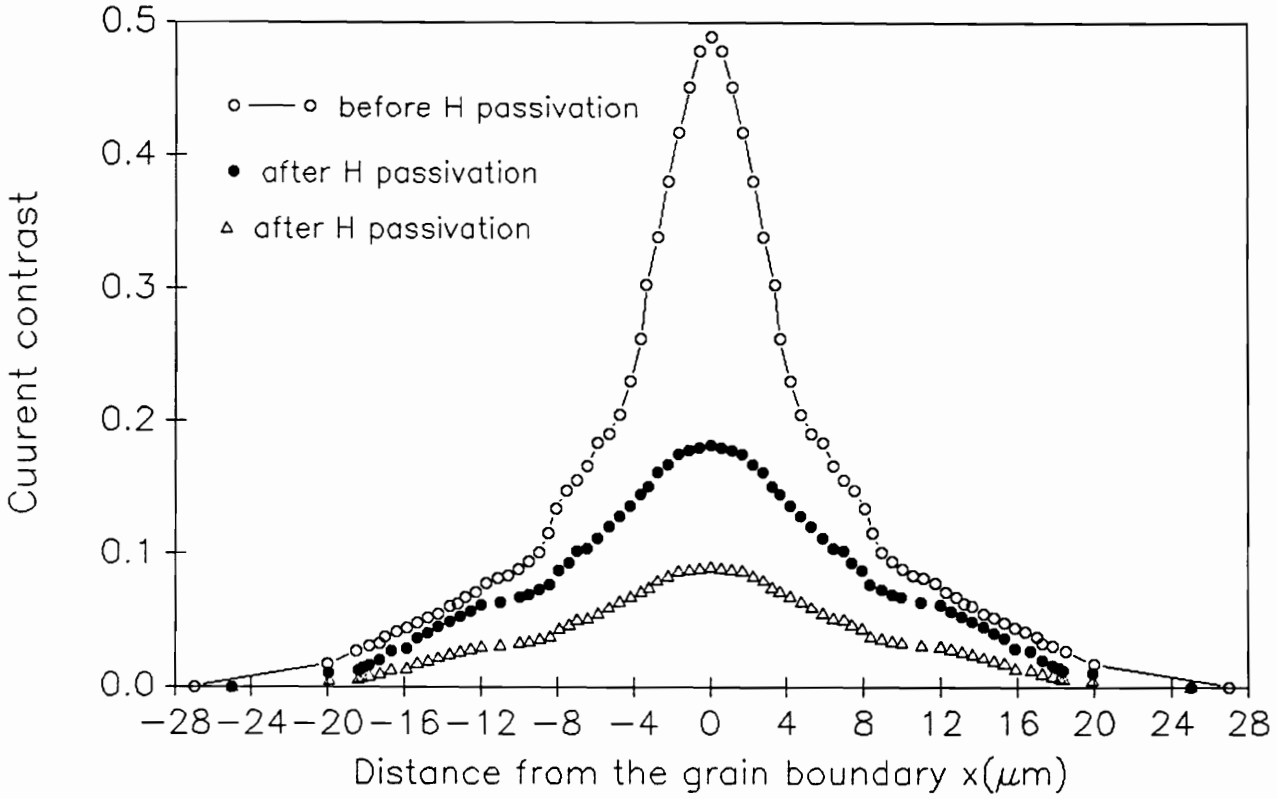

Fig.5.12 Current contrast profile before and after the passivation. • and △ were measured at different positions for the same boundary and corresponding to LS(.2) and LS(.1), respectively

If a simple average is taken, we have the following:

before the passivation: $v_s = 5.1x10^5$ (cm/s), L = 8.61 (μm)

after the passivation: $v_s = 5.6x10^4$ (cm/s), L = 13.03(μm)

It can seen that the hydrogen passivation reduces the boundary recombination velocity about one order of magnitude and increases the diffusion length about 40 % for this boundary.

Fig.5.13 shows an example of using EBIC line scan to monitor the effect of hydrogen implantation on grain boundary recombination. The maximum contrast C can be used to quickly check the degree of passivation, if only a qualitative result is required.

An annealing experiment was done in the vacuum chamber of the SEM machine. A temperature controlled stage was used and the sample was maintained at 340 °C for five hours, then cooled down to room temperature . Fig.5.14 shows the EBIC image and the line scan current signal after the annealing for the same boundary and about same position as in Fig.5.10. Since the same boundary had been measured many times, part of the metal contact was lifted off (see Fig.5.14). But no decrease in collected current was observed in Fig.5.14. This is because the region under the contact had been alloyed. So it was still a good conductor region even after the top metal was lifted off. Therefore it would not influence the EBIC results significantly.

It can be seen that the boundary tends to revert to its original, non-passivated, condition. This indicates that the hydrogen which passivated the defects in the grain

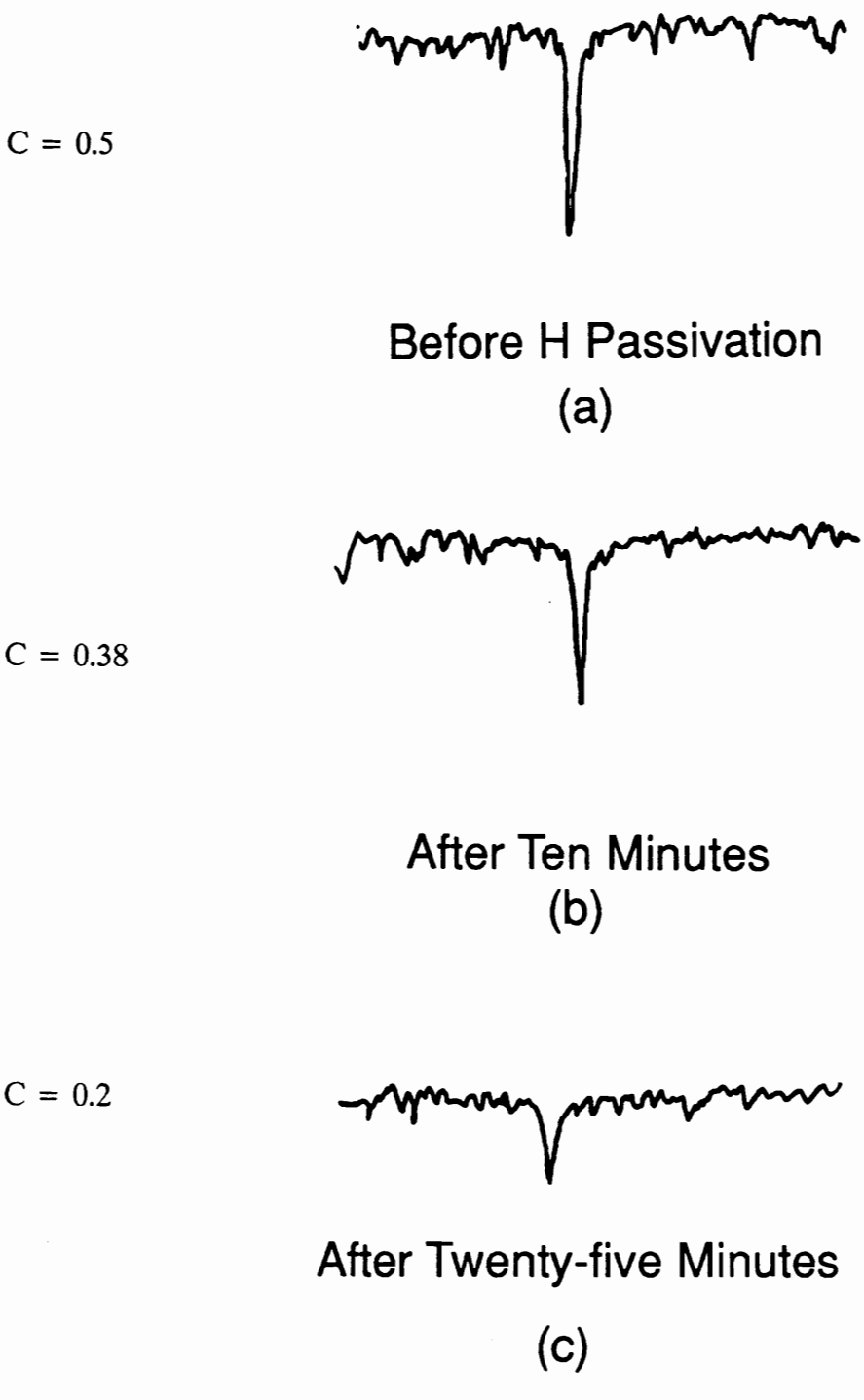

Fig.5.13 Using EBIC line scan to monitor the grain boundary passivation for different implantation times. C is the maximum contrast.

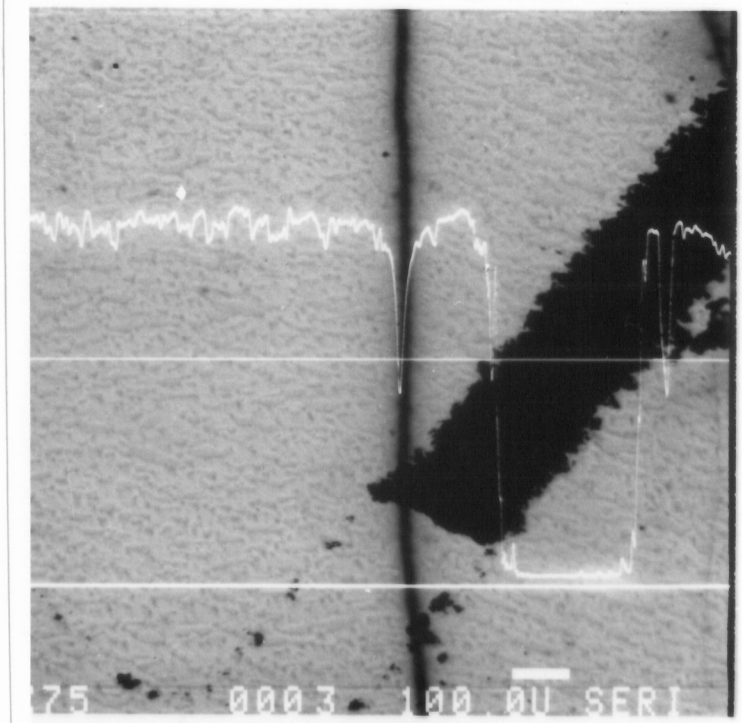

Fig.5.14 EBIC image of the same boundary as shown in Fig.10 after annealing at 340°C for 5 hours

boundary can diffuse out of the boundary at the annealing temperature of 340 $_{o}$C. The results of annealing experiment can be used to determine the uplimit temperature in hydrogen implantation. An interesting question about hydrogen passivation mechanism in the silicon grain boundary is raised here. Hydrogen saturating Si dangling bond in grain boundary to form Si-H bond was thought to be the passivation mechanism. However, the dissociation energy of the Si-H bond is in the range of 1.5 - 3 eV [13], the thermal energy provided in our annealing experiment is about 0.05 eV which is much smaller than the chemical bond dissociation energy. Therefore the simple saturation dangling bond model along cannot explain the annealing result. Some impurities such as oxygen segregated in the boundaries, acting as electric recombination centers, has been suggested, and the interaction of hydrogen with the impurities may play an important role in the passivation [14,15]. More investigations on the passivation mechanism are still needed.

In summary, a hydrogen diffusion depth of more than 230 microns, as measured from the back surface, was detected directly by EBIC on the front side of the cell. Quantitative analysis showed that the recombination velocity can be improved by one order of magnitude. Nonuniformity of passivation was also observed. However, the details of the passivation mechanism and the configuration of hydrogen in Si grain boundary are not yet well understood.

5.6 EBIC study of surface recombination velocity for different surface conditions

As shown in Chapter 2, surface recombination velocity is one of the critical parameters controlling solar cell efficiency. It strongly depends on the cell fabrication process. Besides grain boundary recombination velocity, cell surface recombination velocity can also be characterized by the EBIC technique. Four different surface conditions were studied in our experiments. The details of the mathematic derivations about this method have been done by Von Roos [28,29]. The principle of the method is the follows.

For a p-n junction normal to an electron beam, if the junction depth Z_j (distance from tested surface to the junction) is much larger than the electron penetration depth R, the EBIC current can be expressed as [29]:

$$I = qG\left[\frac{\cosh\left(\frac{R}{L}\right)+S\sinh\left(\frac{R}{L}\right)}{\sinh\left(\frac{Z_j}{L}\right)+S\cosh\left(\frac{Z_j}{L}\right)}\right] \qquad 5.10$$

where

G= beam generation rate

R= electron penetration depth

L= minority carrier diffusion length

S= sL/D, normalized surface recombination velocity

D= Electron diffusion constant, the value of 25 cm^2/s was chosen.

Under constant generation rate condition, Eq.5.10 becomes

$$\frac{\partial \ln(I)}{\partial R} = -\frac{1}{L}\frac{\sinh(\frac{R}{L}) + S\cosh(\frac{R}{L})}{\cosh(\frac{R}{L}) + S\sinh(\frac{R}{L})} \qquad 5.11$$

The surface recombination velocity s can be solved from Eq.5.11

$$s = D\frac{\partial \ln(I)}{\partial R}\left[\frac{S(\cosh(\frac{R}{L}) + S\sinh(\frac{R}{L}))}{\sinh(\frac{R}{L}) + S\cosh(\frac{R}{L})}\right] \qquad 5.12$$

For crystalline Si cells, L >> R is generally valid at the beam energy less than 25 keV, so Eq.5.12 is simplified as [28]

$$s \approx D\frac{\partial}{\partial R}\ln(I) \qquad 5.13$$

Therefore s can be estimated by using Eq.5.13 and measuring the energy dependence of EBIC current.

In order to meet $Z_j >> R$, backside surface recombination velocity S_n of n^+/p solar cells were characterized. A schematic of sample configuration is shown in Fig.5.15. The recombination velocity for crystalline Si cells under four type surface conditions were determined. These surface conditions are:

a. Hydrogen implanted surface at ion beam energy of 1.5 keV, and beam current of 55 mA for 5 min.

b. Fresh chemically etched surface by CP-4A solution for 20 sec. and then rinsed in deionized water.

c. Exposure to air for overnight after the etching

d. Oxidized surface at 200 °C in dry O_2 for three hours.

In the measurements, the constant generation condition was satisfied by keeping the product of E_b and I_b constant, (see Eq.5.3). It can be easily realized for $E_b \geq 10$ keV. The energy dependence of R is determined by Eq.5.2. The electron beam energy varied from 10 to 20 keV by an increment of 2 KeV. The beam current I_b was measured by a Faraday cup and the EBIC current was measured by a Kethley 427 current amplifier. The experimental parameters E_b, I_b and measured EBIC current I as a function of R for four surface conditions are listed in Table 5.4. The measured EBIC currents I_1, I_2, I_3 and I_4 in the table correspond to the surfaces a, b, c and d respectively. The EBIC data for each sample was interpolated by the cubic spline method. The derivative of ln(I) with R was determined numerically in terms of the interpolation at an average electron penetration depth, <R>. A value of 2.01 μm was found for <R> from the Table 5.4. The results of derivatives and surface recombination velocities S_n are summarized in Table 5.5.

It shows that the surface recombination velocity is increased by hydrogen implantation while decreased by a thin SiO_2 layer. Freshly etched surface and the surface exposured to air also show different recombination velocities.

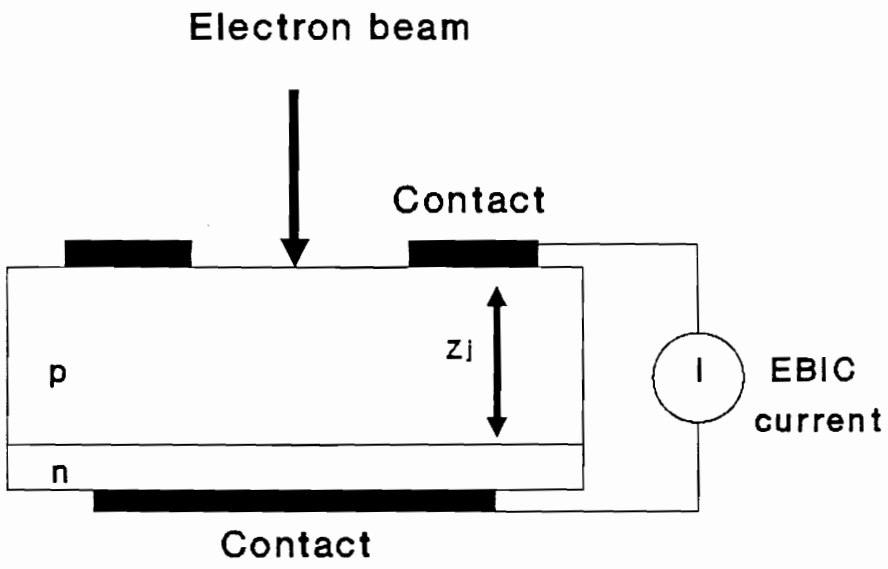

Fig.5.15 Configuration for the measurement of surface recombination velocity

Table 5.4. The measured EBIC current I as a function of R

E_b(keV)	10	12	14	16	18	20
I_b(nA)	0.5	0.42	0.36	0.31	0.28	0.25
R(μm)	0.96	1.32	1.73	2.18	2.69	3.23
$I_1(10^{-7}A)$ $\ln(I_1)$	1.68 o.52	3.0 1.1	5.47 1.7	36.59 3.6	54.59 4.0	66.68 4.2
$I_2(10^{-7}A)$ $\ln(I_2)$	22.19 3.1	22.42 3.11	23.1 3.14	24.05 3.18	25.28 3.23	25.79 3.25
$I_3(10^{-7}A)$ $\ln(I_3)$	8.17 2.1	8.49 2.14	9.5 2.26	11.25 2.42	12.18 2.5	13.33 2.59
$I_4(10^{-7}A)$ $\ln(I_4)$	66.69 4.20	66.95 4.204	67.36 4.21	68.10 4.22	68.92 4.23	69.41 4.24

Table 5.5 Surface recombination velocity S_n for four surface conditions

Surface condition	∂ (ln I) / ∂ R	S_n(cm/s)
a. H^+ implanted	**$4.47x10^4$**	**$1.12x10^6$**
b. Fresh etched	**$0.085x10^4$**	**$2.13x10^4$**
c. Exposure air	**$0.346x10^4$**	**$8.65x10^4$**
d. Thin oxidized	**$0.025x10^4$**	**$6.1x10^3$**

References

1. E.J.Sternglass, Phys.Rev., 95, p348, (1954).

2. A.E.Grun, Z. Natureforsch., 12a, p89 ,(1957).

3. G.Oelgart and H.Scholz, Phys.Stat.Sol.(a), 75, p547, (1983).

4. D.B.Holt and D.C.Joy, "SEM Microcharacterization of Semiconductors", Academic press, p245, (1989).

5. J.R.Fiebiger and R.S.Muller, J.Appl.Phys., 43, p3203,(1972).

6. T.E.Everhart and P.H.Hoff, J.Appl.Phys., 42, p5837, (1971).

7. G.E.Possin and J.F.Norton, "Scanning Electron Microscopy", IIT Reseach Institute, Chicago,Ill., p457, (1975).

8. C.Donolato, J.Appl.Phys., 54, p1314,(1983).

9. J.Marek, J.Appl.Phys., 55, p318, (1984).

10. J.D.Zook, J.Appl.Phys., 37, p223,(1980).

11. R.O.Bell, Short course in 21st IEEE Photovotaic Spec.Conf. (1990)

12. D.B.Holt and D.C.Joy, "SEM Microcharacterization of Semiconductors", Acadamic Press, p306, (1989).

13. C.Donolato, in"Polycrystalline Semiconductors", Edited by G.Hartbeke,(1985), Spring Series in Solid-State Sciences 57, p143.

14. J.Oualid, et.al., J.Appl.Phys., 17, p119, (9180).

15. J.Marek, J.Appl.Phys., 53, p1454, (1982).

16. D.B.Holt and D.C.Joy, " SEM Microcharacterization of Semiconductors", Academic Press, p69, (1989).

17. J.I.Hanoha, C.H.Seager, D.J.Sharp and J.K.G.Panitz, Appl.Phys.Lett., 42, p618, (1983).

18. Y.Simon Tsuo and Milsten,J.B., Appl.Phys.Lett., 45, p971, (1984).

19. J.C.Muller, V.T.Quat and P.Siffert, Solar Cells, April, p109, (1988).

20. R.O.Bell and C.E.Dube, 18th IEEE. Photovoltaic Spec.Conf., p795, (1987).

21. J.Chevallier and M.Aucouturier, Ann.Rev.Mater.Sci., p219, (1988).

22. J.C.Muller, et.al., Solar Cells, 17, p201, (1986).

23. B.L.Sopori, J.Appl.Phys., 64, p5264, (1988).

24. H.Yagi, et.al., 19th IEEE Photovoltaic Spec.Conf., p1600, (1988).

25. S.Martinuzzi, et.al., 18th IEEE Photovoltaic Spec.Conf., p1069, (1987).

26. C.H.Seager and D.S.Ginley, J.Appl.Phys., 52, p1050,(1981).

27. C.Dube,J.I.Hanoka and D.B.Sandstrom, Appl.Phys.lett., 44, p425, (1984).

28. Von Roos, Appl.Phys.lett., 35, p408, (1979)

29. Von Roos, Solid.Sta.Electron., 22, p113, (1979).

Chapter 6

Conclusions and Recommendations for Future Work

6.1 Conclusions

In this research, the following results were obtained:

a. Simpler analytical expressions for the photo-generation rate and photo-current were derived. Based on these two expressions, an analytical approach to the modeling of solar cells was developed. The calculated results agree closely with experimental results, and results reported in the literature.

b. New expressions for the grain boundary barrier height in both dark and illuminated conditions were derived. By using these expressions, the dependences of the minority carrier transport parameters on illumination, grain size, depth, and grain boundary trap state density were determined.

c. 18 percent improvement in cell efficiency was obtained by back-side hydrogen implantation for poly-Si cells with initial efficiencies of about 7%. The improvement strongly depends on the cell's initial conditions and the nature of grain boundary defects.

d. TEM cross-section results of hydrogen-implanted ribbon samples provided direct experimental evidence for a hydrogen-dislocation interaction. Electron diffraction patterns showed that the total dose, not the beam energy, was the

major factor responsible for the surface damage in low energy hydrogen implantation.

e. A hydrogen passivation depth of more than 230 μm was determined directly by EBIC measurements.

f. Hydrogen-saturating Si dangling bonds in the grain boundary is not the only passivation mechanism occuring in hydrogen passivation.

6.2 Recommendations for Future Work

The following topics, as offshoots of this work, should be pursued:

a. An analytical solution should be developed for two dimensional transport equations, in which grain boundaries are treated as boundary conditions.

b. Perform a TEM cross-section study on the hydrogen-dislocation interaction. If a temperature controlled sample stage is used, the movement of the bubbles can be observed, and the hydrogen diffusion constant in silicon could then be determined directly.

c. Combine EBIC and ECP to make a quantitative correlation between a grain's crystal orientations and the grain boundary recombination velocities.

d. The mechanisms involved in hydrogen passivation should be better understood.

Vita

Zhizhang Chen was born in China in 1954. He received a B.S. degree in Physics from Nankai University, Tianjin, China in 1982, and received a M.S. degree in Semiconductor Electronics from the same university in 1985. He came to U.S. in 1985 and received a M.S. degree in Physics from Oregon State University in 1987. He decided to attend the College of Engineering at Virginia Tech in 1988 and received his Ph.D. degree in the Materials Engineering Science in 1991. His primary research interest is in the field of electronic materials and devices.

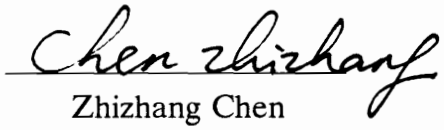

Zhizhang Chen